DEVELOPMENT OF NOVEL ELECTRODES AND ELECTROLYTES FOR SAFER AQUEOUS AMMONIUM-ION BATTERIES WITH ENHANCED PERFORMANCE

A Dissertation

Submitted to the Graduate Faculty of the
Louisiana State University and
Agricultural and Mechanical College
In partial fulfillment of the
requirements for the degree of
Doctor of Philosophy

in

The Department of Engineering Science

by
Shelton Farai Kuchena
B. Eng National University of Science and Technology, 2016
May 2023

Acknowledgements

I would like to offer my sincere appreciation to my advisor Prof. Ying Wang for her guidance support and advice during my PhD work without her supervision and instruction I wouldn't have completed the program.

I also would like to offer my sincere gratitude to Prof. Manas Gartia, Prof. Dorrel Moldovan and Prof. Pallavi Dani for willing to serve in my doctoral committee. I would like to also acknowledge the financial support from LSU Economic Development Award and LASPAC.

Finally, I would like to thank my wife, my family, and friends at LSU for their continued support and encouragement when times got tough during my studies.

Table of Contents

Acknowledgements ii

List of Figures v

Abbreviations vii

Abstract viii

Chapter 1. Introduction 1
1.1. Background 1
1.2. Motivation and NH_4^+ Ion as a Charge Carrier in Batteries 3
1.3. Cathode Materials for Ammonium Ion Storage 5
1.4. Full Cells 7
1.5. Motivation and Scope 8

Chapter 2. Superior Polyaniline Cathode Material with Enhanced Capacity for Ammonium Ion Storage 11
2.1. Introduction 11
2.2. Experimental Section 12
2.3. Results and Discussion 14
2.4. Conclusion 23

Chapter 3. A Full Flexible Ammonium Ion Battery Based on the Concentrated Hydrogel Electrolyte for Enhanced Performance 24
3.1. Introduction 24
3.2. Experimental Section 26
3.3. Results and Discussion. 27
3.4. Conclusion 38

Chapter 4. V_2O_5 Intercalated with Polyaniline for Improved Kinetics in Aqueous Ammonium-ion Batteries. 39
4.1. Introduction 39
4.2. Experimental Section 40
4.3. Results and Discussion. 42
4.4. Conclusion 55

Chapter 5. A Metal-free All-Organic Ammonium-ion Battery with Low-Temperature Applications 56
5.1. Introduction 56
5.2. Experimental Section 57
5.3. Results and Discussion 59
5.4. Conclusion 73

Chapter 6. Conclusions 74

Appendix. Copyright Information. 77

References 93

Vita 103

List of Figures

1.1. Ragone plot of energy and power density for energy storage devices. 1

1.2. Ionic weight, cation radius, and hydrated radius of NH_4^+ ion and metallic charge carriers 3

1.3. Solvation behavior of monovalent ions Li^+, Na^+, K^+ and NH_4^+ ion 4

1.4. Energy configurations for $V_2O_5 \cdot 0.5H_2O$ with intercalating NH_4^+ 7

1.5. Ragone plot showing energy and power density for ammonium ion batteries 8

2.1. SEM images of ES-PANI-coated CFs. 14

2.2. Raman, XRD and XPS spectra of bare CFs and ES-PANI/CFs. 15

2.3. CV curves for ES-PANI/CFs in 0.5M $(NH_4)_2SO_4$ and H_2SO_4 solution of pH 5.3. 16

2.4. CV measurements of ES-PANI/CFs electrodes at various scan rates 17

2.5. Electrochemical perfomance of ES-PANI/CFs i.e. cycling and rate perfomances..... 18

2.6. Electrochemical performance of EB-PANI/CFs i.e. CV curves and rate capability 19

2.7. ES-PANI XPS spectra of N 1s and S 2p at pristine, charged and discharged state..... 20

2.8. Raman spectra of ES-PANI electrodes at pristine, charged and discharged states. 21

2.9. Cycling performances of the ES-PANI/CFs after water and ethanol posttreatment 22

3.1. SEM image, XRD spectra and thermogravimetric analysis result of $NH_4V_3O_8 \cdot nH_2O$ 27

3.2. SEM image, Raman spectra, and XPS N 1s for PANI 28

3.3. Electrochemical performances full cell PANI//$NH_4V_3O_8.2.9H_2O$ 29

3.4. Electronic Impedance spectrum of full cell PANI//$NH_4V_3O_8.2.9H_2O$. 30

3.5. Electrochemical performances quasi solid state PANI//$NH_4V_3O_8.2.9H_2O$ cell 31

3.6. Electronic Impedance spectra of the quasi solid state PANI//$NH_4V_3O_8.2.9H_2O$ 33

3.7. Ionic conductivity, stress strain curves and adhesion for quasi solid state electrolytes. 34

3.8. Ex situ XRD spectra of the $NH_4V_3O_8.2.9H_2O$ cathode. 35

3.9. Ex situ XPS spectra for V 2p and N 1s at pristine, charged and discharged state..... 36

3.10. Fabrication of the flexible AIB and electrochemical perfomance 37

4.1. Synthesis procedure of Vanadium oxide with intercalated PANI. 42

4.2. XRD and Raman spectra for HVO, PVO10, PVO60 and PVO180..... 43

4.3. SEM image, EDS, and XPS spectra for PVO60 and HVO 45

4.4. The O 1s XPS spectra of a) HVO and b) PVO60. 46

4.5. CV curves of PVO60, HVO, PVO10, and PVO180, at a scanning rate of 5 mV/s 47

4.6. Electrochemical perfomance of HVO, PVO10, PVO60 and PVO180 48

4.7. CV curves of PVO60 and capacitive contriburtion calculation 50

4.8. CV curves of HVO at different scan rates from 1mV/s to 10mV/s. 51

4.9. XRD patterns of PVO60 at various charge/discharge states. 52

5.1. SEM, EDS spectrum, EDS mapping, Raman spectrum, and XPS N 1s spectrum of PPY.... 60

5.2. Linear Sweep Voltammetry curves, Raman spectra and NMR spectra for electrolytes..... 61

5.3. CV curves, Rate capability, and cycling for PPy in NH_4Ac and KAc electrolytes 63

5.4. Electronic Impedance Spectra for PPy electrode in NH4Ac and KAc electrolytes. 65

5.5. Electrochemical perfomance of PPy in NH_4Ac and KAc electrolytes. 67

5.6. Ex-situ XPS N 1s spectrum of PPy at pristine, charge, and discharge state,..... 69

5.7. Schematic of the metal-free ammonium-ion full battery based on PPY/PANI electrodes.... 70

5.8. CV curves of PPy and PANI in 25 m NH_4Ac electrolyte at 0 °C..... 70

5.9. Electrochemical performances of the PANI/PPy AIB with 19 m NH_4Ac at 0° and 25°C.... 71

5.10. GCD curves and rate capability for full PANI/PPy cell at 25 and 0°C…… …..78

Abbreviations

CV	Cyclic Voltammetry
EIS	Electronic Impedance Spectroscopy
EDS	Energy dispersive spectroscopy
PVDF	Polyvinylidene fluoride
SEM	Scanning electron microscopy.
TEM	Transmission electron microscopy
XRD	X-ray diffraction
XPS	X-ray photoelectron microscopy
SEI	Solid electrolyte interface
LIBs	Lithium-ion batteries
AIBs	Ammonium ion batteries
WISEs	Water in Salt Electrolytes

Abstract

The Lithium-ion battery (LIBs) system has dominated the battery market because of its superior energy and power density. Problems related to LIBs such as safety, scarcity of cobalt and lithium have led researchers to explore alternative battery systems. NH_4^+ ion is a nonmetal charge carrier with lower molar mass (18 mol g^{-1}) and smaller hydrated ionic size (3.31 Å) which results in excellent electrochemical properties. Furthermore, NH_4^+ ion has a tetrahedral structure that has no preferred orientation as compared to spherical metal ions giving a different intercalation chemistry based on hydrogen bonding. These properties present physical characteristics for NH_4^+ ion to be an effective charge carrier.

This research outlines the development of high performance NH_4^+ ion batteries (AIBs), in terms of anode, cathode, and electrolytes to enhance their electrochemical performance. The first chapter presents polyaniline (PANI) which is facially synthesized by oxidative polymerization resulting in high surface area, improved conductivity, and high-capacity material for NH_4^+ ion storage. We further explored a quasi-solid-state electrolyte in the second chapter based on xanthan gum for application in a flexible AIBs based on $NH_4V_3O_8 \cdot 2.9H_2O$ nanobelts cathode and PANI anode. The full cell showed high-capacity retention when bent at different angles illustrating high structural integrity maintaining good electrochemical properties. Chapter 3 an in-situ intercalation technique is used to synthesize polyaniline-intercalated vanadium oxide (PVO) with a nanoflower morphology for increased surface area and enhanced NH_4^+ ion (de)intercalation kinetics. The interlayer spacing was expanded between V-O layers offering large diffusion channels to accommodate NH_4^+ ions. The diffusion kinetics of the NH_4^+ ions, influenced by the hydrogen bonds formed between NH_4^+ ion and O^{2-} in the host structure, were enhanced by the unique π-conjugated structure of PANI, leading to high capacity. The last chapter presents a metal free all organic AIB, that can operate at a low temperature of 0°C based on Polypyrrole (PPy) and PANI with 19m NH_4CH_3COO water in salt electrolyte (WiSE) . Additionally, the physiochemical properties of NH_4^+-based WiSEs are examined by Raman and nuclear magnetic resonance (NMR) spectroscopies, to explore their electrochemical behaviors and the fundamental effect of salt concentration on the electrolyte characteristics.

Chapter 1. Introduction

1.1 Background

Since the 19th century, most of the energy used by humanity primarily comes from burning fossil fuels. Currently, in the world over 80% of the total electricity generated is produced from fossil fuels such as coal, natural gas, and petroleum. In 2016 burning of fossil fuels to meet energy demand contributed about 73.2% of the 49.4 billion tons of CO_2 towards greenhouse gas emission. As the population continues to increase energy consumption is expected to grow by 50% between 2023 and 2050. [1] Transportation is the main sector that is heavily reliant on fossils fuels at 96.7%, and with the projection that oil will run out in 50 years, and coal in 114 years, an energy crisis is imminent. [2] For human sustainability renewable energy technology such as biofuels, thermal energy, solar power, wind energy is the only solution and has grabbed attention as these energy sources are environmentally friendly. But for the full exploitation to reach maximum potential of these renewable energies, the main drawback has been the lack of high-performance energy storage devices to store energy from these technologies. Much progress has been made in energy storage devices based on their working principle and have been divided into fuel cells, supercapacitors, and batteries.

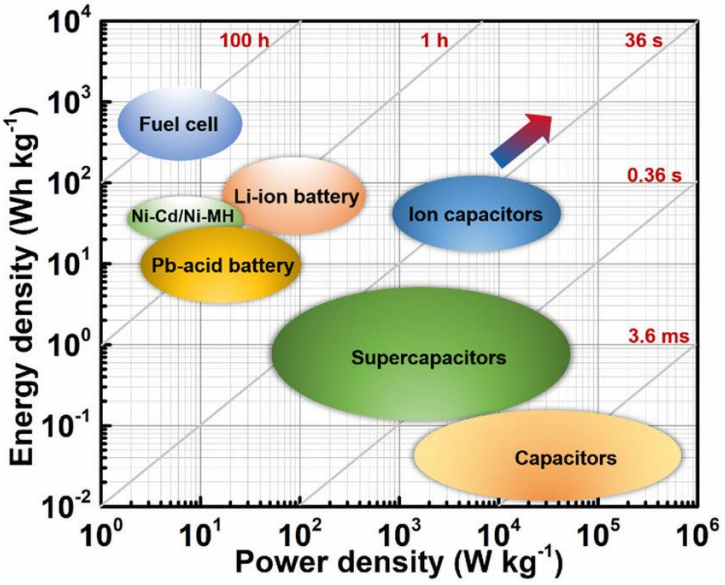

Figure 1.1. Ragone plot showing the comparison of energy density and power density for different energy storage devices. Reproduced with permission.[3] Copyright 2014, American Chemical Society.

Figure 1.1 shows the Ragone plot for energy density and power density for different energy storage devices. From the plot batteries offer the best qualities in terms of energy and power density i.e. in the smallest size. Battery technology is the best invention ever when it comes to the

storage of green energies. Over the past decades scientists have developed battery systems such as Pb-acid, Ni-Cd, Na-S and Li-ion batteries. Among them Li-ion batteries (LIBs) are considered as the most superior in energy storage. LIBs are superior to other battery technologies because they have the highest energy density and power density as a combination, which means they can deliver large amounts of current for high power applications in the smallest size. The advancement of technology has led to high demand for the storage of electric power not only for fast portable electronics and electric vehicles but more importantly for the full exploitation of renewable energy sources.[4] Ever since the commercialization of LIBs (C/LiCoO2) in 1990s, they have taken over majority of the battery market owing to a high charge capacity, power and an excellent cycle life as compared to other battery systems. The award of the 2019 Nobel Prize in Chemistry to John Goodenough alongside Stanley Whittingham and Akira Yoshino, shows how Li^+ ion redox chemistry was a breakthrough in energy storage.

The successful commercialization of lithium-ion batteries (LIBs) provided a new approach for tackling the energy crisis. [5,6, 7, 8, 9] However, despite the best performance of LIBs, it has been reported with issues such as the safety e.g., battery explosions caused by forced increase of internal material chemistry parameters. The safety problems are mainly caused by high voltage causing overcharge, high temperature causing thermal runaway, high pressure from internal gas generation from electrolyte and high current causing dendritic lithium to short-circuit. [10] These issues cause LIBs to explode, and it has become a concern when it comes to their use in electronic gadgets and electric vehicles. When it comes to raw materials used to fabricate LIBs it has been reported that at the current rate of consumption of lithium and cobalt, they will become scarce leading to price increase of LIBs for example in electric cars LIBs make up 30 – 40% cost of an electric vehicle.[11] Furthermore, there has been several cases reported of human exploitation in the mining of lithium and cobalt, as well lack of proper handling from mining companies causing contamination of rivers and soils. [1] Li^+ ion is a metallic charge carrier and because of all the above-mentioned aspects have led researchers to explore other metallic charge carriers such Na^+, K^+, Mg^{2+}, and Zn^{2+} as alternative effective charge carrier in batteries.

Magnesium metal has a low reduction potential of -2.37V vs standard hydrogen potential (SHE) , a high volumetric capacity of 3833 mA h cm^{3}, cheaper and its 8th most abundant element on earth, all these properties make it more attractive to develop high performance magnesium ion batteries (MIBs). Mg^{2+} ion has an ionic radius of 0.72Å which is almost like Li^+ ion of 0.76Å but because of high electric density of Mg^{2+}, there is a high polarization which causes sluggish ion kinetics in cathode materials. The existence of a stronger electrostatic interaction between divalent Mg^{2+} ion and host ions will impede the ion transport kinetics resulting in poor electrochemical performances and low battery specific capacity.[12 13] Aluminum, Al^{3+} is also an attractive choice of an effective charge carrier as it is abundant and has lower reactivity. Al^{3+} ion redox chemistry involves three electron transfer redox processes which leads to high charge/discharge capacity.[14 15] When compared to Li^+ ion, aluminum has four times higher volumetric capacity of 8.04 A h cm^{-3} more than any other metallic charge carrier. However, Al^{3+} ion batteries (AIBs) have unsatisfactory electrochemical performances because of corrosion in aqueous electrolytes which results in an inactive electrochemical layer ion the electrode surface affecting the cell electrochemical performance. Other factors such as restrictions on few cathode materials to choose form, electrolytes, insufficient life cycle remain a challenge to improve their performances. Lastly,

Zn^{2+} ion redox chemistry has gained traction and offered the best performance batteries than any alternative metallic charge carrier. Zinc has a high theoretical capacity (820 mA h g^{-1}), a lower redox potential of 0.76 V vs. SHE and is very stable in water due to high overpotential for hydrogen evolution. Zn^{2+} ions have an ionic radii of 0.74Å almost like Li^{+} ion but it has a higher atomic mass, higher positive polarity. These properties affect the Zn^{2+} ion transport kinetics in different cathode material therefore reported high-capacity Li^{+} ion storage materials cannot be applied for Zn^{2+} ion storage. Despite these facts a very good high-rate performance and cycling stability has been achieved in ZIBs. Problems such as dissolution of elements, self-aggregation, and phase change during Zn^{2+} intercalation remain a challenge for commercialization of ZIBs.

1.2 Motivation and NH_4^+ Ion as a Charge Carrier in Batteries

Ever since the discovery of lithium ion topotactic intercalation in battery systems most of the efforts towards substituting Li-ion in battery systems have been focused on use of metal ions as effective charge carrier such as Mg^{2+}, Na^{+}, Zn^{2+}, Al^{3+}, K^{+} etc. The historical disregard for nonmetal cations (NH_4^+, H_3O and H^{+}) as charge carriers in electrochemistry is not justified and has blinkered battery research. This notion assumes that the interaction between ion and electrode material is purely ionic, leading to researchers forget another dimension of bonding in chemistry such as hydrogen bonding with covalent in nature exhibited by these nonmetal charge carriers can play a crucial role in electrochemistry. Protons (H^{+}), hydronium ions (H_3O^{+}), and ammonium ions (NH_4^{+}) as effective charge carriers in electrochemical energy storage systems is still in its infancy. These nonmetal ions have the advantage that materials used to synthesize these ions are safe, light, inexpensive, environmentally friendly, and even more widely available than metallic charge carriers as they could be synthesized from infinite or unlimited sources i.e., nitrogen and hydrogen in air. These nonmetallic charge carriers exhibit some hydrogen bonding with some covalent nature with the electrode, thus opening another dimension of chemistry that secondary bonding can play a crucial role in electrochemistry. This challenges the premise based on metallic topochemistry that the interaction between the ion and the electrode is purely ionic.

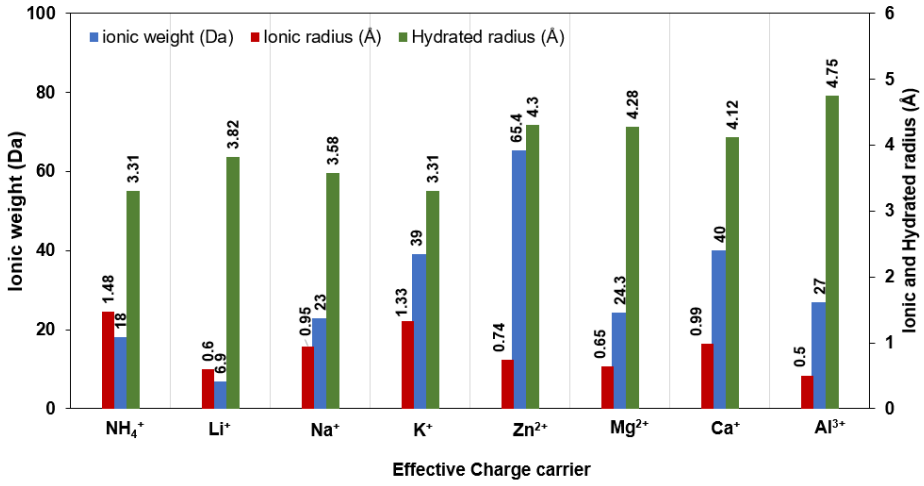

Figure 1.2. Comparison of ionic weight, cation radius, and hydrated radius of the NH_4^+ ion and metallic charge carriers

Of these mentioned nonmetal charge carriers, NH_4^+ ion presents the most attractive properties for electrochemical storage as compared to other monovalent ions such as Li^+, Na^+, K^+. As illustrated in figure 1.2 NH_4^+ ion has low molecular weight of 18 g mol^{-1} which is an important property to get high energy density.16 Secondly, in aqueous solutions charge carriers i.e., ions exist as hydrated ions. NH_4^+ ion has an ionic radius which is large 1.48Å , but it's hydration size of 3.31Å vs 3.82 Å for hydrated Li^+, 3.58 Å for hydrated Na^+ and 3.31 Å of hydrated K^+ ion.17 results in fast ion diffusion in aqueous electrolyte as compared to other charge carriers which results in excellent rate capability.[100]In an aqueous electrolyte, NH_4^+ ion presents milder acid-base environment than Na^+, K^+ and H_3O^+ which helps to alleviate the corrosion of electrode materials and lower potentials for the hydrogen evolution reaction (HER) . Ammonium salts are highly dissociated which results in high ionic mobility leading to improved conductivity. [18,19] Furthermore, NH_4^+ has a tetrahedral structure that has no preferred orientation as compared to spherical metal ions giving a different intercalation chemistry as compared to the metal ions in cathode materials. NH_4^+ ion can form hydrogen bonds with host material offering a different topo-coordination chemistry when compared to metal ions (Li^+, Na^+ and K^+) which contributes to different bonding chemistry.

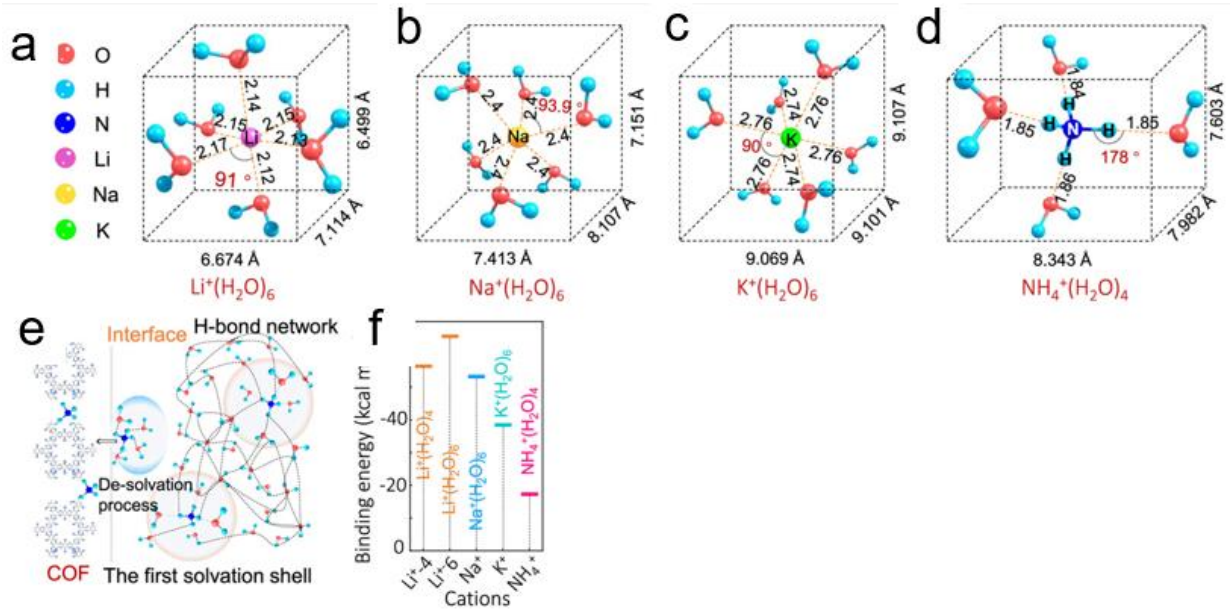

Figure 1.3. Solvation behavior of monovalent ions. a) Li^+ $(H_2O)_6$ b) Na^+ $(H_2O)_6$ c) K^+ $(H_2O)_6$ d) $NH_4^+(H_2O)_4$ Reprinted from Ref. 20 with permission from American Chemical Society (JACS)

Solvation behavior of an ion in solution affects the electrochemical performance for electrolytes from 2 considerations i.e., the kinetics of ion transportation in solution and secondly the thermodynamic desolvation process.[21, 22] Tian at al. did Gaussian simulation to understand the solvation of structure of Li^+, Na^+, K^+ and NH_4^+ ion only the first solvation shell was considered. The calculation of solvation volume as shown in figure 1.3 (a-d) shows NH_4^+ ion having a larger solvation size in comparison to Li^+ and Na^+, even though NH_4^+ ion has the smallest coordination number with water molecules of 4 vs 6 for Li^+ and Na^+ ions as shown in figure 1.3. Despite having

a larger solvation size, the NH_4^+ ion has the loosest solvation structure mainly because the weak H-bond with water molecules compared to the rigid metal ion coordination bond of Li^+ and Na^+ ions. This is because the bond angle N−H···O bond in the $NH_4^+(H_2O)_4$ is 178° which is larger in comparison to Li−O bond in $Li^+(H_2O)_4$ which is 110°.[20] When desolvation happens the cations exclude water molecules before they intercalate into the electrode material as illustrated in figure 1.3 e. Desolvation process, is when solvated cations exclude the coordinated water molecules in solution before ion electrode interaction which results in redox reactions. This process is nonspontaneous, and energy is required for the process to occur, therefore the weakest solvation shell accelerates the desolvation process requiring lower energy. As such the $NH_4^+(H_2O)_4$ has the lowest desolvation energy as shown in figure 1.3 f , affording NH_4^+ ion more energy to accept electrons hence achieving higher redox potential as compared to Li^+ and Na^+ ions.[53]

1.3 Cathode Materials for Ammonium Ion Storage

Many electro active materials have been shown to store NH_4^+ ions with considerable capacity, such Prussian blue analogues ($A_xL_y[M(CN)_6]_z{\cdot}nH_2O$,) that have a an open structure and framework, whose geometry is excellent for ionic transport and rate capability. Their open structure is suitable for allowing the large ionic radius (1.48Å) of the NH_4^+ ion. The PBA framework results from the transition metal ion bonded to 6 nitrogen and carbon atoms to form the -C ≡ N- bonds. Most of the reported PBAs have limited capacity and their long-term cycling performances are very unsatisfactory as shown in the table. Listed below are the typical storage capacities and their working potential ranges.

Table 1. Electrochemical Performances of Various PBAs as Ammonium Ion Battery (AIB) cathodes

Cathode Material	**Potential Range**	**Electrolyte**	**Capacity ($mAhg^{-1}$) / Specific Current ($mA\ g^{-1}$)**	**Reference**
CuHCF	0.16 - 1.4 V vs. S.H. E	0.5 M $(NH_4)_2SO_4$	55/500	23
Ni-APW	0.2 – 0.9 V vs. Ag/AgCl	1 M $(NH_4)_2SO_4$	51.3/300	24
N-CuHCF	0.5 - 1.0V vs. SCE	0.01 M $Cu(NO_3)_2$ +2.0 M NH_4NO_3	53.1/1000	25
MnHCF	0 – 1 V vs. Ag/AgCl	1 M NH_4TFSI	104/100	26
Berlin Green	-0.2 – 1.2V vs. Ag/AgCl	0.5 M $(NH_4)_2SO_4$	80/5000	27
$Fe_4[Fe(CN)_6]_3$	0.1 – 1 V vs. Ag/AgCl	1 M $(NH_4)_2SO_4$	40/1800	28

(table cont'd.)

Cathode Material	**Potential Range**	**Electrolyte**	**Capacity (mAhg$^{-1)}$ / Specific Current (mA g^{-1})**	**Reference**
NaFeIII [FeII(CN)6]	0.2 – 0.8 V vs. Ag/AgCl	1.0 M $(NH_4)_2SO_4$	60/250	29
Na1.45Fe[Fe(CN)6]0.93	-0.1 – 0.9 V vs. Ag/AgCl	1.0 M $(NH_4)_2SO_4$ + 20 mM $ZnSO_4$	75/250	30
K0.9Cu1.3Fe(CN)6	0.4 – 1.4 V vs. Ag/AgCl	0.5 M $(NH_4)_2SO_4$	60/50	31

In various electrochemical systems transition metals have been used as electrode materials because of their large open structure, wide interlayer spacing and the ability to change oxidation number during electrochemical reactions. For example, Vanadium can change its oxidation state from +2 to +5 showing the capability of multielectron transfer thus achieving high capacity.

Table 2. Electrochemical Performances of various PBAs as Ammonium Ion Battery (AIB) cathodes

Cathode	**Potential Range**	**Electrolyte**	**Capacity (mAh g$^{-1)}$ / Specific Current (mA g^{-1})**	**Reference**
V_2O_5	-0.2-0.8 V vs. Ag/AgCl	0.5 M $(NH_4)_2SO_4$	70/5000	36
MnO_x	0 – 0.8 V vs. Ag/AgCl	0.5M NH_4Ac	175/500	32
$Fe_5V_{15}O_{39}(OH)_9 \cdot 9H_2O$	-0.4 – 1.2 V vs. Ag/AgCl	0.5M $(NH_4)_2SO_4$	130/100	33
$NH_4V_3O_8$	0 – 1 V (Full cell)	1 M $(NH_4)_2SO_4$	110/100	34
Hetero-VS_2/VO_x	-0.6 – 0.9 V vs. Ag/AgCl	5 M $(NH_4)_2SO_4$	200/100	32

Dong et al. reported a high-rate reversible NH_4^+ ion (de)intercalation in a bi-layered V_2O_5 in which a good reversible capacity of 100 m Ah g^{-1} at a specific current of 0.1 A g^{-1}, capacity retention of 80% after 30 000cycles at 5 A g^{-1} . [35] Furthermore, the pseudocapacitive behavior of NH_4^+ was compared to K^+ ions since they have almost similar characteristics ionic radii of NH_4^+ ion is 1.48Å coordination number (CN) 6 and K^+ ionic radii of 1.38Å and CN 6. Through density functional theoretical calculations, X-ray Spectroscopy (XPS), Fourier-transform infrared spectroscopy (FTIR) and Raman spectroscopy characterizations they revealed that NH_4^+ have a

unique directional bonding with the host as compared to K^+, Li^+ and Na^+ that have no preferred orientations. The NH_4^+ ion has a tetrahedral shaped multipole hence during migration within the bi-layered V_2O_5 the NH_4^+ ion can twist and rotate to keep set of coordinated hydrogen bonds with oxygen atoms in the V-O framework, because of this mechanism NH_4^+ ion had a higher capacity of 103 mA h g^{-1} versus 63 mA h g^{-1} for K^+ ion at a same specific current of 0.1 A g^{-1} and same potential window of -0.2 – 0.8 V (V vs Ag/AgCl). NH_4^+ ion storage mechanism was compared to K^+ ion in which as they illustrated that the -pseudocapacitive behavior of NH_4^+ storage was stronger and faster than that of K^+ ion and proposed a monkey-swinging model was proposed. NH_4^+ ion can form hydrogen bonds with the V=O structure in the VO framework, whilst the K^+ ion like metallic ions will forms ionic bonds with the host materials, which results in the lower Gibbs free energy for the ion electrode system for hosting NH_4^+ ion than K^+.

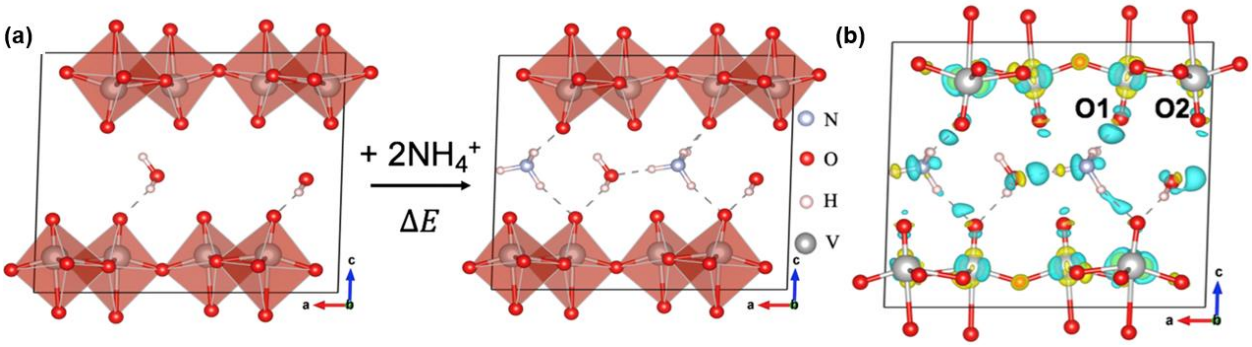

Figure 1.4. (a) Lowest energy configurations for $V_2O_5{\cdot}0.5H_2O$ with intercalating NH_4^+ (b) Plots of energy difference from the intercalation of the NH_4^+ ion showing charge transfer through the V=O bond to an H·····O=V bond (blue cloud). Thus, oxidizing the attached V-Ion (the yellow core underneath outer blue lobes of the V-ion. Reprinted from Ref. 38 with permission from Elsevier.

By performing Density functional Theory (DFT) calculations the lower energy model structure of the $V_2O_5{\cdot}0.5H_2O$ with different NH_4^+ and H_2O in the intercalated layer. As shown in Figure 1.4a and b the intercalated NH_4^+ ions forms hydrogen bonding with both the V_2O_5 layers as well as with the crystalline water. The bonding between the NH_4^+ ion and the host structure can be confirmed to be hydrogen bonding as they are in the range of 1.86-1.99 Å. The V=O bond is stretched to 1.67 from 1.61Å after intercalation demonstrating a different ion electrode interaction with have been assumed to be ionic. Other materials such as MnO_x and MoO_3 have been shown to exhibit similar hydrogen bonding during the intercalation with the NH_4^+ ion.

1.4 Full Cells

Figure 1.5 shows the Ragone plot for full rocking chair AIBs up to date whose performance is compared to Lithium-ion batteries, lead acid batteries, and capacitors. The full cells assembled from various electroactive materials whose an average nominal voltage of 1V and specific capacity

of 50 mA h g^{-1} which needs improvement as compared to lithium-ion battery that has a nominal voltage of 3.7V and capacity of 750 mA h g^{-1}. From figure 1.5 the ALO//Ni-APW system presented the best performance with an energy density of 45 W h g^{-1} and power density of 2250 W kg^{-1} whose power density does not decrease when the power density increases. This is superior as compared to other AIBs but more improvement is required to be comparable to LiBs or ZIBs.

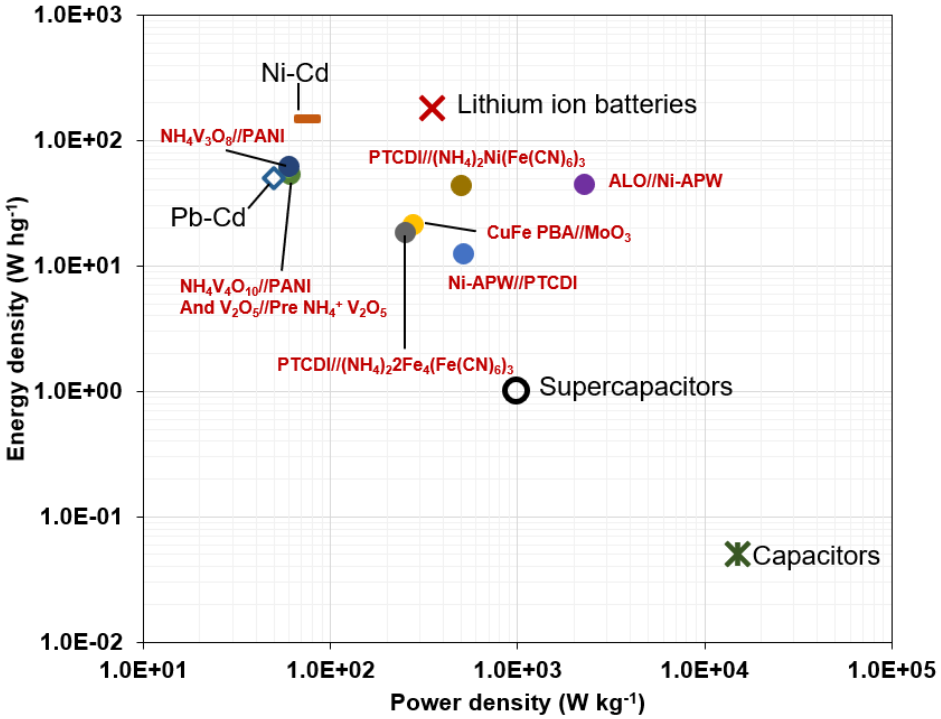

Figure 1.5. Ragone plot showing the comparison of energy density and power density for different ammonium ion batteries up to date with conventional energy storage devices such as LiBs, supercapacitors, capacitors, and lead acid batteries.

1.5 Motivation and Scope

Though progress has been made in the NH_4^+ -ion battery redox processes, its electrochemical performance does not match its counter-part metal-ion battery such as LIBs or ZIBs. Therefore, more research is needed for NH_4^+-ion batteries before they can be commercially viable, particularly with respect to finding high-capacity electrode materials. The main obstacles in the fabrication of full NH_4^+ cells are firstly the NH_4^+ ion has the smallest hydration ionic size which results in fast ion migration in aqueous electrolytes, however NH_4^+ ion has a large ionic radius, which requires the host materials to have an open or flexible structure that can accommodate the ions during charging and discharging. Secondly most of the cathode materials do not have NH_4^+ ions in their structure, and solution would be to find a method to ammoniate the anode or cathode before battery assembly. The cathode and anode materials should meet the following conditions for a high-performance battery. Firstly, the materials should be low cost and environmentally friendly to enable large scale battery manufacturing. Secondly the anode and

cathode materials should have high electronic conductivity and higher charge NH_4^+ diffusion coefficient for the fast transport of the NH_4^+ ions leading to excellent rate capability. Thirdly cathode materials should be able to accommodate a large amount of NH_4^+ ions without structural failure which leads to high specific capacity and long cycle life. Lastly, for the battery to be used practically in different conditions such as wearable devices, and use in extended wide temperature ranges the electrolytes, cathode and anode materials should be stable in these condition without the battery failing. In all these mentioned aspects NH_4^+ ion battery still needs to be improved from the cathode, anode and electrolytes to compete with their counterparts such as ZIBs and LiBs. In this regard, developing novel cathode and anode materials of high conductivity, high specific capacity and good rate capability underlie the construction of high-performance NH_4^+ ion full cells. Furthermore, to realize the full potential of the ammonium ion battery its electrolyte must be facially tuned and optimized to maximize ionic conductivity and transport kinetics. NH_4^+ ion redox chemistry also provides another dimension of chemistry which is the nature of the interaction between the ion and electrode, which is largely assumed to be purely ionic. My work focuses on the development of novel aqueous ammonium-ion batteries with intrinsic safety and enhanced performance, with particular attention to design and synthesize of nanostructured materials with high capacity for NH_4^+ storage and the tuning and optimization of the electrolyte to develop high performance ammonium ion batteries.

This dissertation contains 6 chapters detailing my research achievements during my doctoral program which research projects on synthesis of high-performance cathode/anode nanomaterials and facially tuned electrolyte with desirable structures, morphologies, and compositions for improved performance NH_4^+ ion batteries.

In Chapter 1, an overview of energy storage systems is presented starting from the development of the lithium-ion rechargeable battery and discussion on alternative metallic battery systems being developed to replace lithium-ion battery, followed by the chemistry of development of the NH_4^+ ion as an effective charge carrier in battery systems. Furthermore, an overview of the developed cathode materials so far is presented and lastly the current challenges to develop high perforce ammonium ion batteries that need to be addressed.

High performance, low cost and high specific capacitance are the factors to consider when designing cathode materials. Chapter 2 focuses on the synthesis and development of the polyaniline cathode nanomaterial for enhanced capacity for NH_4^+ storage. The polyaniline with high surface area is synthesized and doped with Cl^- ions to enhance its electrochemical properties. The electrochemical performance of the as prepared polyaniline is evaluated for NH_4^+ ion storage. A facile method is used is to prepare emeraldine salt polyaniline (ES-PANI) and it exhibited a high capacity of 160 m Ah g^{-1} at a specific current of 1 A g^{-1} as compared to undoped polyaniline in the form of emeraldine base polyaniline (EB-PANI) showing 120 $mAhg^{-1.}$

Electrolytes play a pivotal role in batteries as they serve as ionic transportation between anode and cathode, and to a greater extent determine the electrochemical performance of the battery such stable electrochemical window and ionic conductivity. Aqueous electrolytes are not suitable for use in flexible devices because of potential hazards such electrolyte leakage and

evaporation of electrolytes. Gel polymer electrolytes have immobilized liquid electrolyte in the gel matrix, and they possess better mechanical integrity. In Chapter 3 we present a full flexible ammonium ion battery composed of a concentrated hydrogel electrolyte, which was synthesized using ammonium sulfate, xanthan gum and water. The gel electrolyte is facilely tuned and optimizes the salt concentration in the electrolyte, to maximize its ionic conductivity and transport kinetics. It is found that the battery based on the electrolyte prepared using 3 M ammonium sulfate solution exhibits the best performance. The new electrolyte, which is optimized, allows the fabrication of flexible ammonium ion battery with excellent electrochemical performance when bent at different angles, demonstrating remarkable mechanical strength and flexibility.

To improve the capacity for polyaniline we synthesized a composite of polyaniline and V_2O_5. Chapter 4 reveals an in-situ intercalation technique utilized to synthesize polyaniline-intercalated vanadium oxide with a nanoflower morphology for increased surface area and enhanced NH_4^+ ion (de)intercalation kinetics. It summarizes the diffusion kinetics of the NH_4^+ ions, enhanced by hydrogen bonds between NH_4^+ ion and O^{2-} in the V-O framework, which are effectively enhanced by the unique π-conjugated structure of PANI, leading to high capacity, improved rate capability and improved cycle life. The as-prepared PANI-intercalated V_2O_5 (PVO) shows NH_4^+ ion electrochemical storage based on hydrogen bond chemistry with the electrode material as elucidated by X-ray photoelectron spectroscopy and Raman spectroscopy characterizations.

For practical application of batteries, the battery system should be able to function at low temperature as well without losing it electrochemical properties. The most important aspect for batteries to function at low temperature is electrolyte. At low temperatures the electrolyte tends to freeze affecting the mobility of ions leading to very low capacity. Additionally, the anode and cathode materials need to withstand low temperatures without structural failure and losing their electro active properties. Chapter 5 reports a metal free battery all organic NH_4^+ ion that can operate at a low temperature of 0°C by using Polypyrrole as the cathode, polyaniline as the anode in 19m electrolyte. We demonstrate Polypyrrole as a high-capacity storage material for NH_4^+ ion storage and the electrochemical stability of polyaniline and Polypyrrole at low temperatures. Furthermore, we explore the physiochemical properties of the NH_4^+-ion based WISEs using Raman and nuclear magnetic resonance (NMR) spectroscopies.

Chapter 5 provides my main research co the main conclusions on the development of novel aqueous ammonium ion battery with intrinsic safety.

Chapter 2. Superior Polyaniline Cathode Material with Enhanced Capacity for Ammonium Ion Storage

2.1 Introduction

Organic compounds have been explored for electrochemical storage due to their structural diversity and molecular-level controllability and have been utilized as cathode materials in different battery systems such as lithium ion batteries because they can store cations in their conjugated chemical bonds during the discharge process.[36,37]Among them, PANI has been of great interest due to its high conductivity, reversible convertibility between redox states during charge and discharge processes, environmentally friendliness, low cost and easy synthesis through chemical and electrochemical methods. [38]In this chapter we present the synthesis of PANI for use as cathode material for NH_4^+ storage. PANI has a different doping mechanism and structure in comparison with other conductive or semi-conductive polymers. Unlike in other conductive polymers where the number of electrons change during doping, number of electrons do not alter in PANI when doped with protons in acidic solutions through a non-redox process. [39]During doping in PANI, a proton bound to a N atom of the quinone group in the PANI chain reduces the quinone ring to benzene ring, resulting in its being positively charged. To maintain charge neutrality and an anion will be attracted to the polymer chain.[40] PANI has three oxidation states which are fully reduced leucoemeraldine base (LEB), half oxidized emeraldine base (EB) and fully oxidized pernigraniline base (PE). PANI can converted between these oxidation states either by oxidation or reduction, which alters it color and properties.[41]

Protonation of EB in the quinoid and benzenoid rings results in the formation of polarons, which consequently improves the conductivity of PANI, while protonated PE or LEB are insulating, due to the irregularity in their polymer chains and much less chance of polaron formation as a result. [42, 43] Oxidized PANI has a positively charged nitrogen group $C\text{-}N^+$ which can store anions and the cations can be stored on the electronegative nitrogen $C\text{-}N^-$ in the protonated PANI .[44] It has been reported that PANI is capable of anion storage. Cuipin Han and coworkers demonstrated conductive PANI can be used for capacitive storage of PF_6^- through doping and dedoping reactions.[45] H. Gao et al. revealed that the anion component from a salt electrolyte of KPF_6 is intercalated into PANI cathode upon charging and de-intercalated during discharging while K^+ is stripped on the potassium-metal anode.[46] Quinton et al. discovered that the redox and attachment properties of anions are dependent on the nanoscale thickness of PANI. It was found that the PANI films of thickness less than 10 nm have an excellent chloride ion uptake which is important for desalination application, and the PANI films with a thickness of approx. 100nm have excellent capacity in SO_4^{2-} solutions because the proton donor/acceptor will be SO_4^{2-}/HSO_4^- in the PANI.[47]

This chapter previously appeared as: Kuchena, Shelton Farai, and Ying Wang. "Superior polyaniline cathode material with enhanced capacity for ammonium ion storage." *ACS Applied Energy Materials* 3, no. 12 (2020): 11690-11698. Copyright 2020 American Chemical Society. https://pubs.acs.org/doi/full/10.1021/acsaem.0c01791

Polyaniline-based compounds have been shown to be excellent electrode materials for chloride ion storage. For instance, polyaniline-intercalated iron oxychloride was reported to serve as a cathode material in the chloride ion battery, showing a reversible capacity of 120mAhg^{-1} with a capacity retention of 82% after 50 cycles.[48] A composite of chlorine doped PANI/carbon nanotubes (CNTs) was also found to provide a capacity of 80 mAhg^{-1} for chloride ion storage.[49] Computational studies and density functional theory calculations reveal that NH_4^+ ions can have hydrogen bonding with hosts. The strong hydrogen bonds formed by NH_4^+ ions with PANI can enhance the structural stability thus giving a higher theoretical capacity. The ratio of oxidant to monomer during the synthesis of a polymer affects its properties such as morphology and conductivity. [50,51,52] Doping PANI with anions results in improved electrochemical performance in a high-pH environment due to improved proton storage along its polymer chains. For the first time, we utilize emeraldine base state polyaniline (EB-PANI) and emeraldine salt state polyaniline (ES-PANI) electrodes for ammonium ion storage with high capacity. In addition, the intercalation of NH_4^+ion is shown to be reversible in the electrode ES-PANI doped with Cl^- ions, suggesting that NH_4^+ ion topochemistry can be used for energy storage.

This chapter presents polyaniline (PANI) is an excellent material for in NH_4^+ on storage, and thus further proves that NH_4^+ions can be used effective charge carriers in aqueous ion battery systems. A facile solution method is used to prepare emeraldine salt polyaniline (ES-PANI) on the carbon felts (CFs) as the cathode material. The battery cell based on the ES-PANI cathode material shows a good discharge capacity of 160 mAh g^{-1} at a specific current of 1 A g^{-1}. At 5 A g^{-1}, it shows a good capacity retention of 82% after 100 cycles and exhibits excellent rate capability. Furthermore, it is found that the ES-PANI/CFs washed with water deliver higher capacity than those washed with ethanol, because washing with ethanol causes the oligomers to dissolve in the solution and thus decreases the storage capacity of ES-PANI for NH_4^+ ion storage. The intercalation/deintercalation of NH_4^+ ion is shown to be highly reversible in the ES-PANI electrode doped with Cl^- ions, due to the stable redox properties of nitrogen in ES-PANI polymer chains. As such, this work sheds new insight into the exploration of alternative electrode material for ammonium ion storage which can lead to new electrochemical energy technology.

2.2 Experimental Section

In situ polymerization was carried out to polymerize ES-PANI on carbon felts (CFs) surface since the CFs have higher porosity than the more commonly used carbon cloth. After the full polymerization reaction, the CFs changed from the original black color to dark green, to form ES-PANI/CFs for application as the electrodes. This color change indicates the deposition of ES-PANI on the CFs. The electrochemical performance was tested in three electrode cells. This cell setup had a graphite rod as the counter electrode, silver chloride Ag/AgCl (in 1M KCl) as the reference electrode, and 0.5 M $(NH_4)_2SO_4$ solution as the electrolyte with a pH of approximately 5.3. The working electrode is the ES-PANI/CFs with no other conducting materials or binder. The mass loading on the CFs was approximately 1.5 mg cm^{-2}.

2.2.1 Material Synthesis

Synthesis of *emeraldine salt polyaniline carbon felts* was carried out using an in-situ polymerization method. [11, 53] CFs were weighed and placed in a beaker in which a solution containing 0.365 ml of aniline and 15 ml of 1M HCl was added and put under string. CFs of known mass were soaked into the combined solution and then placed in the ice bath to maintain low temperature in the range 0 to 5 °C and continuous stirring for 1 hour. After 1 hour of continuous stirring, an additional solution of 5 ml of 1 M HCl with dissolved 0.228 g $(NH_4)_2S_2O_8$ (APS) was introduced into the mixture drop by drop whilst under continuous stirring in an ice bath. After a few minutes, the colorless solution turned dark green, showing polymerization has occurred. After the reaction continued for 1 h, the ES-PANI/CFs were taken out and washed with deionized water, and then put in an oven for drying at 60°C for 12 hrs. The active mass material loading on the CFs was calculated to be approximately 1.5 mg cm ^{2}. The EB-PANI was obtained from the as synthesized ES-PANI powder which was immersed in 0.1M NH_4OH and stirred for 15hrs.The EB-PANI was then collected and washed and washed the deionized water then dried in an oven at 60ºC overnight. The slurry was produced in a mass ratio of 7:2:1 for Active material: Super P conductive carbon black: carboxymethyl cellulose (CMC) in DI water and the slurry was cast on carbon felts (CFs), followed by drying at 60ºC for 12 h.

2.2.2 Material Characterization

Scanning electron microscopy (SEM) imaging was done using a JSM -6610 LV SEM to study the surface morphology of the in situ polymerized PANI on the carbon felts. X-ray photoelectron spectroscopy (XPS) characterizations were carried out using a Scienta Omicron ESCA 2SR XPS. Raman spectra were obtained though the Renishaw in a Via Reflex Raman Microscope, which enabled chemical identification with a spatial resolution of 1µm. The surface area of ES-PANI and EB-PANI was performed through a Brunauer-Emmett-Teller (BET) experimental procedure at nitrogen condition.

2.3 Results and Discussion

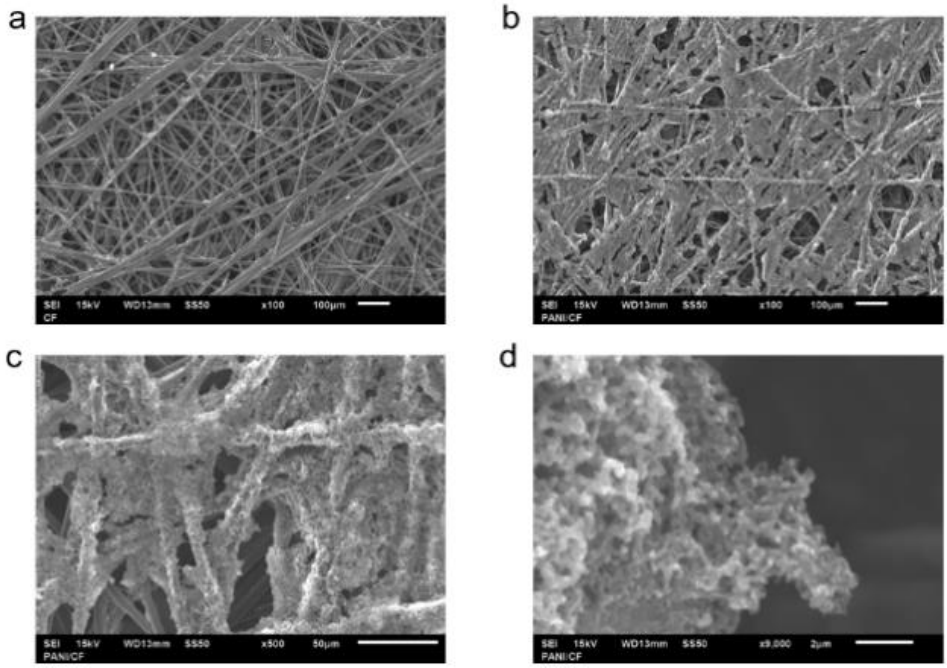

Figure 2.1. SEM images of (a) pure CFs without any ES-PANI coating and (b, c, d) ES-PANI-coated CFs coated at different magnifications.

Figure 2.1a shows the SEM image of bare CFs without ES-PANI coating. Carbon felts are cut from carbon paper which is formed from carbon fibers. Carbon fibers are known to have unique properties such as high mechanical strength, gas permeability, good electrical conductivity, and are thus often chosen to serve as current collectors.[54] Figure 2.1b-d present SEM images of ES-PANI-coated CFs at different magnifications, revealing the coating of ES-PANI on the surface in comparison with Figure 1a. Figure 1d further displays a nanothorn structure of ES-PANI well distributed on the surface of the CFs. This nanothorn structure is beneficial to the electrochemical performance of ES-PANI as it provides high surface area and short diffusion paths for redox reactions. The surface area was measured by BET experimental procedure under the nitrogen condition which showed surface areas of 38.9311 m^2/g 34.8328 m^2/g for ES-PANI and EB-PANI. These characteristics result in fast redox reaction kinetics and charge transfer which improves the electrochemical performance of ES-PANI and EB-PANI. The nanothorn structure grows on the nucleation sites of the carbon felts which are in contact with the solution because of the lower nucleation thermodynamic barrier with the solution.[55, 56] The nanothorn structure has an advantage over flat structure when it comes to bending, because it can endure larger strain when bent in comparison with the flat structure and thus helps to maintain the structural integrity of ES-PANI.

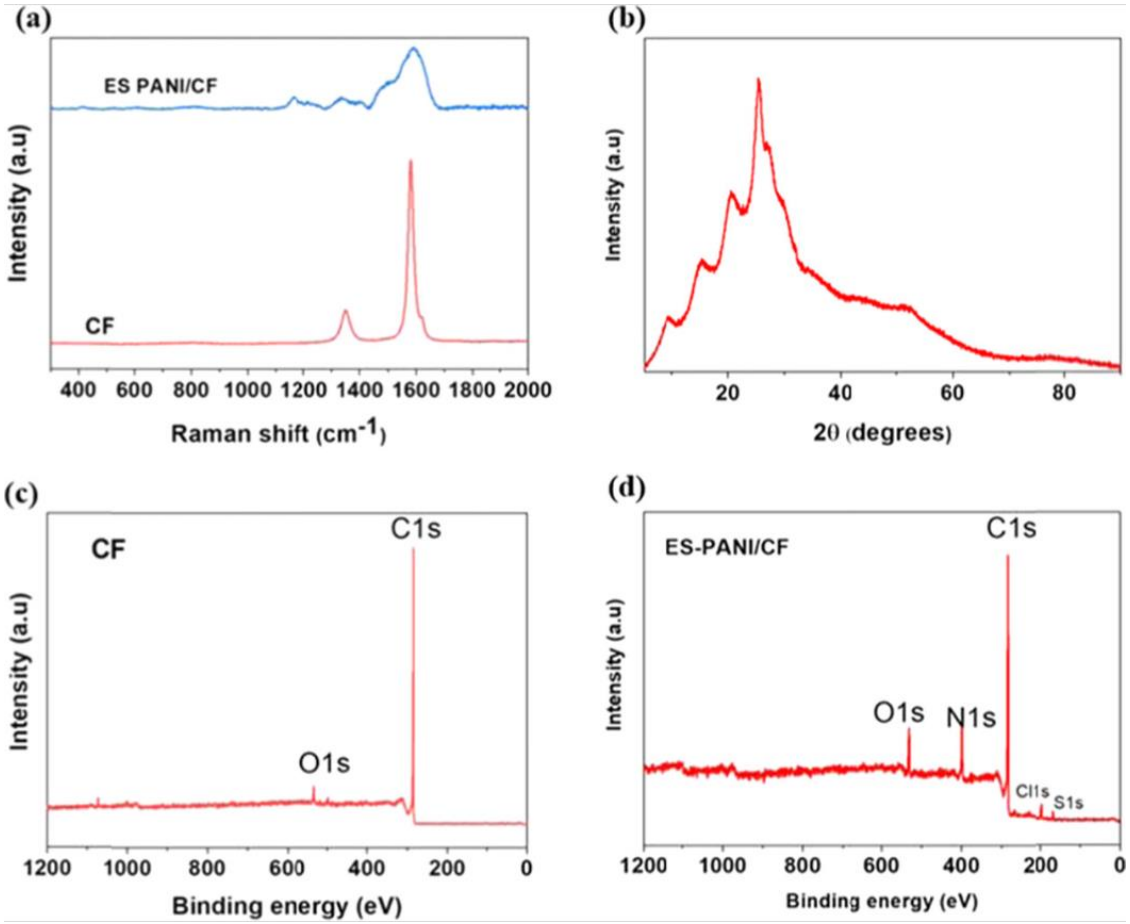

Figure 2.2. (a) Raman spectra of bare CFs and ES-PANI/CFs, (b) XRD pattern of polyaniline powders, (c) XPS spectra of bare CFs, (d) XPS spectra of ES-PANI/CF sample.

Figure 2.2a displays the Raman spectra of the ES-PANI/CF sample, revealing peaks at 1162.3 cm^{-1} which is C-H group bending vibrations of the quinoid ring, a peak at 1251.8 cm^{-1} is the C-H bending vibrations of the benzenoid ring, peaking at 1410.1 cm^{-1} corresponding to C=C stretching vibrations in the quinoid ring, peak at 1584.9 cm^{-1} for the C=C stretching vibrations of benzenoid ring and 1297.4 cm^{-1} for the stretching vibrations of $C\text{-}N^{+}$. As such, these results confirm the coating of ES-PANI on the CFs. The active material ES-PANI is washed with de-ionized water followed by drying at elevated temperature. In order to examine the crystallinity of the ES-PANI, its X-ray diffraction pattern is obtained. From the XRD pattern in Figure 2.2b, it is observed that ES-PANI is semi crystalline as evidenced by the broad peaks. [57,58] The Raman spectra results in Figure 2a are also confirmed by the XPS spectrum of the ES-PANI/CF sample in Figure 2.2d. The nitrogen intensity in ES-PANI/CFs is increased in comparison with pure CFs in Figure 2.2c due to the formation of ES-PANI on CFs. Cl element is also observed in the XPS spectra in Figure 2d owing to the formation of emeraldine salts.

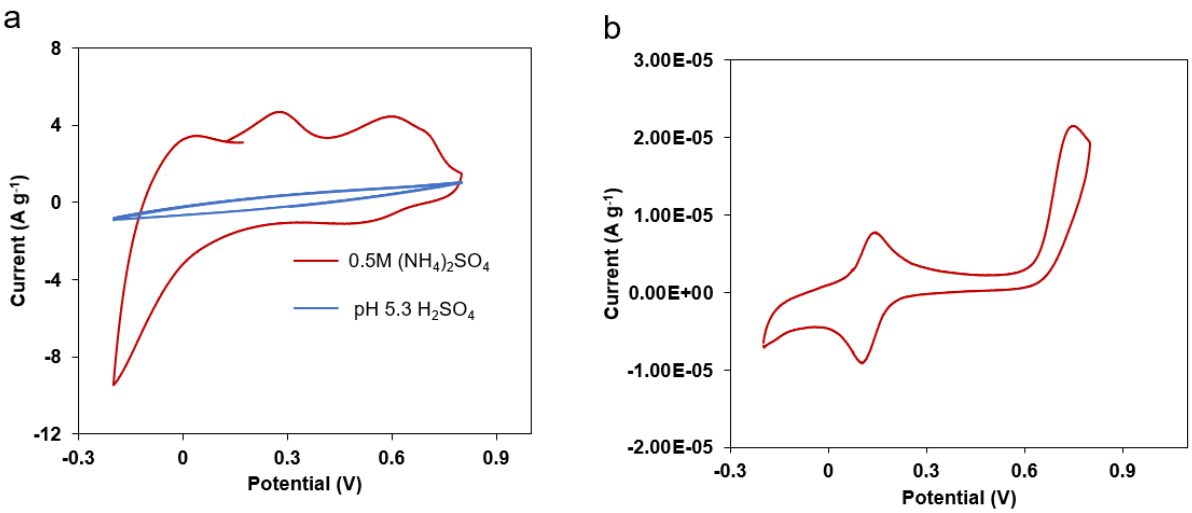

Figure 2.3. (a) The combined CV curve of ES-PANI/CFs electrode in the H_2SO_4 solution with pH 5.3 and of ES-PANI/CFs in 0.5M $(NH_4)_2SO_4$ at a scan rate of 5 mVs^{-1} b) The CV curve of pure CFs electrode in 0.5 M $(NH_4)_2SO_4$ at a scan rate of 5 mVs^{-1}.

The 0.5M $(NH_4)_2SO_4$ electrolyte has a pH of 5.3. Due to this mild acidic characteristic, we examine if protons or hydronium ions in the electrolyte contribute to the capacities of the electrode. Hence, a CV of the same three electrodes in a diluted H_2SO_4 solution at the same pH of 5.3 is measured, revealing that the CV current is very small and negligible compared to that of the electrode in the 0.5 M $(NH_4)_2SO_4$ electrolyte, as shown in Figure 2.3a. The area within the CV curve from H_2SO_4 solution is less than 2.0% that from the 0.5 M $(NH_4)_2SO_4$ electrolyte. To determine if CFs contribute to the capacity of the ES-PANI/CFs electrode, CV measurement is also performed on bare CFs in 0.5 M $(NH_4)_2SO_4$ electrolyte, as presented in Figure 3b. It is observed that the current of this CV curve from bare CFs is extremely small and negligible compared to that from the ES-PANI/CFs in Figure 2.3a. Therefore, it can be concluded that there is negligible contribution of capacity from CFs and protons for the ES-PANI/CFs electrode for ammonium ion storage.

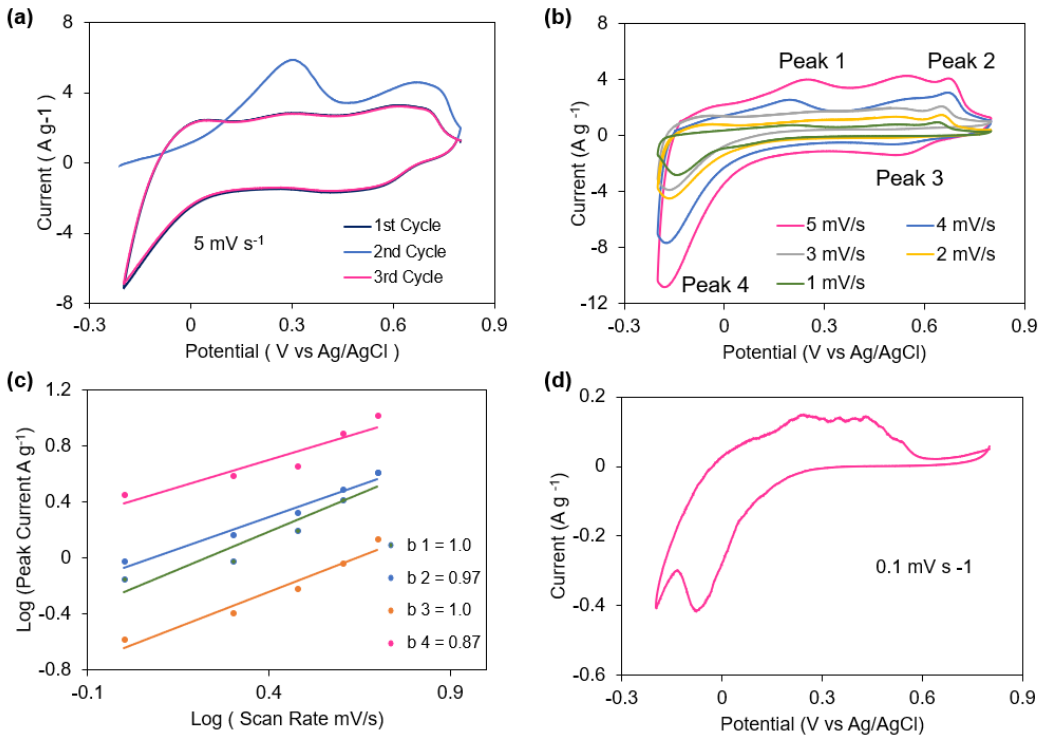

Figure 2.4. CV measurements of ES-PANI/CFs electrodes in the electrolyte of 0.5 M $(NH_4)_2SO_4$ (a) the first 5 CV curves at a scan rate of 5 mVs^{-1}, (b) CV curves at various scan rates from 1 to 5 mVs^{-1}, (c) b values for peaks 1,2,3,4 (d) CV curve at a low scan rate of 0.1 mV s^{-1}.

Figure 2.4a shows the first 3 CV curves of the ES-PANI/CFs electrode for ammonium ion storage in a potential range -0.2 V to 0.8 V at scan rate of 5 mV s^{-1}, showing two oxidation peaks at 0.244 V, 0.680 V (vs. AgCl) and two reduction peaks at 0.58 V and -0.199 V . Multiple oxidation and reduction peaks correspond to the multistep reaction process of the NH_4^+ ion intercalation and deintercalation. Furthermore, the CV profiles of the first 5 cycles clearly shows excellent repeatability which shows high reversibility and structural integrity of the ammonium ion battery system. Figure 2.4b shows the CV curves at different scan rates. There are two types of current in the CV curves as follows. One is originated from the capacitive process and the other is from the diffusion-controlled process. The currents of the CV curves follow the power law: $i_p = av^b$, where i_p is the oxidation or reduction peak current from the CV profiles and v is the scan rate. The limiting value of b can be in the range 0.5-1.0 where it will be diffusion limited redox relation with the value of b approaching 0.5 and non-diffusion controlled pseudocapacitive processes with b approaching 1.0. The power law equation is rearranged to $\mathbf{\log i = b \log v + \log a}$ to give a linear relationship of log i versus log v at the peak potentials. It can be observed from Figure 2.4c that the gradients fit linearly at about 1.0, 0.97, 1.0 and 0.87 for peak 1, 2, 3, and 4 showing the reaction kinetics being dominated by attachment limited processes also known as non-diffusion controlled pseudocapacitive processes.[59, 60] In order to understand the redox reaction in PANI a CV technique was performed at a very slow scanni9ng rate as shown in figure 2.4d. Oxidation Peaks at 0.28V and at 0.48V can be observed and reduction peak at -0.22V.

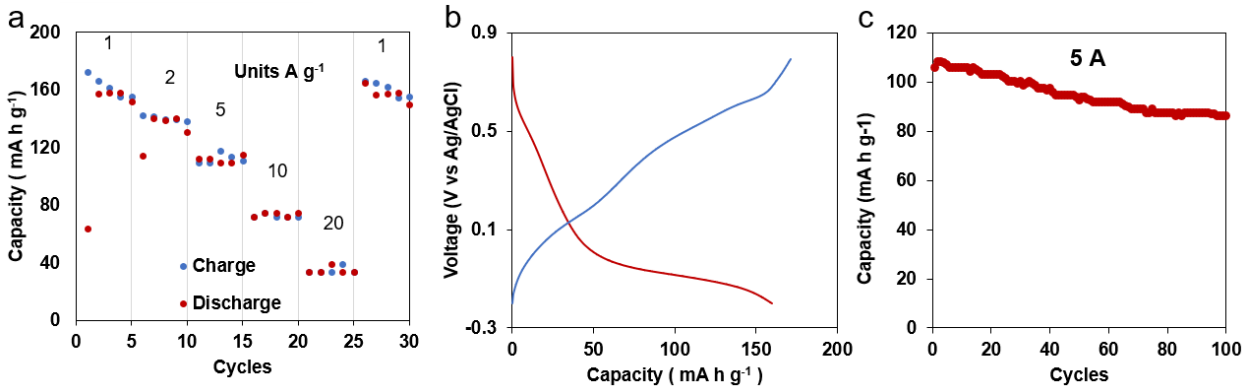

Figure 2.5. (a) Rate capability of ES-PANI/CFs at various specific currents, (b) Galvanostatic charge discharge (GCD) curves at specific current of 1 A g^{-1}, (c) cycling performance of ES-PANI/CFs electrode in at specific current 5 A g^{-1} in 0.5M $(NH_4)_2SO_4$.

Additionally, the rate performances of the ES-PANI/CFs are displayed in Figure 2.5a. The ES-PANI/CFs electrode shows excellent rate capability in a voltage window of -0.2V – 0.8V when the specific current is changed from 1 A g^{-1} to 20 A g^{-1}, revealing discharge capacities of 160 , 140 , 112, 75 and 33 mA g^{-1} within the range of ± 5 mA g^{-1} at specific current of 1 , 2 , 5 , 10 and 20 A g^{-1}, respectively, which are far better than any reported NH_4^+ storage capacities and also for EB-PANI.[61] When the specific current returns to initial 1 A g^{-1} after cycling at 20 A g^{-1} the discharge capacity is restored back to 160 mA g^{-1} which shows that ES-PANI has an excellent structural integrity after fast NH_4^+ ion migration. Figure 2.5b presents GCD profile of the ES-PANI/CFs electrode cycled between -0.2 V and 0.8 V at a specific current of 1 A g^{-1}. The electrode initially delivers a discharge capacity of 160 mAh g^{-1} and charge capacity of 171 mAh g^{-1}, corresponding to a coulombic efficiency (CE) of 93.4%. Such a high initial CE reveals reversible intercalation/deintercalation of NH_4^+ into the ES-PANI structure. Finally, upon cycling as shown in Figure 2.5c, the ES-PANI/CFs electrode exhibits an 82% capacity retention at a specific current of 5 A g^{-1} with an initial capacity of 105.5 mAh g^{-1} and 86.1 mAh g^{-1} after 100 cycles, demonstrating a durable cycling performance. The durable cyclability of ES-PANI is mainly attributed to its conjugated bonds and structural stability of ES-PANI during the NH_4^+ intercalation and deintercalation. This capacity retention is better than or comparable to those reported in literature for ammonium ion storage [62 , 2]

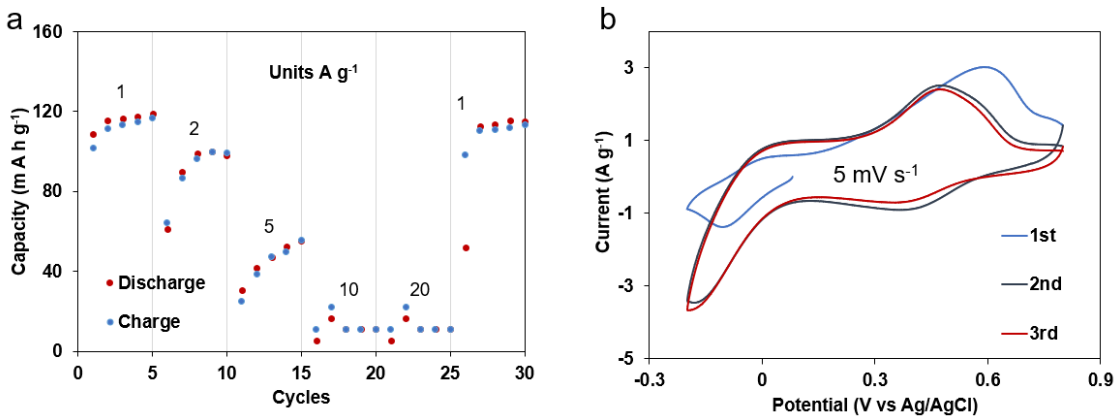

Figure 2.6. The electrochemical performance of EB-PANI/CFs for NH_4^+ ion storage: a) the first five CV curves of EB-PANI/CFs in 0.5 M $(NH_4)_2SO_4$ solution at 5 mV s^{-1}, b) rate performance of EB-PANI/CFs at various specific currents.

For comparison purpose, electrochemical performance of undoped PANI (EB-PANI) is evaluated. Figure 2.6a displays the first five CV curves of EB-PANI/CFs in the same electrolyte at a scan rate of 5 mV/s. Figure 2.6b presents the rate performance of the EB-PANI/CFs, showing its capacity is less than that from doped emeraldine salt form of PANI (ES-PANI) in Figure 2.5a. The ES-PANI/CFs electrode exhibits excellent rate capability in a voltage window of -0.2V – 0.8V revealing discharge capacities of 160, 140, 112 , 75 and 33 mA g^{-1} ± 5 mA g^{-1} at specific current of 1 , 2 , 5 A, 10 and 20 A g^{-1} respectively and EB-PANI showing discharge capacities of 116 , 97 , 55 , 11 and 8 mA g^{-1} at specific current of 1 , 2 , 5 , 10 and 20 A g^{-1} respectively. These capacities show that ES-PANI has better performance for NH_4^+ ion storage than EB-PANI. This is mainly attributed to the fact that half oxidized emeraldine base state of PANI is a semiconductor and it comprises of a sequence of one quinoid unit and two benzenoid units. EB-PANI can be non-redox doped to give a conductive ES-PANI by using a protonic acid. [63] Non-redox doping is different from redox doping in that there is no alteration on the number of electrons from the ES-PANI chains. During this non-redox doping, imine nitrogen atom will receive a proton and then transform into a polaron. This polaron will have delocalized spin and charge in the polymer backbone. Thus ES-PANI is improved with higher conductivity with larger capacity. The highly conductive ES-PANI can be changed back to semiconducting EB-PANI through treatment using a base. This doping with HCl leads to higher storage capacity of ES-PANI as compared to EB-PANI.

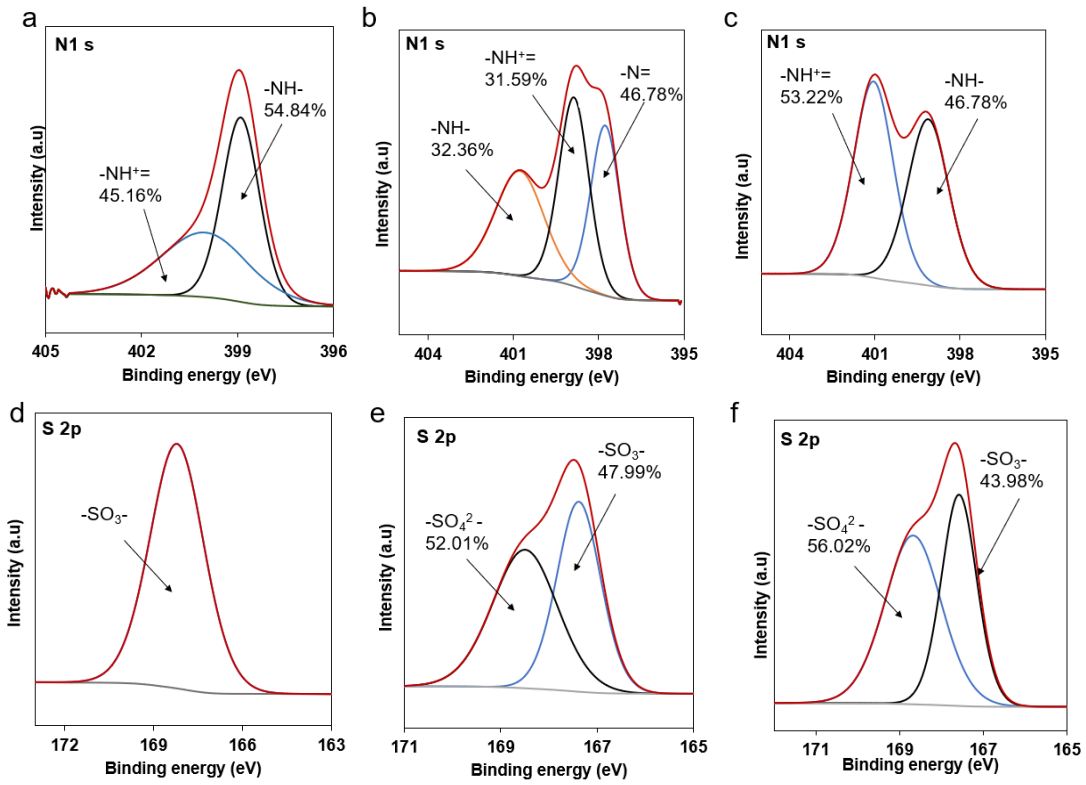

Figure 2.7. XPS spectra of nitrogen in (a) the original ES-PANI/CFs (control sample) as prepared, (b) the ES-PANI/CF sample at charged state, and (c) the ES-PANI/CF sample at discharged state. XPS of S 2p peaks from ES-PANI/CF (d) as prepared, (e) at charged state, and (f) at discharged state.

To explore the storage mechanism of NH_4^+ in ES-PANI, ex situ XPS and Raman spectroscopy characterizations are carried out. Figure 2.7a shows the XPS spectra of Nitrogen 1s (N1s) in the original ES-PANI/CF, revealing two peaks which correspond to -NH- and =N- groups. The oxidation state of nitrogen in ES-PANI polymer chain is very important because it determines the physical and chemical properties of ES-PANI. [64] The ES-PANI is in its intermediate state as shown in figure 2.7a, revealing -NH- groups with atomic weight percentage of 54.84% and $=NH^+$- groups with atomic weight percentage of 45.16%. Figure 2.7b shows the XPS from the ES-PANI/CF at the charged state. The N 1s signal from the sample at the charged state is fitted with the peak components of -NH-, $-NH^+$- and -N= with atomic weight percentages of 36.05%, 32.36% and 31.59% respectively. The above groups are consistent with the oxidized state of ES-PANI because the reduced components and oxidized components are almost equal. [65] Figure 2.7c displays XPS of the ES-PANI/CFs at the discharged state, exhibiting atomic weight percentages of $-NH^+$- (53.22%) and -NH- (46.78%). The formation of -NH- and $-NH^+$- groups show that during the discharging process there is an inter conversion of quinoid and benzenoid rings. Cl^- signal is not observed in the XPS spectra of the electrode at the charged and discharged states, suggesting Cl^- ions may dissolve in the electrolyte during electrochemical cycles and exchange with the $-SO_4^{2-}$ groups in the electrolyte.[65] This speculation is confirmed in the S2p XPS spectra of the electrodes at charged and discharged states in figure 2.7e and f revealing a new peak of $-SO_4^{2-}$ in addition to $-SO_3^-$, while S2p XPS of the original electrode in figure 2.7d only has $-SO_3^-$. After early cycling, there are three components of -NH-, $-NH^+$- and -N= in the electrode

at charged state, in which the -NH^+- is charge balanced by the $-SO_3^-$ or $-SO_4^{2-}$ groups. During the discharge process, the amount of -NH^+- increases to 53.22% and the amount -NH- increases to 46.78%. The increase in -NH- is due to the -NH^+- accepting an electron to become -NH- ; in contrast it is seen that the amount of -NH^+- also increases. Protonation of the oxidized -N= group occurs, yielding another oxidized component -NH^+-. This result is confirmed by the XPS spectra as the peak of the -N= group completely disappears in the electrode at discharged state in figure 2.7c, and the amount of -NH^+ increases whist it is charge balanced by the $-SO_3^-$ or the$-SO_4^{2-}$, which would then interact with the NH_4^+ in the electrolyte during electrochemical cycling.

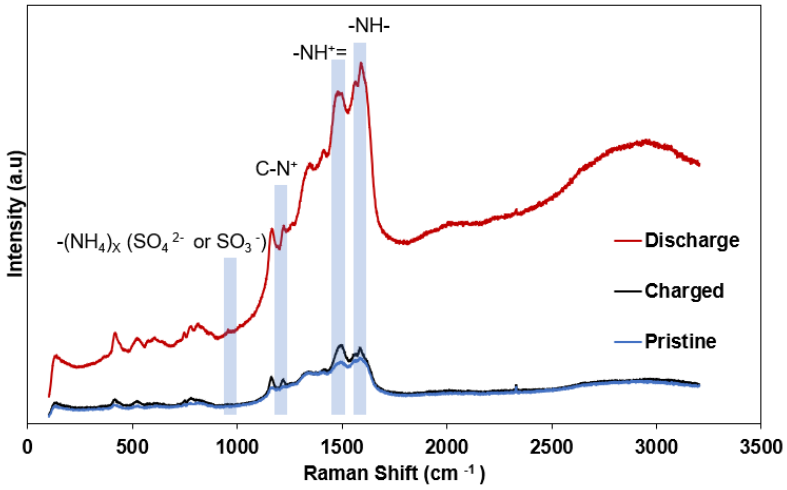

Figure 2.8. Raman spectra of the ES-PANI electrodes as prepared, and at charged and discharge states.

Figure 2.8 shows the Raman spectra of ES-PANI at charged and discharge states in comparison with the original ES-PANI. The interaction between the NH_4^+ ion and the $-SO_3^-$ or $-SO_4^{2-}$ is confirmed by the formation of a new peak at 980 cm^{-1} and at 2980 cm^{-1}, confirming the presence of $-SO_3^-$ NH_4^+ or $-SO_4^{2-}$ $(NH_4^+)_2$. As the reduction continues, more NH_4^+ gets attracted to the electrode, due to the increase in the negative charge on the electrode surface, which comes from charge balancing of the -NH^+ ion with$-SO_3^-$ or $-SO_4^{2-}$ because of the protonation of -N= group. It is important to note that the effect of resonance is more compelling than inductive in -NH- and -NH^+ groups, hence these groups have a higher electron density which makes them more electronegative.[66] Due to the electrostatic interaction, the NH_4^+ions will actively interact with the -NH- and -NH^+ groups during the discharging process. At the charged state as can be seen from the XPS spectra in figure 2.7b, the -NH- and -NH^+ groups will be converted back to -NH-, -NH^+ whose percentages decrease. This is a result of the deintercalation of NH_4^+ back into the electrolyte. From the Raman spectra in figure 2.8, it is observed that there is a general intensity increase of the nitrogen groups of particular importance of -NH- and -NH^+ peaks due to the NH_4^+ intercalation during the discharge process. At the charge state, the intensities decrease due to NH_4^+ ion being removed from the ES-PANI. The XPS spectrum in figure 2.7b shows the -N= group at the charged state, confirming that there is a transformation of quinoid and benzenoid rings during the charging and discharge process. This dual mechanism of using Cl^- as a dopant which caused a self-doping

of ES-PANI with $-SO_3^-$ or $-SO_4^{2-}$ group from the electrolyte and the changing of quinoid and benzenoid rings due to electrostatic interaction of NH_4^+ ion with high electron density in -NH- and -NH^+ groups resulted in the better electrochemical performance of the ES-PANI.

The proposed reaction pathway is shown in scheme 1 below.

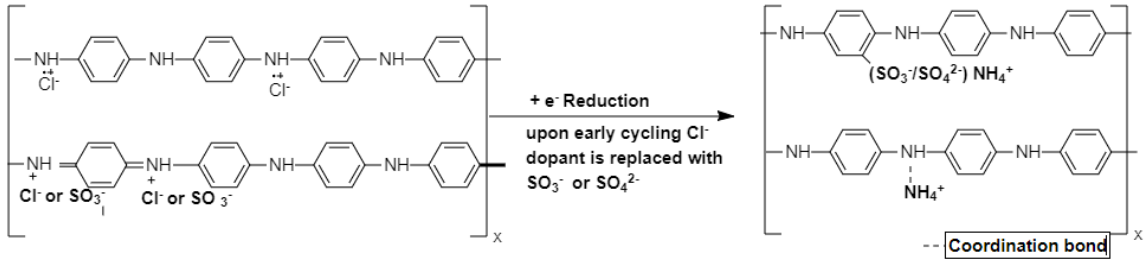

Scheme 1 The proposed reduction cycle.

The effect of post treatment method on the capacity of the ES-PANI for NH_4^+ ion storage is also investigated. The as-prepared ES-PANI deposited on the surface of the carbon felts are washed completely with either water or ethanol.

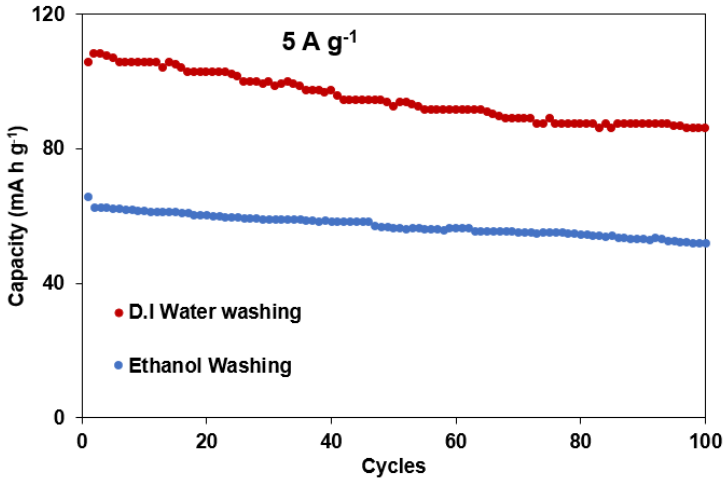

Figure 2.9. Cycling performance of the ES-PANI/CFs electrode washed with water or ethanol, respectively, when cycled in 0.5 M $(NH_4)_2SO_4$ at 5 A g^{-1}.

Figure 2.9 shows the cycling of performances the ES-PANI/CFs washed with D.I water and ethanol respectively. It can be observed that the initial capacity of the ES-PANI/CFs washed with water is 105.5 mAh g^{-1} , ± 5 mA g^{-1} and when washed with ethanol a lower capacity of 65.5 mAh g^{-1} was delivered. This result is ascribed to ethanol removing oligomers whilst dedoping the ES-PANI, which decreases the capacity of ES-PANI for NH_4^+ storage. In the ES-PANI sample, the Cl^- ions are in equilibrium with the polymer chains. Washing with Lewis bases compared to

HCl, that is, ethanol, will result in the removal of Cl^- dopants, turning the emeraldine salt into emeraldine base which has lower conductivity. Therefore, we can conclude that washing with water is more favorable for the electrochemical performance of the ES-PANI/CFs electrode.

2.4 Conclusion

In summary, high-surface-area ES-PANI with nanothorn structure is obtained on conducting carbon felts via facile in situ polymerization through chemical oxidation, for application as a storage material for NH_4^+ ion storage. At a specific current of 1 A g^{-1}, the ES-PANI/CFs delivers an initial discharge capacity of 160 mAh g^{-1} and initial charge capacity of 171 mAh g^{-1}, resulting in a coulombic efficiency of 93.4%. Of particular importance is the excellent cycling stability of the ES-PANI/CFs with capacity retention of 82% after 100 cycles at specific capacity of 5 A g^{-1}. These results together with the remarkable rate capability of the ES-PANI/CFs demonstrate ES-PANI can be a high-potential electrode material for NH_4^+ ion storage in a new aqueous rechargeable battery. The ES-PANI in our work has the optimum degree of oxidation and protonation, resulting in the formation of emeraldine salt with much increased conductivity. When PANI is doped, local charge carriers are generated. These charges can move because of the conjugated π-electron system on the polymer chains of PANI. Through the interaction with the PANI environment, the charge carriers undergo relaxation, causing the distortions of bipolarons, polarons and solitons, which can migrate intra and intermolecularly within PANI, thus giving ES-PANI high conductivity. These factors in addition to the large surface area and short diffusion paths of the nanothorn-structured ES-PANI on CFs lead to its high capacity for NH_4^+ storage. Moreover, the intercalation and deintercalation of NH_4^+ ion is shown to be highly reversible in the PANI doped with Cl^- ions, demonstrating that NH_4^+ ion is a promising charge carrier for new electrochemical energy technology and PANI as a very promising electrode material for NH_4^+ storage.

Chapter 3. A Full Flexible Ammonium Ion Battery Based on the Concentrated Hydrogel Electrolyte for Enhanced Performance

3.1 Introduction

Flexible batteries, have been attracting much attention recently, are designed to be conformal, lightweight, and can be rolled without any loss of energy. They are imperative for powering wearable electronics, smart packaging, and medical devices, etc. It has been recognized that to increase the economic viability of flexible batteries, it is imperative to develop safer and more cost-effective flexible batteries. Aqueous rechargeable batteries have shown high potential in the fast-expanding market of electrochemical energy storage devices because of their low cost and intrinsic safety. However, the use of aqueous electrolyte limits the electrochemical stability window and causes undesirable side reactions and exhaustion of water content in the electrolyte, due to the hydrogen and oxygen evolutions in the aqueous solution.

As such, "water-in-salt" electrolyte (WiSE) has been reported to alleviate this issue, by dissolving high-centration salts in water. [67,68] The WiSE can suppress side reactions such as dendrites formation, active material dissolution and replenishing of water, as pH increases with the salt concentration and thus hydrolysis is reduced. Yet such electrolytes would greatly increase the cost for future larger-scale production due to the use of a much larger amount of salts. Additionally, there remain parasitic side reactions and the potential leakage issue of liquid-state electrolytes, affecting the stability and lifetime of the battery. One approach to solve this issue is to prepare a hydrogel electrolyte with high salt concentration. Compared to the WiSE, the hydrogel electrolyte can serve as a separator with better safety/stability, and the number of salts can be significantly reduced with the polymer bonded with water to form a network. The ionic conductivity of the aqueous solution improves with the increased salt concentration but decreases with further increased salt concentration because too many salts can expand the volume of the solution. Therefore, the salt concentration can be optimized to achieve maximum ionic conductivity.

Layered vanadium-based materials have been utilized as cathode materials in zinc ion batteries (ZIBs) due to their large interlayer spacings, the abundance, high capacity that can tolerate high number of electron transfer and structural stability during cycling.[69] Thus, they might be good candidates as electrode materials to accommodate large NH_4^+ ions. It has been reported that ions can be inserted in the layered structure of the vanadium-based materials in the form of cations and lattice water, leading to improved stability during the ingress/egress of cations particularly Zn^{2+} ions.[70,71,72,73] Met^{2}al cations, such as $Na^{+,}$ [74] K^+,[75] Zn^{2+}, [69] or Mg^{2+},[76] can be

---

This chapter previously appeared as : Farai Kuchena, Shelton, and Ying Wang. "A full flexible NH_4^+ ion battery based on the concentrated hydrogel electrolyte for enhanced performance." *Chemistry–A European Journal* 27, no. 62 (2021): 15450-15459. Copyright 2021 Wiley Publishing company: https://chemistry-europe.onlinelibrary.wiley.com/doi/full/10.1002/chem.202102442

employed as pillars in layered vanadium-based materials, to enhance the capacity retention after long cycling. But these metal ions have high atomic masses and do not contribute to the capacity, particularly in ZIBs, thereby limiting the capacity of the cathode materials. On the other hand, lighter NH_4^+ ions along with crystal lattice water can exist as pillars in the layered structure of ammonium metavanadates, resulting in enhanced capacity for NH_4^+ ion storage. The strong hydrogen bonds formed between NH_4^+ pillars and the vanadium oxide layer along with lattice improve the structural stability by mitigating structural changes during the NH_4^+ (de)intercalation, leading to better cycling performance. For example, ammonium vanadium bronzes have been employed in different rechargeable battery systems such as Li^+, Na^+, or Mg^{2+} battery systems consisting of organic electrolytes.[77,78,79,80, 81] An earlier publication from our group demonstrated PANI is a good host for NH_4^+ ion, with a capacity of 167 mAh g^{-1} at a specific current of 1 A g^{-1}.10 The PANI electrode showed good cycling ability because of its good ionic conductivity and reverse convertibility between redox states during cycling.[10] Additionally, Hui lai et al. assembled a full AIB with PANI nanorods grown on carbon fibers as anode and $NH_4V_4O_{10}$ as cathode in a 1M $(NH_4)_2SO_4$ aqueous electrolyte. A capacity of 167 mA g^{-1} at a specific current of 0.1 A g^{-1} was reported along with stable performance under different mechanical deformation.[82]

Herein, we fabricate a full flexible ammonium ion battery consisting of a concentrated hydrogel electrolyte sandwiched between the $NH_4V_3O_8.2.9H_2O$ nanobelts cathode and the PANI anode, in addition to a full battery composed of the same electrodes but liquid electrolyte for comparison purpose. The hydrogel electrolyte is synthesized via mixing xanthan gum and ammonium sulfate solution. A variety set of polymers with hydrophilic chains can be used to obtain hydrogels.[83] Among them, xanthan gum is an excellent choice, as it is natural and biodegradable, with hydroxyl groups that can attract a great amount of water molecules and long polymer chains that can strengthen the interaction with water molecules. Additionally, xanthan gum has a high tolerance of salts because it is a complex exopolysaccharide with α, β-1,4-linked glucan backbone along with trisaccharide side chains attaching on the alternating D-glucosyl residues.[84, 85] The salt concentration in the hydrogel electrolyte is varied and optimized to maximize the battery performance. Moreover, the full flexible battery is examined for electrochemical performance while undergoing mechanical deformation.

A flexible full NH_4^+ ion battery (AIB) composed of a concentrated hydrogel electrolyte sandwiched between $NH_4V_3O_8{\cdot}2.9H_2O$ nanobelts cathode and polyaniline (PANI) anode, for enhanced performance is presented. The hydrogel electrolyte is simply synthesized by using ammonium sulfate, xanthan gum and water. As a reference, the AIB based on the liquid aqueous electrolyte is prepared first, which exhibits a capacity of 121 mAh g^{-1} and a capacity retention of 95% after 400 cycles at a specific current of 0.1 A g^{-1}. On the other hand, the simple synthesis of the hydrogel electrolyte allows us to facilely tune and optimize the salt contents in the electrolyte, to maximize the ionic conductivity, transport kinetics, mechanical characteristics, and consequently the battery performance. It is found that the flexible battery based on the hydrogel electrolyte prepared from 3 M ammonium sulfate solution shows the best electrochemical performance, i.e., a capacity of 60 mAh g^{-1} while maintaining a capacity retention of 88% after 250 cycles at a specific current of 0.1 A g^{-1}. Moreover, the flexible AIB retains excellent electrochemical performance when bent at different angles, demonstrating remarkable mechanical

strength and flexibility. Therefore, this study sheds new light on the utilization of concentrated hydrogel electrolyte in the AIB chemistry, for future developments of new electrochemical energy storage technology with high safety and low cost.

3.2 Experimental Section

3.2.1 Materials Synthesis

A hydrothermal method was used to synthesize $NH_4V_3O_8.2.9H_2O$. In a typical synthesis, a solution of 1g of V_2O_5 (Sigma -Aldrich 99.5% purity) and 5 ml ammonium hydroxide (VWR 18-30%) was made, followed by the addition of 40mL of 0.1M oxalic acid (VWR ≥99.0%). The mixture was then magnetically stirred for 30 mins at 20°C. The pH of the solution was adjusted to 3 via dropwise addition of HCl (Alfa-Aesar 36%). The solution was then put into a 10 mL Teflon-lined autoclave and heated to 190°C for 5 h. The precipitates were placed at room temperature and allowed to cool down naturally. The precipitates were washed three times with ethanol, then placed in an oven for drying at 60°C for 12 hrs.

To synthesize PANI, a solution that contained 0.365 mL aniline (Acros Organics, 99+% purity) and 15 mL of 1 M HCl (Alfa-Aesar 36% purity) was placed under magnetic stirring. To maintain a low temperature in the range of 0−5°C the solution was placed in an ice bath and continuously stirred for 1 h. After 1hr of continuous stirring, a solution containing 5 mL of 1 M HCl (Alfa-Aesar 36%) with dissolved 0.228 g $(NH_4)_2S_2O_8$(APS Sigma -Aldrich 99%) was added dropwise whilst under continuous stirring in the ice bath. The color changed to dark green after a few minutes showing polymerization has occurred. After 1 h under continuous stirring, the precipitates were collected and washed with deionized water three times, and then put in an oven for drying at 60°C for 12 h. The obtained precipitates were then used to make the anode film.

The hydrogel electrolyte was prepared by dissolving 1 g xanthan gum powder in 2 mL DI water and mixed homogeneously at room temperature overnight. Afterwards, 1 M (or 2M or 3 M) solution of $(NH_4)_2SO_4$ (VWR Chemicals ≥99.0%) prepared from 3 ml deionized water was added into the above mixture, respectively, followed by stirring for 2 days to obtain the 1 M, 2 M, and 3 M QSS electrolyte respectively.

3.2.2 Materials Characterizations

The X-ray diffraction was done using a Rigaku MiniFlex X-ray diffractometer with Cu Kα radiation (λ = 1.5405 Å) scanning rate of 2° min^{-1}. The Scanning Electron Microscopy images were obtained using the FEI Quanta 3D FEG field emission scanning electron microscopy (FESEM). X-ray photoelectron spectroscopy (XPS) measurements were carried out using an AXIS165 spectrometer. The thermogravimetry (TGA) data were collected using an SII STA7300 analyzer under nitrogen.

3.2.3 Electrochemical Characterizations

The electrode (PANI anode or $NH_4V_3O_8.2.9H_2O$ cathode) was prepared in a ratio of 6:3:1 for active material (PANI or $NH_4V_3O_8.2.9H_2O$) : conductive carbon: polytetrafluoroethylene (PTFE) and rolled into a thin film. The full aqueous battery was assembled with the cathode and the anode in 1 M $(NH_4)_2SO_4$ solution in a coin cell. The full quasi-solid state AIB was prepared with the hydrogel electrolyte sandwiched between the cathode and the anode. The mass ratio of anode to cathode was set at 1:2, to make the cathode in excess to account for the difference in capacities of the two, according to the capacity matching principle. The capacity was calculated based on the mass of both anode and cathode. To lighten up the LED bulb, four AIBs were connected in series. The galvanostatic charge-discharge tests were performed within a voltage range of 0 – 1 V on the 8 channel battery analyzers (MTI Cooperation). The cyclic voltammetry and electronic impedance measurements were carried out using an electrochemical workstation (CHI 6504C) with a frequency range from 100 kHz to 0.01Hz.

3.3 Results and Discussion.

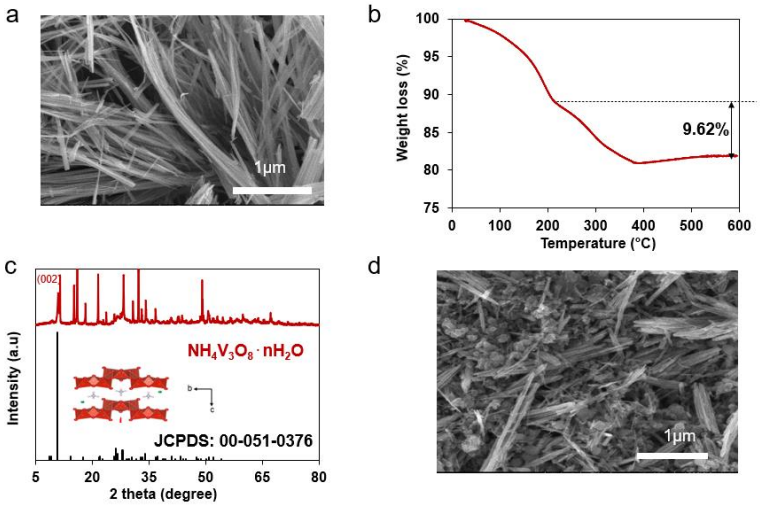

Figure 3.1. a) SEM image of ammonium vanadate nanobelts, b) XRD pattern of $NH_4V_3O_8$. nH_2O sample, c) thermogravimetric analysis result of $NH_4V_3O_8$. nH_2O sample, and d) SEM image of $NH_4V_3O_8.nH_2O$ cathode film

Figure 3.1a presents the SEM image of the hydrated ammonium vandate, revealing a porous urchin-like archtecture composed of bunches of nanobelts. X-ray diffraction (XRD) is then performed on the ammonium vandate powders to determine its composition and structure. The XRD pattern in Figure A1b can be indexed to JCPDS no. 00-051-0376, corresponding to $(NH_4)_2V_6O_{16}{\cdot}mH_2O$ or $NH_4V_3O_8{\cdot}nH_2O$. According to an article about $NH_4V_3O_8$ prepared by the hydrothermal method, the most intense peak in its XRD pattern would become much weaker as

the pH becomes closer to 2.[86, 87] Hence, the most intense peak in our XRD pattern in Figure 3.1b might have a doublet and decreased intensity in comparison with other peaks, because the pH in the solution during the synthesis is 3. The major challenge to develop AIBs has been that NH_4^+ ions have large ionic size. It is calculated that the lattice spacing of the (002) facet of the $NH_4V_3O_8{\cdot}nH_2O$ is 8.8 Å, which is similar to the interlayer spacings reported for $Na_2V_6O_{16}{\cdot}3H_2O$,88 $Ca_{0.25}V_2O_5{\cdot}nH_2O$,[89] and zinc pyrovanadate.[90] The $NH_4V_3O_8$ structure is made up of VO_6 octahedra and VO_5 square pyramids as well as water, with NH_4^+ cations acting as pillars to support the VO_x layers, which stabilizes the layered crystal structure during the NH_4^+ ions (de)intercalation. To examine the water content in the ammonium vanadate, Figure 3.1c displays the thermogravimetric analysis profile of the ammonium vanadate sample under nitrogen in a temperature range of 25 - 600°C. Based on the water content loss in this plot, the crystalline water content in the sample is determined to be 2.9 per $NH_4V_3O_8$ unit. Therefore, the chemistry formulae of the cathode material is $NH_4V_3O_8{\cdot}2.9H_2O$. The vandate nanobelts are then mixed with binder and carbon black, to make a cathode film and the same structure can be seen after it was made into a film as shown on Figure 3.1d.

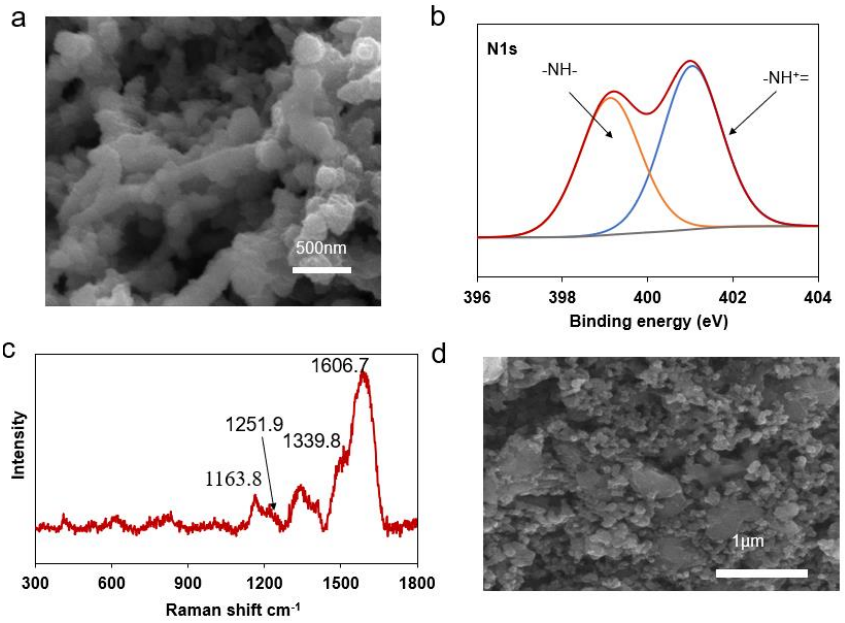

Figure 3.2. a) SEM image of polyaniline powders, b) Raman spectra of PANI powders, c) N1s XPS spectra of PANI powders, d) SEM image of the polyaniline anode film.

Figure 3.2a shows the SEM images of the PANI powders. The PANI sample reveals a nano thorn structure, which is favorable for excellent electrochemical performances as it provides short diffusion paths and large surface area for electrochemical reaction sites. Figure 3.2b presents the XPS N1s spectrum of the PANI sample. The oxidation state determines the storage mechanism on NH_4^+ ions in the PANI electrode. The two N1s groups related to the two peaks in the spectrum represent the -NH^+= and -NH- with a percentage of 50.45% and 49.55% respectively. Such an almost equal amount of imine to amine groups shows that the PANI sample is in its half oxidation state, which is characteristic of the conductive emeraldine salt PANI state. The Raman spectra of the PANI in Figure 3.2c reveals a peak at 1163.8 cm^{-1} corresponding to the C-H group bending

vibration of the quinoid ring, a peak at 1251.9 cm^{-1} of the same group but representing the benzenoid ring, a peak at 1606.7 cm^{-1} for the C=C quinoid ring, and a peak at 1339.8 cm^{-1} related to C-N^{+}. Figure 3.2d presents the SEM of the anode film composed of PANI, polymer binder and carbon black, exhibiting a highly porous structure. To examine the electrochemical performance of the full AIB based on the PANI anode and the $NH_4V_3O_8{\cdot}2.9H_2O$ cathode, the 1 M $(NH_4)_2SO_4$ aqeous electrolyte is employed first. The electrochemical performance of PANI//$NH_4V_3O_8{\cdot}2.9H_2O$ cell is evaluated in a coin cell with an anode/cathode mass ratio 1:2. This ratio is adopted based on the capacity match principle of the materials to fully utilize their capacity, so as to achieve a maximum capacity based on the combined mass of cathode and anode.

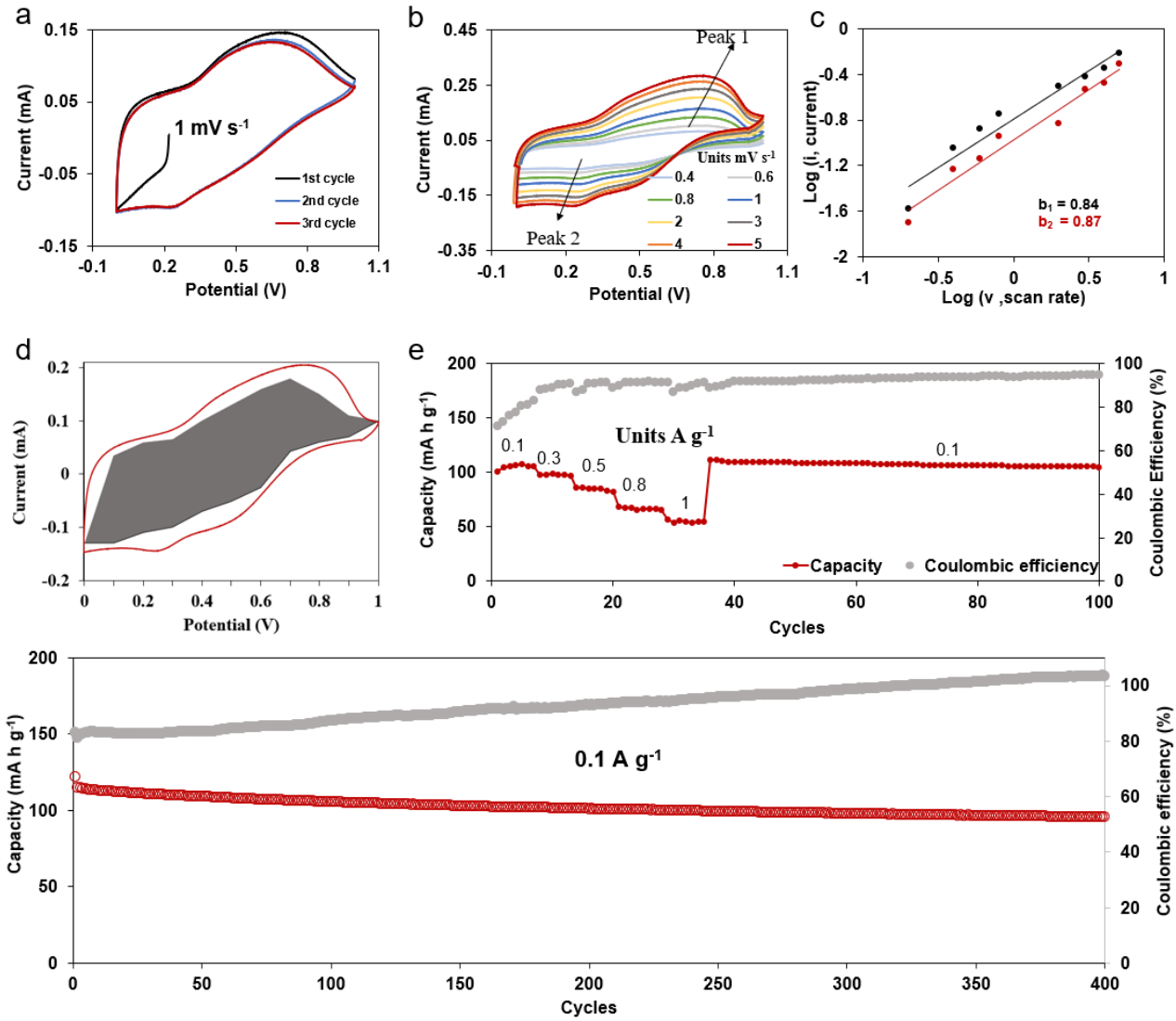

Figure 3.3. Electrochemical performances of the battery composed of PANI//$NH_4V_3O_8.2.9H_2O$ in 1M aqueous $(NH_4)_2SO_4$ electrolyte. (a) The first 3 cycles of the cyclic voltammogram (CV) curve at 1 mVs^{-1}, (b) a series of CV profiles at various scan rates, (c) Log (i) vs Log (v) at cathodic and anodic peaks, (d) the CV showing capacitive contribution at 1mV s^{-1}, (e) the rate capability at different specific currents with coulombic efficiency, (f) cycling performance and coulombic efficiency at specific current of 0.1 A g^{-1}.

Figure 3.3a presents the first three cyclic voltammogram (CV) cycles of this battery. There is a cathodic peak at 0.252 V, which is different from the anodic peak at 0.683 V. The overlapping of the first three CV curves shows good reversibility and good structural integrity of the AIB. Figure 3.3b illustrates the CV curves of the battery at various scanning rates, showing a slight shift in the peak potentials as the sacn rate is increased. By applying the power law $i = av^b$, if ploted on the log scale in the form of $\log I = b\log v + \log a$, where I is the peak current , v is the scan rate, a linear relationship is displayed in figure 3.3c. The b value is the gradient of the plot, if confirmed in the range 0.5 – 1. If the value approaches 0.5, it means that the electrochemical reaction mechansim is diffusion controlled; if the value of b aproaches 1.0, it is a capacitive process. The b value is 0.84 and 0.87 for the peak 1 and 2 respectively, which confirms that the electrochemical reactions in the battery above are dominated by the capacitive controlled processes. Applying the Trassati and Dunn differentiation method using the equation of total current $i(v) = k_1v + k_2v^{1/2}$, we are able to calculate the current contribution from both the capacitive process and diffusion controlled process. Figure 3.3d shows that the capacitive contribution to total current which is aproximately 74%. The aqeous AIB is tested at different specific currents to test its rate perfomance. As summarized in Figure 3.3e, the aqeous AIB delivers a reversible capacity of 110, 98, 78, 64, and 58 mA g^{-1} ± 5 mA g^{-1} at a specific curent of 0.1, 0.3, 0.5, 0.8 and 1 A g^{-1}, respectively, demonstrating excellent rate capability with approximately 38% capacity loss when specific current is increases from 0.1 A g^{-1} to 0.8 A g^{-1}. The aqueous AIB also exhibits excellent cycling perfomance as shown in figure 3.3f, showing a high capacity retention of 95% after 400 cycles.

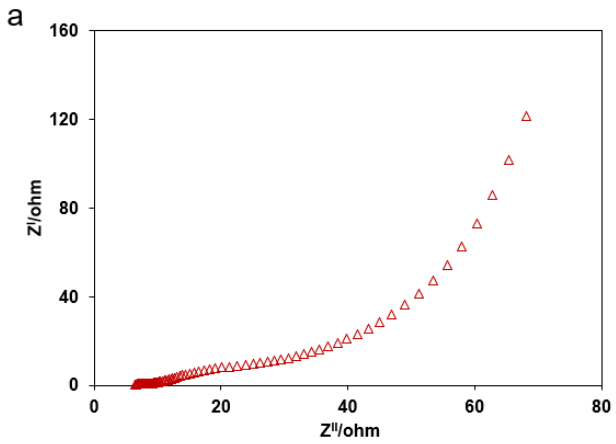

Figure 3.4. Electronic Impedance spectrum of the full ammonium ion battery with 1 M ammonium sulfate aqueous solution as the electrolyte.

The Electrochemical Impedance Spectroscopy (EIS) was also carried out in order to understand the interficial charge transfer process in the AIB above, and the EIS spectrum is displayed in figure 3.4 , revealing a charge transfer resistance of 25 Ω which shows fast reaction kinetics in this electrochemical system.

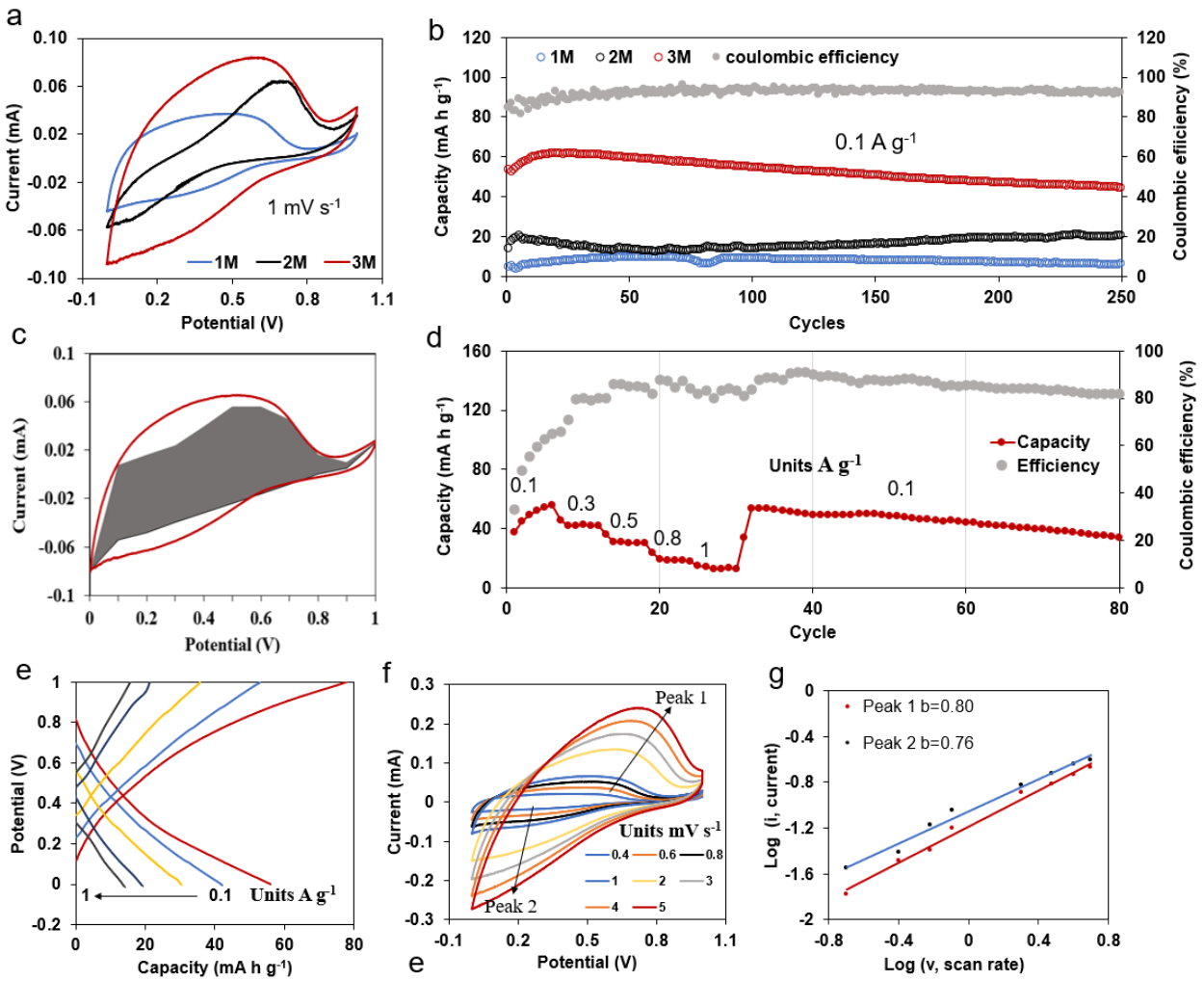

Figure 3.5. (a) CV profiles and (b) long term cycling performances at a specific current of 0.1 A g^{-1}, from the full QSS AIBs composed of PANI//$NH_4V_3O_8.2.9H_2O$ electrodes and the hydrogel electrolytes prepared from 1 M, 2 M, and 3 M ammonium sulfate solutions respectively and coulombic efficiency of the battery with 3 M electrolyte. Electrochemical performances of the full QSS AIB composed of PANI//$NH_4V_3O_8.2.9H_2O$ electrodes and the hydrogel electrolyte prepared from 3 M ammonium sulfate solutions: (c) CV showing capacitive contribution at 0.8 mV s^{-1} scan rate, (d) rate capability, (e) charge and discharge profiles at different specific currents, (f) CV profiles at different scanning rates, (g) Log i (peak current) vs Log v (scan rate) at different oxidation/reduction states based on the CV data in (g).

Encouraged by the results above, we explore the full AIB consisting of the same electrodes but a hydrogel electrolyte with varied salt concentration. Three different hydrogel electrolytes based on xanthan gum are prepared using 1, 2 and 3 M $(NH_4)_2SO_4$ aqueous solution, respectively. The electrochemical performances of the QSS AIB with the hydrogel electrolyte of different salt concentration are evaluated and presented in figure 3.5. Figure 3.5a presents the CV curves of the full batteries based on the hydrogel electrolyte prepared from 1 M, 2 M, 3 M ammonium sulfate respectively. The CV curve of the battery with the 3 M electrolyte has the largest area, indicating

it may have the best electrochemical performance among the three. It should be noted that the n M hydrogel electrolyte refers to the hydrogel being prepared from n M aqueous salt solution, not that the concentration of salts in the hydrogel form is n M. Figure 3.5b compares the cycling perfomances of the three batteries based on 1, 2 and 3 M hydrogel electrolytes at a specfic current of 0.1 A g^{-1}. It is observed that the battery consisting of the 3 M gel electrolyte delivers the highest intial capacity of 55 mA g^{-1} among the three and retains 88% capacity after 250 cycles, while battery with the 2 M QSS electrolyte has an initial capacity of 23 mAh g^{-1} and a capacity retention of 98% after 250 cycles, and the battery with the 1 M QSS electrolytes shows a very low capacity of 5 mAh g^{-1} with 99% capacity retention after 250 cycles. These results are attributed to the increased ionic conductivity, reduced side reactions, and suppressed active material dissolution in the hydrogel elecrolyte with higher salt concentration. We also explored the possibility of preparing hydrogel electrolyte with higher salt concentration. But when we try to mix the gum/water suspension with 4 M ammonium sulfate solution, precipitates appear and no homogeneous hydrogel can be obtained, possibly due to the larger salt amount and less water. This phenomenon is observed for the electrolyte containing salt concentration ranging from moderate to high with asymmetric/irregular ions and its ion associations may result in large, branched aggregates when added to gum/water suspension.[91] Therefore, we can conclude the optimized concentration of ammonium sulfate that can be used to prepare hydrogel electrolyte for the best performance in the full QSS AIB is 3 M.

Figure 3.5c presents the capacitive contribution to the total CV current for the 3M QSS electrolyte. At a scan rate of 0.8 mV s^{-1}, aproximately 79% of the total current is from the capacitive contribution, which accounts for the excellent rate performance of this AIB. The full AIBs reported in literature mostly show poor cycling and rate perfomaces, due to irreversible structural change during the de/intecalation of NH_4^+ ions and intensive polarisation of NH_4^+ ions accompanied by slaggish redox kinetics.[92] However, the 3M QSS AIB in this work exhibits good rate capability at specific currents in a range of 0.1 – 1 A g^{-1} in a potential window of 0 – 1 V, as shown in figure 3.5d and e. The 3M QSS AIB exibits reversible capacities of 60, 48, 38, 24, and 18 mA g^{-1} ± 5 mA g^{-1} at a specific current of 0.1, 0.3, 0.5, 0.8 and 1 A g^{-1} respectively. To the best of our knowledge, this result is the best rate perfomance for a full QSS AIB so far. Notably is the fact that there is an aproximately 37% capacity decay as the specific current increases from 0.1A g^{-1} to 0.5 A g^{-1}. At a specfic current of 1 A g^{-1}, it has a corresponding charge-discharge time of approximately 40 s. These results demonstrate fast kinetics and good rate perfomance of the 3M QSS AIBs, even though NH_4^+ has large ionic radius and traditional QSS electrolyte generally has slower ionic transport compared to a liquid aqeous electrolyte. As the specific current switches to 0.1 A g^{-1}, the capacity becomes 55 mAh g^{-1} which is close to the intial capacity, suggesting high structural integrity of the electrodes after accomodating large NH_4^+ ions. It can be seen that the initial coulombic efficiency of the battery at a specific current of 0.1 A g^{-1} is approximately 60% and impoves sugnificantly as the cycling continues, and increases to 80% at higher specific current due to the activation of the ammonium metavanadate. The same phenominon has also been reported in recent publications about NH_4^+ ion batteries. To better understand the kinetics in the full battery, figure 3.5f shows the CV curves of the battery based on the 3M hydrogel electrolyte at different scan rates ranging from 0.4 to 5 mV s^{-1}. As scanning rate is increased, the CV profiles retain their shapes, suggesting good structural integrity and continous reversible de/intercaltion of NH_4^+ ion. Similar to what is discussed above regarding the power law $i = av^b$ for figure 3.2f, a linear relationship is given in figure 3.5g. The b value here is 0.78 and 0.80 for peak 1 and 2

respectively, confirming that the electriochemical reactions in the full battery with the hydrogel electrolyte are dominated by capacitive and diffusion controlled processes.

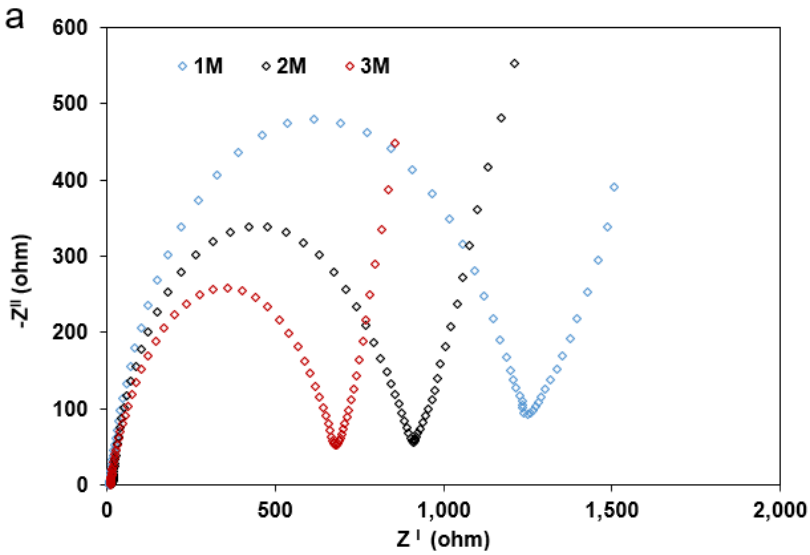

Figure 3.6. Electronic Impedance spectra of the full QSS AIBs based on the hydrogel electrolytes prepared from 1 M, 2 M, and 3 M ammonium sulfate solution, respectively.

Similarly, the EIS is performed to understand the interficial charge transfer processes in the AIBs based on the 1,2 and 3M QSS electrolytes, as shown in Figure 3.6. It is found that batteries based on the 1,2 and 3M QSS electrolytes have charge transfer resistances of 1249, 906, and 680 Ω respectively, which can explain the best electrochemical perfomance from the battery consisting of the 3 M QSS electrolyte among the three. These results confirm that the hydrogel with higher salt concentration promotes faster transport kinetics in the electrolyte. The same effect is observed in zinc ion batteries composed of concentrated hydrogel electrolytes made from Xantham gum for operations at sub-zero temperatures

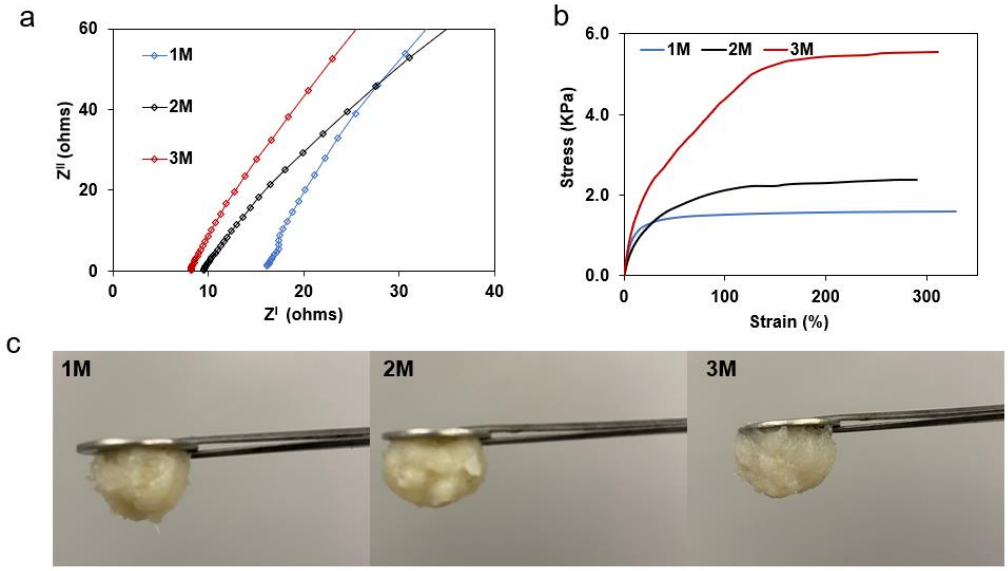

Figure 3.7. (a) The EIS profiles and (b) the stress vs. strain curves of the hydrogel electrolytes prepared from 1 M, 2 M, and 3 M ammonium sulfate solutions, respectively, and (c) photos showing adhesion of the three electrolytes to the stainless-steel substrates.

The EIS measurement is also conducted on the QSS electrolyte sandwiched between two titanium plates for examining its ionic conductivity. The ionic conductivity is given by $\sigma = d/RA$, where d is the thickness R is the resistivity and A is the area. From the EIS spectra of the three electrolytes in figure 3.7a, it can be calculated that the ionic conductivities of the 1, 2 and 3M gel electrolytes are 1.9×10^{-3} S cm^{-1} , 3.7×10^{-3} S cm^{-1}, 6.1×10^{-3} S cm^{-1} , respectively. The ionic conductivity of the electrolyte increases when its salt concentration is increased, and the 3M electrolyte has the highest ionic conductivity. Additionally, to investigate the mechanical characteristics of the electrolytes, tensile tests are performed on them, and their stress-strain curves are presented in figure 3.7b. It is found that the tensile strengths of the 1, 2 and 3M gel electrolyte are 1.52, 2.12 and 4.36 KPa respectively. It can be observed that the tensile strength of the hydrogel electrolyte increases as the salt concentration increases due to a more rigid structure of the electrolyte containing more salts and less water. Therefore, the 3 M hydrogel electrolyte has the highest tensile strength among the three, which is beneficial to the flexible battery as it can withstand a considerable load without mechanical failure to ensure stable electrochemical performance during cycling. The adhesion between the electrolyte and electrode is also crucial to the performance of the flexible battery. Thus adhesion tests are carried out for all the three electrolytes, as shown in figure 3.7c, indicating all the electrolytes attach very well to steel substrates showing good robustness.

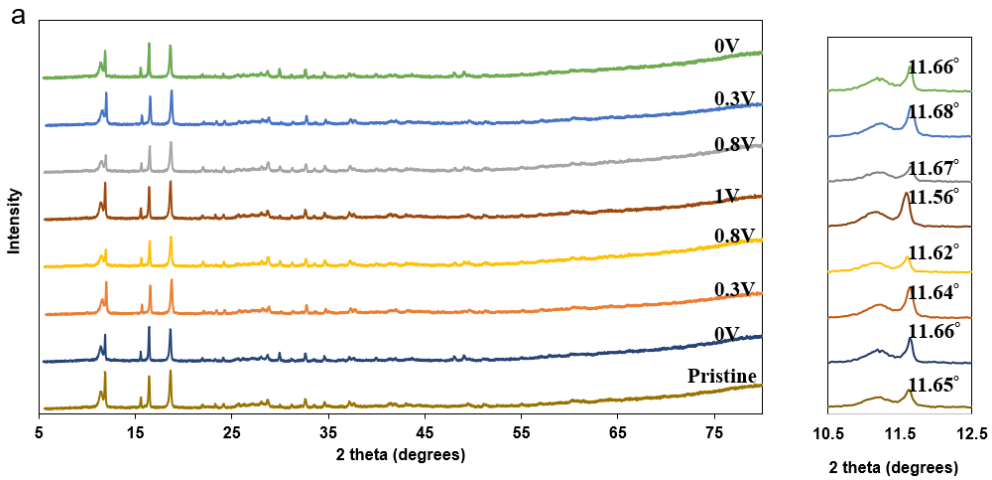

Figure 3.8. Ex situ XRD patterns of the $NH_4V_3O_8.2.9H_2O$ cathode at different discharged/charged states.

X-ray diffraction is carried out to determine the structural changes in the $NH_4V_3O_8{\cdot}2.9H_2O$ cathode during the charge and discharge process. Figure 3.8 displays the XRD patterns ·of the cathode at different discharge or charge states. There is a peak shift from 11.56° to 11.66°, when the state of the battery is changed from being fully charged to fully discharged, correspond·to a slight change in the interlayer spacing from 7.68 Å to 7.62 Å. This slight structural change of $NH_4V_3O_8{\cdot}2.9H_2O$ during the intercalation and deintercalation of NH_4^+ ion shows promising structural stability. This shows excellent structural stability of the $NH_4V_3O_8{\cdot}2.9H_2O$. Wang et. al [93] have observed the same phenomenon for the $(NH_4)_2V_6O_{16}$ electrode in an aqueous ZIB stable cyclability. During the discharge process, NH_4^+ ions are intercalated into the layered structure of $NH_4V_3O_8{\cdot}2.9H_2O$, forming N-H----O hydrogen bonds between NH_4^+ ions and O in the V-O layers; and during the charge, the N-H----O hydrogen bonds are broken. The slight contraction in the lattice distance is observed due to the screening effect of the interlayer repulsion as the amount of NH_4^+ ions increase. The decrease in the interlayer spacing from 7.68Å to 7.62Å is ascribed to the expulsion of crystalline water in the interlayer structure, whilst the increase in the amount of NH_4^+ ions increase the screening effect, and thus further pins the layers together. The same effect has been observed in the layered $Zn_{0.25}V_2O_5{\cdot}nH_2O$ electrode in ZIBs too.[94] This effect is further enhanced by the electrostatic attraction between the NH_4^+ ions and the negatively charged V_3O_8. The shift is also observed for other peaks, attributed to the NH_4^+vacancy ordering as the amount of NH_4^+ ions increase.

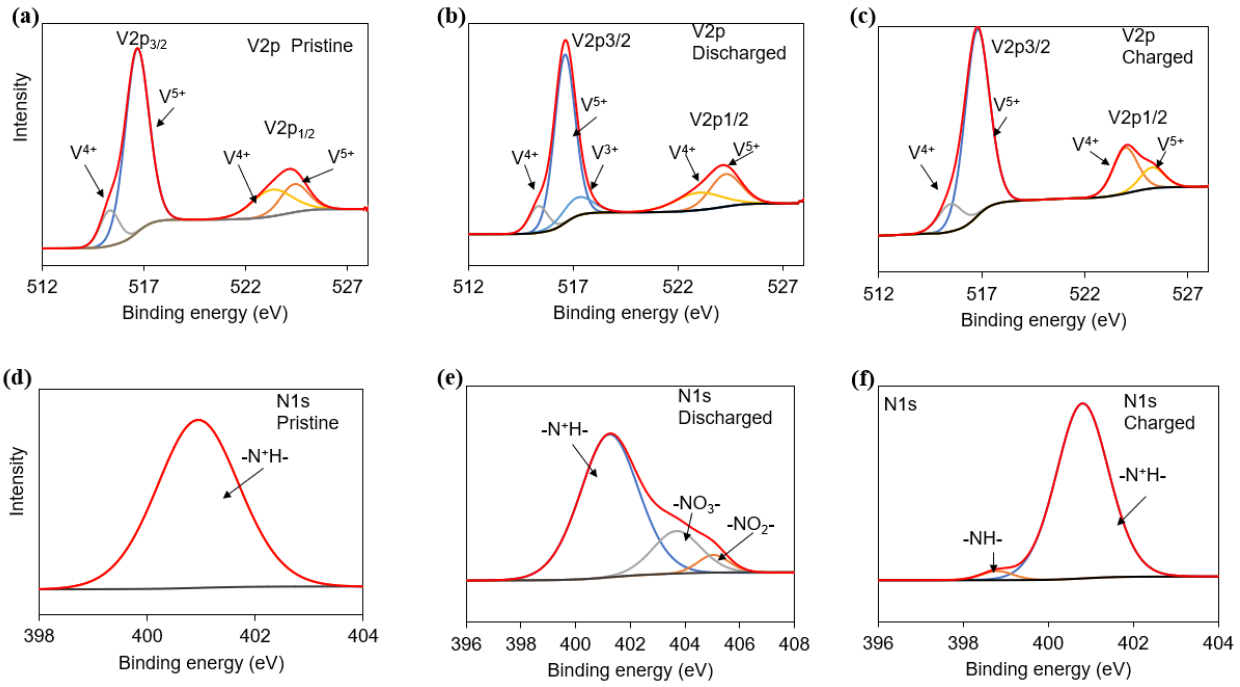

Figure 3.9. Ex situ XPS spectra for V2p (a-c) and N1s (d-f) at pristine, fully discharged and fully charged.

To further explore the change of the ammonium vanadate cathode during cycling, XPS characterization is perform to study the valence state of V and N in the pristine, charged and discharged state of the cathode as shown in figure 3.9. In the pristine state of the cathode as revealed in figure 3.9a, V has peaks located at 515.45 eV and 523.95 eV ascribed to V $2p_{3/2}$/V $2p_{1/2}$ corresponding to the spin orbit doublet for V(IV), and has peaks at 516.75 eV and 525.25 eV representing V(V) due to the impurity of the precursor V_2O_5.[95,96] At the discharged state of the cathode in figure 3.9b, the V$2p_{3/2}$ peaks at 517.18 eV, 516.60 eV and 515.35 eV are attributed to V^{5+}, V^{4+} and V^{3+} respectively, and the V$p_{1/2}$ peaks at 524.26eV and 522.96eV correspond to V^{5+} and V^{4+}, showing the reduction of vanadium due to the NH_4^+ intercalation.

Furthermore, the peaks of V^{4+}/V^{5+} shift slightly to a higher binding energy of 517.18 eV, 516.60 eV and 515.35 eV ascribed to V^{5+}, V^{4+} and V^3 respectively, owing to the NH_4^+ ion intercalation and the bonding rearrangements at the V^{4+}/V^{5+} sites in the layered structure of the ammonium vanadate cathode. These have also been observed for the zinc ion insertion in metavanadates, but the mechanism remains unclear. [97, 98] In the charged state of the cathode at 1 V as shown in figure 3.9c, most of the V^{4+}/V^{3+} will be oxidized to V^{5+}, indicating high reversible de/intercalation of NH_4^+ ions in the $NH_4V_3O_8{\cdot}2.9H_2O$ lattice. The N1s spectra in figure 3.5d displays a peak at 400.95 eV ascribed to N^+H-(-NH_4^+) that can be seen in the charged and discharged state, showing the existence of NH_4^+ in the ammonium vanadate cathode. At the discharged state, there are new peaks at positions 405.04 eV and 403.69 eV corresponding to the formation of -NO_2- and -NO_3- in Figure 3.9e. The appearance of the new peaks is resulted from the bonding between the NH_4^+ ions with the oxygen atoms from the crystalline water and the V-O layers. The formation of this special bond to yield -NO_x- is due to the stress and position relaxation

and site orientation, resulted from the increased amount of NH_4^+ ions during the discharging. At fully charged the cathode has the N1s spectrum in figure 3.9f reveals the peaks shift back to the pristine positions corresponding to -NH-(-NH_3) and -N^+H-(-NH_4^+), demonstrating highly reversible NH_4^+ ions intercalation in the ammonium vanadate layers.

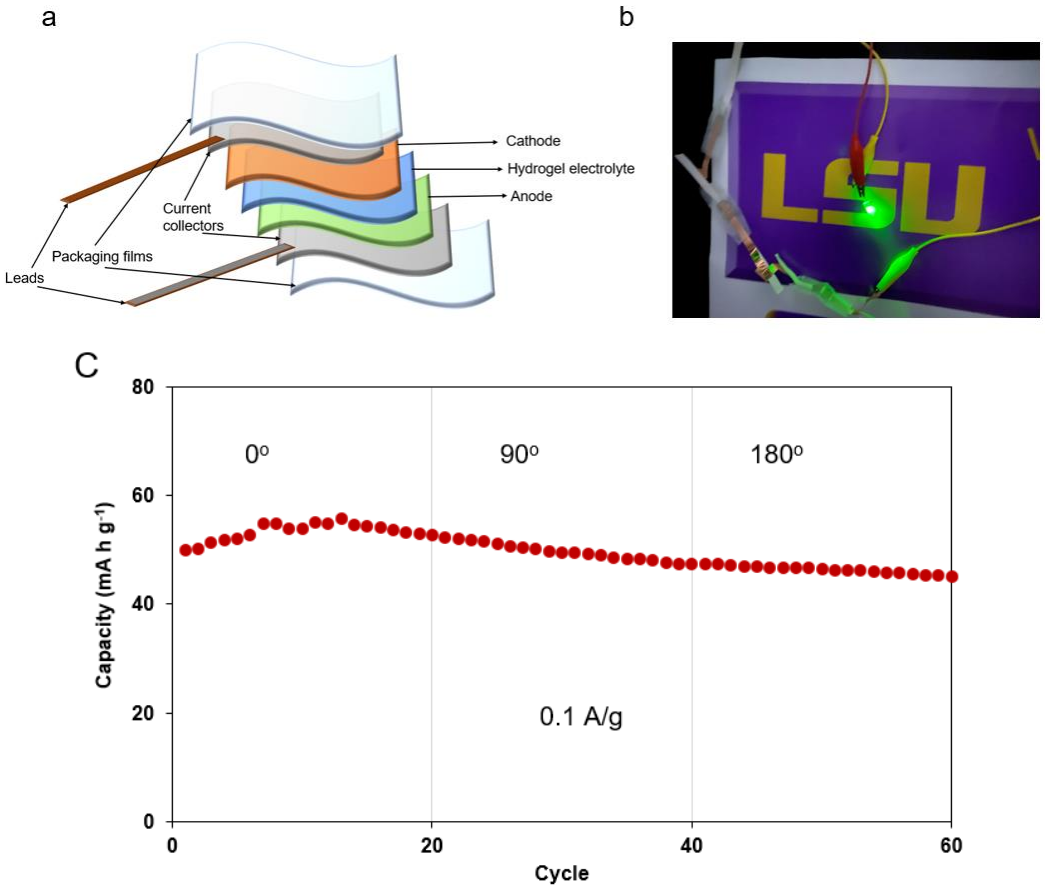

Figure 3.10. a) Schematic of the fabrication of the flexible AIB with PANI as the anode 3M $(NH_4)_2SO_4$ QSS electrolyte and $NH_4V_3O_8.2.9H_2O$ as cathode b) An image showing 5 AIBs cicuit connected in series powering an LED light (c) Cycling at a specific current of 0.1 A g-1 at different bending angles

Finally, we examine the mechanical strength of the full flexible battery while it undergoes electrochemical cycling. Figure 3.10a presents a schematic showing the sandwich structure of the flexible battery. In figure 3.10b, five AIBs are connected in a series circuit to power an LED light, demonstrating the potential of these batteries for practical applications. Figure 3.10c shows the cycling performance of the flexible battery consisting of the 3 M hydrogel electrolyte while it is bent at different angles. The battery remains flat for the first 20 electrochemical cycles then is bent at 90 degrees for subsequent 20 cycles, followed by being bent at 180 degrees for another 20 cycles. It can be seen the capacity of the battery slightly increases then decreases when the battery is flat. Overall, the battery shows a remarkable 98% capacity retention after being bent at 90° and 180°. The flexible AIB in this work shows a capacity of 58 m A g^{-1}. There has been few work concerning flexible full AIBs in literature, and the capacity of our battery is higher than the capacity of 40 mA h g^{-1} from a flexible AIB based on PAM electrolyte reported recently.[1] These

results demonstrate the full QSS AIB battery consisting of the concentrated hydrogel electrolyte can maintain its electrochemical performance while being deformed, showing excellent mechanical robustness and flexibility of the battery. Additionally, the AIB battery using the liquid electrolyte in this work shows superior capacity retention of 95% after 400 cycles with comparable final capacity, which is much higher than the capacity retention of 73.3% after 400 cycles from the aqueous AIB battery based on PANI and ammonium metavanadtes reported in literature.[82]

3.4 Conclusion

In summary, the non-metallic NH_4^+ ion redox chemistry is utilized to demonstrate a full flexible AIB, composed of the $NH_4V_3O_8 \cdot 2.9H_2O$ cathode and the polyaniline anode as well as the concentrated hydrogel electrolyte containing ammonium sulfate and xanthan gum. As a proof of concept first, the cathode and the anode are assembled with liquid aqueous 1 M $(NH_4)_2SO_4$ electrolyte for electrochemical performance evaluation. The resulting battery delivers an impressive capacity of 121 mA h g^{-1}, stable cycling performance and a capacity retention of 95% after 400 cycles. As for the QSS AIB, the salt concentration in the gel electrolyte is tuned to maximize the battery performance, and it is found that the battery based on the gel electrolyte prepared from 3 M salt solution shows the highest capacity of 55 mAh g^{-1} and the best performance can be ascribed to the increased ionic conductivity, reduced side reactions, and suppressed active material dissolution resulted from the high salt concentration. This battery also delivers excellent cycling perfomance with a high capacity retention of 98% after 250 cycles. This battery also maintains the capacity whilst bent at 90 and 180 degrees and undergoing electrochemical cycling silmultaneously, demonstrating remarkable mechanical strength and flexibility. As such, the full flexible AIB in this work shows high potential as a safe and low-cost power source to meet the demands of the fast expanding market of wearable electronics.

Chapter 4. V_2O_5 Intercalated with Polyaniline for Improved Kinetics in Aqueous Ammonium-ion Batteries.

4.1 Introduction

Hydrated V_2O_5 has been reported to be capable of intercalating NH_4^+ ions by forming strong hydrogen bonding between NH_4^+ ion and bi-layered hydrated V_2O_5 because of the layered tunable structure and multiple redox states of vanadium. [99] This material delivers a capacity of 90 mA h g^{-1} at a specific current of 0.1 A g^{-1}, and the interlayer spacing withing the V-O_6 framework is found to be 0.87 nm. Such interlayer distance in the V_2O_5 framework is relatively small for NH_4^+, sterically hindering the ion diffusion kinetics and eventually leading to poor electrochemical performa[3]nce.[100,101] Layered vanadium-based materials are promising materials for NH_4^+ storage due to their easy synthesis, low cost, multiple electron transfer feature, and stable structure.[102] To improve their capacity, the pillar strategy has been explored to enhance the structural integrity of vanadium-based layered compounds during the charge (de)intercalation processes. A cation or lattice water can be used as pillars in the layered structure, improving its structural stability thereby improving the rate and cycling capability particularly in zinc ion batteries.[103,104] It has been shown that NH_4^+ can form hydrogen bonds with lattice water in the layered $V_2O_5 \cdot nH_2O$ for enhanced battery performance. However, large hydrated NH_4^+ ions could also be formed if the NH_4^+ ions forge coordination bonds with lattice water molecules, which can affect the NH_4^+ ion (de)intercalation. Ca^{2+}, Li^{2+}, Na^+ and Mg^{2+} ions have been employed as pillars in the interlayers of vanadium-based compounds to improve the transport properties of charge carriers in the host structure.[105] Nevertheless, the NH_4^+ ion transport kinetics will be limited by the coulombic interactions between the NH_4^+ ion and the anions in the host structure. It has been reported that oxide cathodes show more sluggish kinetics than their sulfide due to the stronger electronegativity of O^{2-} compared to S^{2-}.[106] In bi-layered V_2O_5 nH_2O, the structural water which acts as pillars would have shielding effect for NH_4^+ ions such that the formation of hydrated ions would decrease their interactions with oxygen in the lattice. During the (de)intercalation processes of NH_4^+ ions, there is loss of water molecules, which would compromise the structural integrity of the electrode material causing battery failure.[107] Considering all the factors above, an effective strategy would be to develop a vanadium-based material with enlarged interlayer spacing to accommodate large NH_4^+ ions with excellent structural integrity while shielding the coulombic interactions with lattice water molecules simultaneously.

Earlier in chapter 2 polyaniline (PANI) was demonstrated that it can store NH_4^+ ions with an impressive capacity of 160 mA h g^{-1} at a specific current of 1 A g^{-1} due to its high conductivity and porous structure for accommodation of more NH_4^+ ions.108 In the present study, we introduce PANI between the bilayers of V_2O_5 nH_2O, thereby expelling water molecules, resulting in PANI-intercalated V_2O_5 (PVO) with enlarged interlayer spacing to enhance the NH_4^+ ion kinetics for

---

This chapter previously appeared as: Kuchena, Shelton F., and Ying Wang. "V_2O_5 intercalated with polyaniline for improved kinetics in aqueous ammonium-ion batteries." *Electrochimica Acta* 425 (2022): 140751. Copyright Elsevier 2022 : https://www.sciencedirect.com/science/article/pii/S0013468622009100

aqueous ammonium ion batteries. Though the PANI-intercalated vanadium oxide has been used in lithium-ion and zinc-ion batteries, it has never been explored in ammonium-ion batteries and this work is the first effort to synthesize and optimize this material for this new application. The PANI not only expands the interlayer spacing but stabilizes the layered V_2O_5 structure serving as pillars in the interlayer structure of vanadium oxide. Furthermore, the intercalation of PANI in the layered V_2O_5 has a π-conjugated structure with electron reservoir that can improve the coulombic interactions between the NH_4^+ ions and the V-O framework.99 Additionally, the PANI in V_2O_5 will be able to form a dual storage mechanism in which the NH_4^+ ions will interact with the V-O framework in V_2O_5 and be intercalated in PANI too, since PANI has been demonstrated to have NH_4^+ storage capability. Finally, the composition of PVO, or the ratio between PANI and V_2O_5 can be tuned and optimized, to maximize the battery performance.

NH_4^+ ion redox chemistry is dominated by non-ionic chemical bonding such as hydrogen bonding with some covalent bonding in nature which plays a significant role in electrochemical performance of the battery. In this work, an in-situ intercalation technique is utilized to synthesize polyaniline-intercalated vanadium oxide with a nanoflower morphology for increased surface area and enhanced NH_4^+ ion (de)intercalation kinetics. Through this strategy, an interlayer spacing of 13.99Å between V-O layers is reached, offering large diffusion channels to accommodate NH_4^+ ions which have an ionic radius of 1.48 Å and a hydrated radius of 3.31Å. The diffusion kinetics of the NH_4^+ ions, influenced by the hydrogen bonds formed between NH_4^+ ion and O^{2-} in the host structure, are thus effectively enhanced by the unique π-conjugated structure of PANI, leading to high capacity, improved rate capability and improved cycle life. The as-prepared PANI-intercalated V_2O_5 (PVO) demonstrates stable, ultrafast NH_4^+ ion electrochemical storage based on hydrogen bond chemistry as elucidated by X-ray photoelectron spectroscopy and Raman spectroscopy characterizations. Additionally, the composition of the PVO electrode is optimized with respect to the amount of PANI between the V-O layers. The PVO with an optimal composition exhibits the best overall electrochemical performance, delivering a high capacity of 192.5 mA hg^{-1} and 39 mA hg^{-1} at specific currents of 1 and 20 A g^{-1} respectively, as well as a stable cycle life with a capacity retention of 98% at a specific current of 10 and 20 A g^{-1}. As such, the present work provides critical insights into the design of promising electrode materials for emerging aqueous non-metal batteries with intrinsic safety and reduced cost.

4.2 Experimental Section

4.2.1 Synthesis of PVO and HVO

An in-situ hydrothermal method was used to synthesize the PANI-intercalated V_2O_5. 1 mmol of commercial V_2O_5 powder (Sigma Aldrich, 98%) was dispersed in 30 mL of DI water under stirring at room temperature. After they fully dissolve, 60 μL of aniline were added under continuous stirring. To adjust the pH of the solution to 3, 3 M HCl was added dropwise under stirring at room temperature and continuous stirring was maintained for 30 mins. The solution was then transferred into a 50 mL Teflon autoclave and put into an oven at 120°C for 24 h. After 24 h, the autoclave was removed from the oven and cooled down naturally to room temperature. Dark

green precipitates were collected and washed with DI water and ethanol three times. After washing the precipitates were dried at 60°C overnight. In this work, three different amounts of aniline (10 μL, 60 μL and 180 μL) were used to prepare three PVO samples, designated as PVO10, PVO60 and PVO180.

Synthesis of HVO*:* To fully recognize the effect of PANI on hydrated V_2O_5, hydrated V_2O_5 (HVO) was synthesized according to the following procedure for comparison purpose. 1 mmol of commercial V_2O_5 powder (Sigma Aldrich, 98%) was dispersed in 40 mL of DI water containing 1mL H_2O_2 (30%) under stirring. Continuous stirring was maintained for 30 mins at room temperature. The solution was then transferred into a 50 mL Teflon autoclave and put into an oven at 120°C for 6 h. Afterwards the autoclave was removed from the oven and cooled down naturally to room temperature. The precipitates were collected and washed with DI water and ethanol three times. After washing, the precipitates were dried at 60°C overnight.

4.2.2 Materials Characterization

The X-ray diffraction (XRD) data were collected on a Rigaku MiniFlex X-ray diffractometer with Cu Kα radiation (λ= 1.5405 Å). An FEI Quanta 3D FEG field emission scanning electron microscopy (FESEM Scanning electron microscopy (SEM) was used for imaging. X-ray photoelectron spectroscopy (XPS) measurements were conducted using an AXIS165 spectrometer. A Renishaw in Via Reflex Raman Microscope was used for Raman spectroscopy characterization. Thermogravimetry (TGA) data were collected using an SII STA7300 analyzer under nitrogen.

4.2.3 Electrochemical Measurements

The electrode was prepared by mixing the as-prepared PVO/HVO powder, carbon black and carboxymethyl cellulose binder (CMC) binder, with a weight ratio of 7:2:1. The slurry was layered evenly onto a carbon fiber paper, followed by drying in oven at 60 °C. The mass of the electrode material is about 3 mg/cm$^{2.}$ The electrochemical performance was evaluated in a three-electrode cell, with PVO/HVO electrode as the working electrode, graphite rod as the counter electrode, and saturated Ag/AgCl as the reference electrode, in an electrolyte solution of 0.5 M $(NH_4)_2SO_4$. Cyclic voltammetry (CV) measurements and galvanostatic charge- discharge (GCD) tests were conducted in a potential range of −0.5 to –1.0 V on an electrochemical workstation CHI 6504C (CH Instruments, Inc., Austin, TX).

4.3 Results and Discussion.

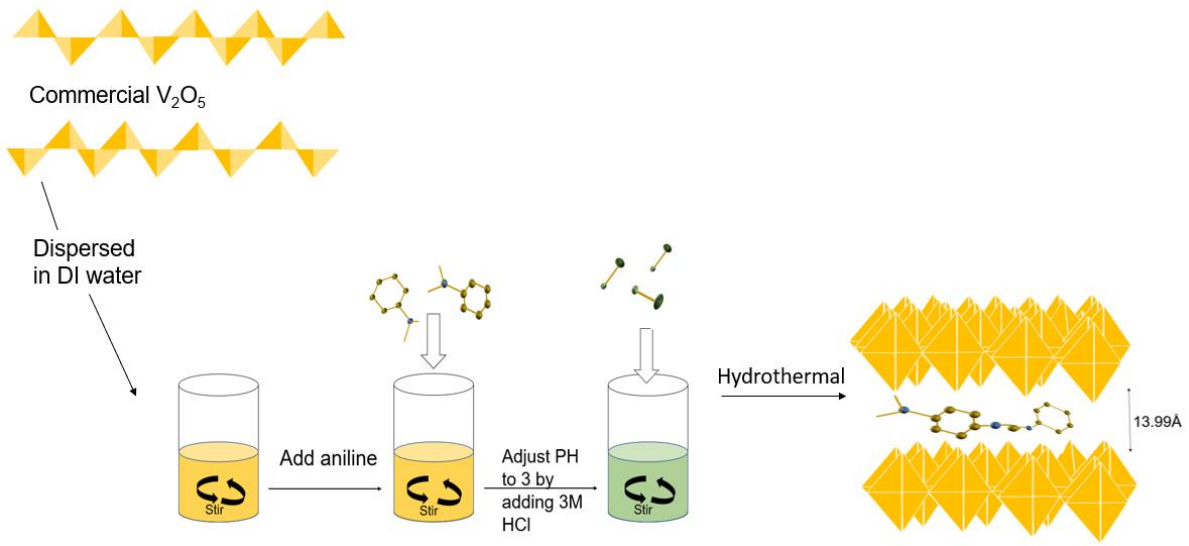

Figure 4.1. Schematic showing the synthesis procedure of PVO with enlarged interlayer spacing.

The PANI-intercalated V_2O_5 (PVO) is synthesized using a hydrothermal method through acidic oxidation polymerization of aniline. In this synthesis, dissolution and recrystallisation of V_2O_5 occurs along with the in-situ polymerization of aniline, as illustrated in figure 4.1. During the hydrothermal process, dissolution of pure V_2O_5 results in free vanadium ions, followed by nucleation and growth. As the reaction proceeds, PANI is formed through the protonation of aniline then inserted into the interlayers of the orthorhombic V_2O_5. The insertion of aniline occurs simultaneously with water molecules being embedded in the V-O layers, which is very beneficial as they will act as pillars to improve the structural integrity of the material. As a result, the interlayer spacing V_2O_5 is expanded significantly. The conductivity of the as-formed PANI polymer chain is also improved by the presence of HCl acid which causes the protonation of PANI leading to the formation of quinoid and benzenoid rings in the form of polarons.[109] At the same time, the partial reduction of V^{5+} to V^{4+} and the presence of V^{5+}/V^{4+} enhances the ion/electron transfer of the sample. The overall chemical reaction is shown below:

$$x C_6H_5NH_2 + V_2O_5 \cdot nH_2O + (2x\text{-}3y)/2O_2 \rightarrow (C_6H_4NH)_{x-y}(C_6H_5NH_3)_y V_2O_5 \cdot mH_2O + (2x\text{-}3y)/2H_2O_2 + (n\text{-}m)H_2O. \quad [110]$$

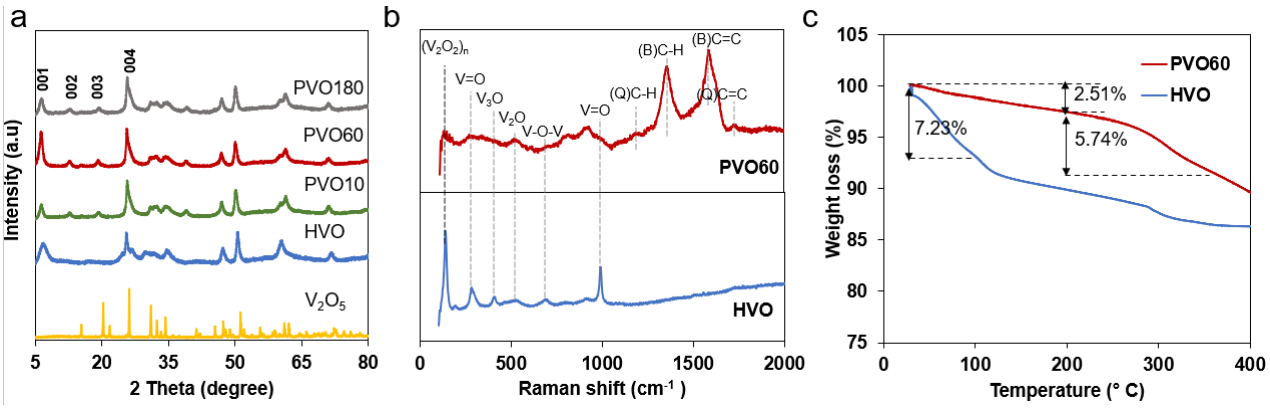

Figure 4.2. a) XRD patterns of HVO, PVO10, PVO60 and PVO180, b) Raman spectra of HVO and PVO60, c) TGA curves of HVO and PVO60.

To unveil the effect of PANI content on the electrochemical property of PVO, three different amounts of aniline are used respectively in the synthesis above, that is, 10, 60 and 180 µl. The resulted PVO samples are designated as PVO10, PVO60, and PVO180, respectively. Figure 4.2a presents the XRD patterns of anhydrous V_2O_5, hydrated V_2O_5 (HVO), PVO10, PVO60, and PVO 180. A peak appears at the low angle corresponding to the *(00l)* planes for all the samples, revealing lamellar-ordered assembly of layers along the c-axis in the crystal structure.[111] Only a set of *(00l)* are observed in the XRD patterns for both V_2O_5 and PVO samples, illustrating one-dimensional stacked layered materials.[112]

Table 4.1. The interlayer spacings of HVO and PVO samples calculated based on the (001) peak in their XRD patterns.

	Diffraction peak position (°)	**d- interlayer spacing (Å)**
HVO (V_2O_5)	6.85	**12.91**
PVO10	6.48	**13.64**
PVO60	6.32	**13.99**
PVO180	6.28	**14.08**

The interlayer spacings of these samples can be determined using Braggs' law and are presented in Table 4.1. It is found that PVO10, PVO60 and PVO180 have an enlarged interlayer distance of 13.64 Å, 13.99 Å and 14.08 Å, compared to HVO having a smaller interlayer spacing of 12.91Å corresponding to a sharp peak at 6.85°. This increase in the interlayer spacing of PVO can be attributed to the replacement of H_2O molecules by larger polymer chains of PANI in the interlayers of V_2O_5. And it is observed that the interlayer distance of PVO increases with the amount of PANI intercalated in V_2O_5.

Figure 4.2b displays Raman spectra of PVO60 and HVO, both showing peaks below 1000 cm^{-1} attributed to the V-O crystalline structure. The spectrum of PVO60 also contains peaks above

1000 cm^{-1} ascribed to organic groups in PVO, whereas that of HVO does not have these. The Raman spectrum of PVO60 reveals peaks at 1080 and 1589.22 cm^{-1}, corresponding to the C-H and C=C group vibrations of the quinoid ring, while the peaks at 1194.41 and 1359.87 cm^{-1} represent the C-H and C=C group vibrations in the benzenoid ring and another peak at 1297.4 cm^{-1} refers to the $C\text{-}N^{+}$ group, confirming incorporation of PANI in V-O layers. It can be seen from the spectra of HVO and PVO that they have peaks with similar positions below 1000 cm^{1}, indicating V_2O_5 is structurally preserved after the insertion of PANI, which is consistent with the XRD results. The compositions of the as-synthesized HVO and PVO60 are further examined using thermogravimetric analysis (TGA) as shown on figure 4.2c. The HVO sample shows approximately a weight loss of 7.23% at 100°C, caused by the removal of physically absorbed water; further weight loss is observed at higher temperatures due to the loss of structural water. Based on these results, it can be calculated that there are 1.55 water molecules per unit of V_2O_5. On the other hand, PVO60 presents the first weight loss of only 2.51% at 200°C, because the structural water molecules are partially replaced by PANI monolayer. As PVO60 is heated from 200 to 400°C, further weight loss is observed which is ascribed to the removal of the organics or PANI. The PVO sample before heating is green, but turns yellow after heating, suggesting yellow V_2O_5 is left after organics being burnt off.

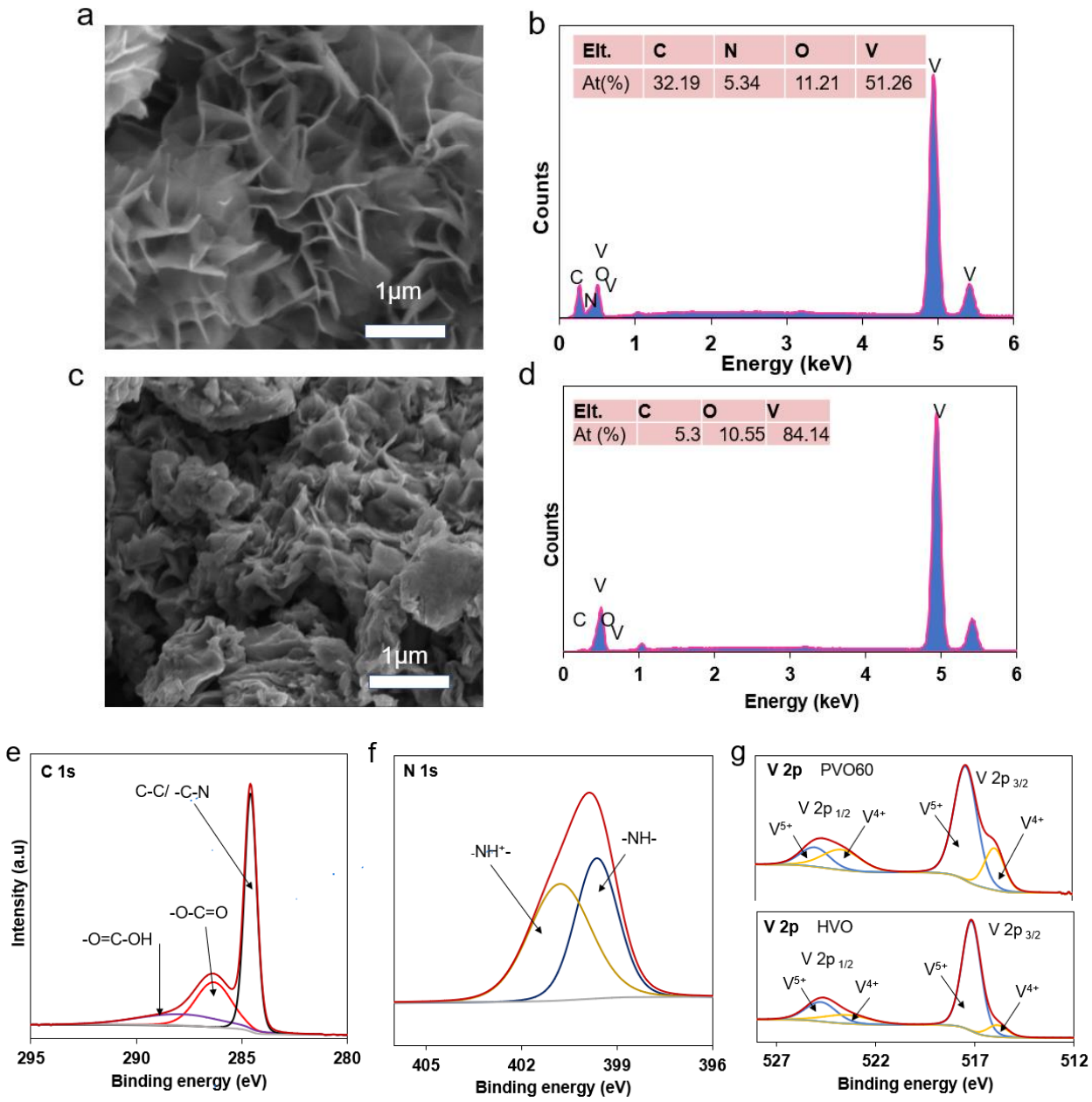

Figure 4.3. a) SEM image of PVO60, b) EDS spectrum of PVO60, c) SEM image for HVO d) EDS spectrum for HVO e) SEM image of HVO, f) EDS spectrum of HVO; XPS g) C 1s, f) N 1s, g) V 2p spectra of PVO60.

Figure 4.3a exhibits the scanning electron microscopy (SEM) image of PVO60, showing a morphology of nanoflowers composed of uniform nanosheets, which is much more porous than the fibrous structure of HVO as displayed in its SEM image in figure 4.3c. The corresponding EDS spectrum of the PVO60 is presented in figure 4.3b, revealing the V, O, C and N elements, while

the EDS spectrum of the HVO in figure 4.3d only shows V, O, and C elements, again indicating the intercalation of PANI into V_2O_5 framework in the PVO60 sample.

XPS is then performed to investigate the valence state of the elements in PVO and HVO. Figure 4.3e presents the C1s spectra for PVO60, showing three peaks located at 284.50, 286.32 and 287.88 eV. The peak at 284.50 eV corresponds to the PANI group of C-C, C=C or C-H, and the peaks at 286.32 and 287.88 eV are from the benzenoid carbon, C-N/C=N and C=O. The peak located at 287.88 eV represents the group O-C=O that forms electrostatic bonds between the polymer and the V_2O_5 framework, and this interaction further stabilizes the framework with the enlarged interlayer spacing.[113] Figure 4.3f displays the N 1s spectra from PVO60, showing two nitrogen groups at 399.62 and 400.78 eV, attributed to -NH- (45.53%) and $=NH^+$ (54.47%) groups in PANI. The valence state of nitrogen in PANI is very important as the electrochemical property of PANI is dependent on it. The ratio of non-protonated imine -NH- (45.53%) and protonated amine $=NH^+$ (54.47%) is nearly 1, suggesting the emeraldine state of the PANI.[114]The presence of HCl acid during synthesis would result in non-redox doping, in which an imine nitrogen gets protonated to become a polaron that has delocalized spin and charge in the polymer backbone.108 The emeraldine salt has very good conductivity which further improves the rate capability of PVO. As such, PVO has a dual storage mechanism as NH_4^+ ions can be intercalated in both the V_2O_5 framework and PANI, leading to an enhanced capacity. [115,116]

Figure 4.3g shows the V2p spectra from PVO60 and HVO, with characteristic peaks at 517.18 and 524.75 eV related to V^{5+} in PVO, and the peaks at 515.87eV and 523.44eV from V^{4+} in PVO. The positions of V2p peaks from PVO are almost like those from HVO (517.32 and 524.72 eV for V^{5+}, 515.69 and 522.97eV for V^{4+}), suggesting the V_2O_5 framework and its oxidation state are maintained after the intercalation of PANI. According to the XPS peak fitting, the difference between V $2p_{3/2}$ and V $2p_{1/2}$ for V_2O_5 should be 7.5 eV, which is like the difference between these peaks for PVO60, again indicating the well-preserved V_2O_5 framework during polymerization/intercalation. [117,118]

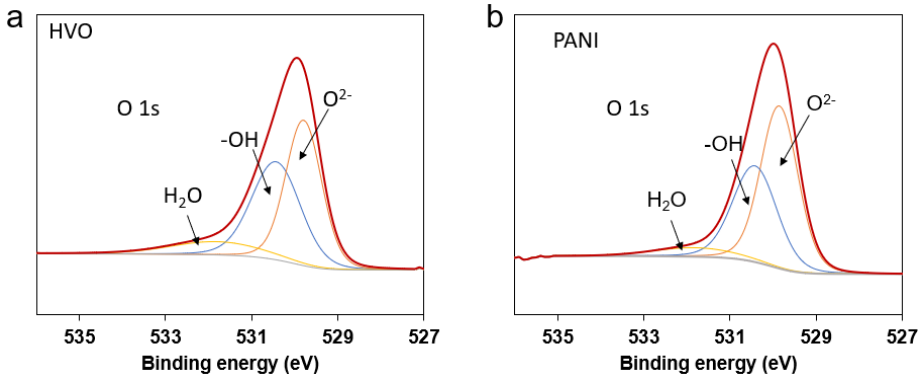

Figure 4.4. The O 1s XPS spectra of a) HVO and b) PVO60.

Figures 4.4 a and b reveal the O1s spectra from HVO and PVO60, with the peaks assigned to O^{2-}, -OH group and H_2O confirming the bridging -OH group and water molecules in the

interlayers. Just the peak intensities of the O 1s groups from HVO and PVO60 are different, with those from PVO60 have lower intensities attributed to the removal or H_2O and -OH groups during the PANI insertion into the V_2O_5 framework.

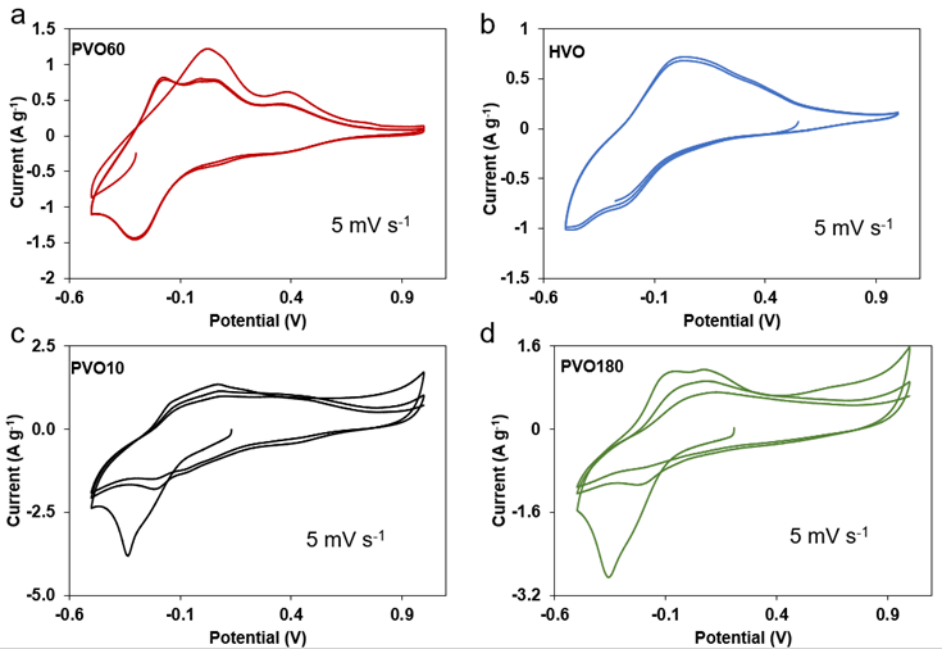

Figure 4.5. Cyclic voltammetry curves of a) PVO60, b) HVO, c) PVO10, d) PVO180, at a scanning rate of 5 mV/s

Figure 4.5 presents the first three cycles of CV curves for HVO, PVO10, PVO60, and PVO180. The CV profile of PVO has additional distinct peaks compared to that of HVO. On the CV curve of PVO60 in Figure 4.5a, the cathodic peaks are located at -1.45 and 0.4 V in the first three reductions scans, and both do not shift during the cycling, showing high reversibility during the (de)intercalation of NH_4^+ ions in PVO60. From figure 4.5b, the CV curve of HVO has one reduction peak at -0.251 V which is different from the one observed in PVO (Figure 4.5a, c-d), mainly attributed to the different storage mechanism in these cathode materials. The initial three oxidation peaks scans in PVO60 clearly overlap with oxidation peaks at 0.415, 0.07, -0.01 and -0.15V. As for HVO, there is only one oxidation peak at 0.678 V. The observation of many reduction and oxidation peaks in PVO60 suggests a multistep reaction process for the NH_4^+ ion during (de)intercalation mechanism. Furthermore, the CV curves of the first three cycles of PVO60 (Figure 4.5a, with the second and third scan almost identical) have better repeatability than those of other PVO electrodes (Figure 4.5c and d), indicating its good structural integrity and desirable reversibility.[119] Additionally, it can be seen that the peaks on the CV curves of PVO10 and PVO180 are lower and broader compared to those from PVO60, due to the electrostatic interactions between the charged species. The existence of interaction forces between the adsorbed molecules and the electrode material causes a change in the width of the peak. If the attraction forces dominate, the peak becomes narrower and sharper, and the number of electroactive sites on the area increases. When the peak is broader, the repulsion forces predominate.[120,121] The CV curves of PVO60 have relatively sharper peaks compared to those of HVO, PVO10 and PVO180,

suggesting a more efficient electrochemical process in the battery cell based on PVO60. It is noted that the CV profile of PVO60 is different from those reported for pure PANI [109] and bi-layered V_2O_5,[122] suggesting the ammonium-ion storage mechanism in PVO60 is not simply the addition of PANI and V_2O_5, owing to the hydrogen bonds with covalent nature formed between NH_4^+ ion and O^{2-} in the host structure that are effectively enhanced by the π-conjugated structure of PANI.

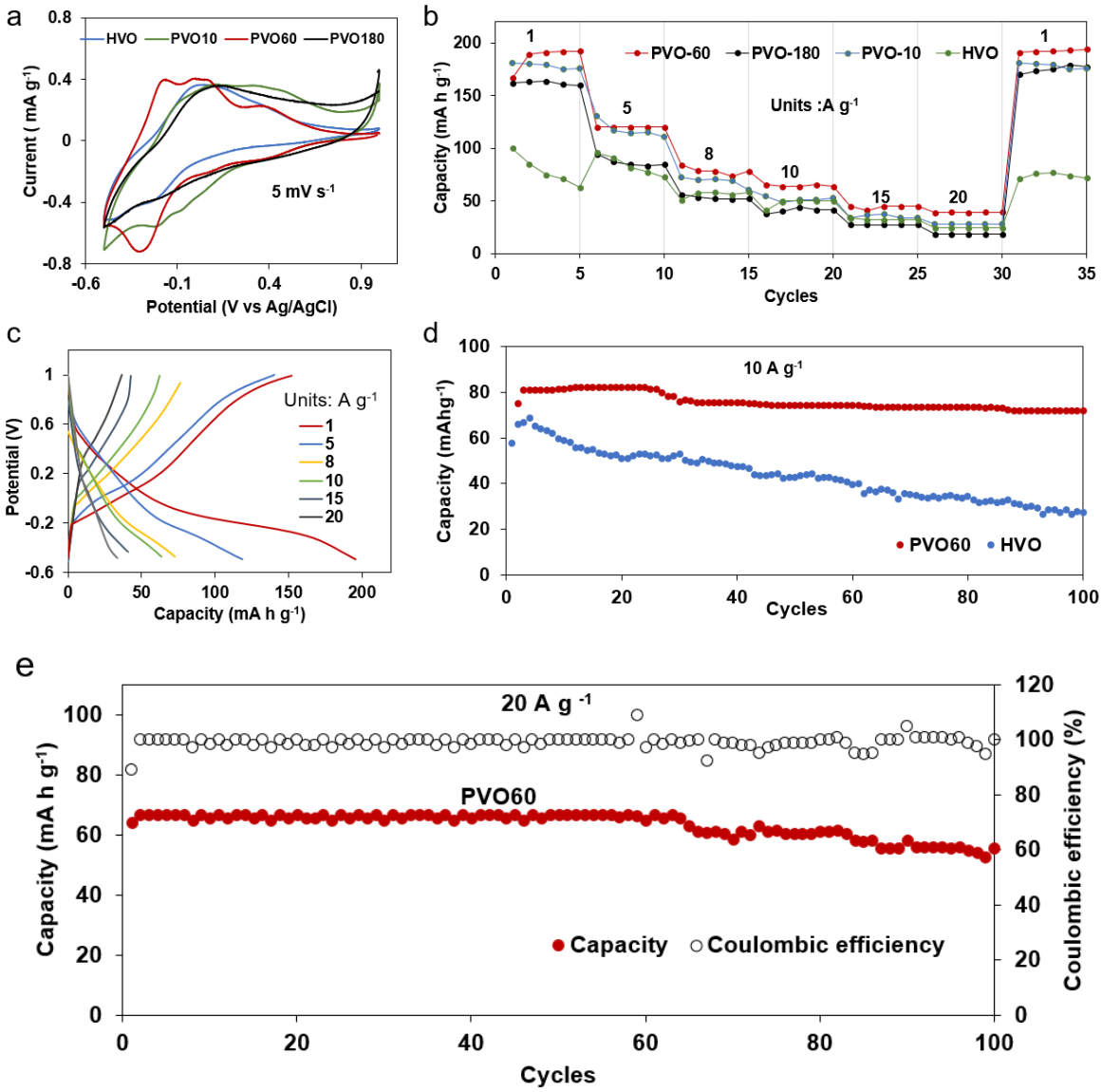

Figure 4.6. a) CV curves of HVO, PVO10, PVO60 and PVO180; b) Rate performance of HVO, PVO10, PVO60, and PVO180; c) Charge-discharge curves of PVO60 at various specific currents; d) Cycling performance of HVO and PVO60 at 10 A g^{-1}; d) Cycling performance of PVO60 at 20 A g^{-1}.

The cyclic voltammogram (CV) curves for the batteries based on HVO, PVO10, PVO60 and PVO180 are recorded in a voltage range of -0.5 – 1.0V (vs Ag/AgCl) at a scan rate of 5 mV s^{-}

[1] , as shown in figure 4.6a. In the electrochemical evaluation of the AIBs, the electrolyte used is 0.5 M $(NH_4)_2SO_4$ solution, because it is discovered in our previous publication that this electrolyte is only mildly acidic with a pH of 5.3 so that the contribution of protons and/or hydronium towards capacity would be minor.[108] In this earlier work from our group, a CV scan is performed for the AIB using the electrolyte of H_2SO_4 solution with the same pH of 5.3, and it is found that the current from the resulted CV curve is less than 2.0% of the CV current from the AIB using 0.5 M $(NH_4)_2SO_4$ as the electrolyte, confirming that the contribution of protons and/or hydronium ions to the capacity is very minor in the AIB using 0.5 M $(NH_4)_2SO_4$ as the electrolyte.[108]

The AIB cathode materials reported so far usually present relatively unsatisfactory rate performances because of the irreversible structural damages caused by the large ionic radius of NH_4^+ ions and the slow transfer kinetics due to the intensive polarization of NH_4^+ ions. Nevertheless, the battery cells based on HVO, PVO10, PVO60 and PVO180 all exhibit decent rate capability when subjected to different galvanostatic evaluations ranging from 1 to 20 A g^{-1} over a potential window of -0.5 to 1 V, as shown in figure 4.6b. Battery consisting of PVO60 electrode demonstrates the highest reversible capacities of 192.50, 120.14, 78.44, 65.50, 45.04, and 39.0 mA h g^{-1} at a specific current of 1, 5, 8, 10, 15 and 20 A g^{-1}, which are higher than those of HVO exhibiting 100, 77.5 56.2 50, 32 and 24.38 mA h g^{-1} at the same specific currents respectively. These results clearly show that the insertion of PANI between the V-O layers of V_2O_5 is very effective in increasing the capacity for NH_4^+ storage. It is important to note that a capacity decay of only 37.6% is observed in PVO60 when the specific current is increased from 1 to 5 A g^{-1}. Furthermore, a capacity of 39 mA h g^{-1} is obtained at a very high specific current of 20 A g^{-1} with a discharge time of 7.02 s after withstanding different specific currents, indicating the ultrafast, stable transportation kinetics and good rate capability of PVO60. When the specific current is changed back to 1 A g^{-1}, a discharge capacity of 191.94 mA h g^{-1} is restored, suggesting a strong tolerance ability for NH_4^+ ion transportation and excellent structural integrity of PVO60. The capacities of PVO10 are 179.00, 114.03, 68.78, 50, 37.5, and 28.05 mA h g^{-1}, and PVO180 delivers 163.30, 77.50, 52.2, 43.89, 27.5 and 18.33 mA h g^{-1}, at specific currents of 1, 5, 8, 10, 15 and 20 A g^{-1} respectively. It is found that PVO10 has higher capacity than PVO180 while PVO60 presents the highest capacity among the three. It should be noted that PVO10 and PVO60 exhibit better rate performances than the cathodes reported before.[8 -108] The rate capabilities of PVO180 and PVO10 are inferior when compared to PVO60, mainly because the driving force for the oxidation of aniline is based on the redox potential of V_2O_5, and the oxidative polymerization of organic monomers would be limited by the amount of reduced V^{4+} center in the V-O with no oxidant added in the synthesis, resulting in the electrical conductivity of the hybrid bronzes reaching a peak, thereby limiting the oxidant available for polymerization of aniline.[123, 124]

It appears that PVO60 has the optimal composition for the best battery performance. Hence, we focus on PVO60 for further electrochemical testing and other characterizations. Figure 4.6c summarizes the charge/discharge profiles of PVO60 at various specific currents. This electrode shows a high capacity of 195.60 mA h g^{-1} with a Coulombic efficiency of approximately 80% at 1A/g, whilst the Coulombic efficiency is approximately 98% at 20 A/g. It is noted that the discharge curves exhibit a plateau in the voltage range of -0.3 to 0.22 V, corresponding to the intercalation / deintercalation of $NH_4^{+\cdot}$ Additionally, as illustrated in Figure 4.6d, PVO delivers an initial capacity of 80.83 mA h g^{-1} at a high specific current of 10 A g^{-1} with a capacity retention of

98% after 100 cycles showing excellent durability and cyclability, in contrast to the fast decay of HVO that exhibits an initial capacity of 65 mA h g^{-1} and a very low-capacity retention of 38.46% after 100 cycles. Furthermore, PVO60 is cycled at a higher specific current of 20 A g^{-1}, yielding a high capacity of 64.33 mA h g^{-1} and a capacity retention of 97% after 100 cycles, as shown in figure 4.6e.

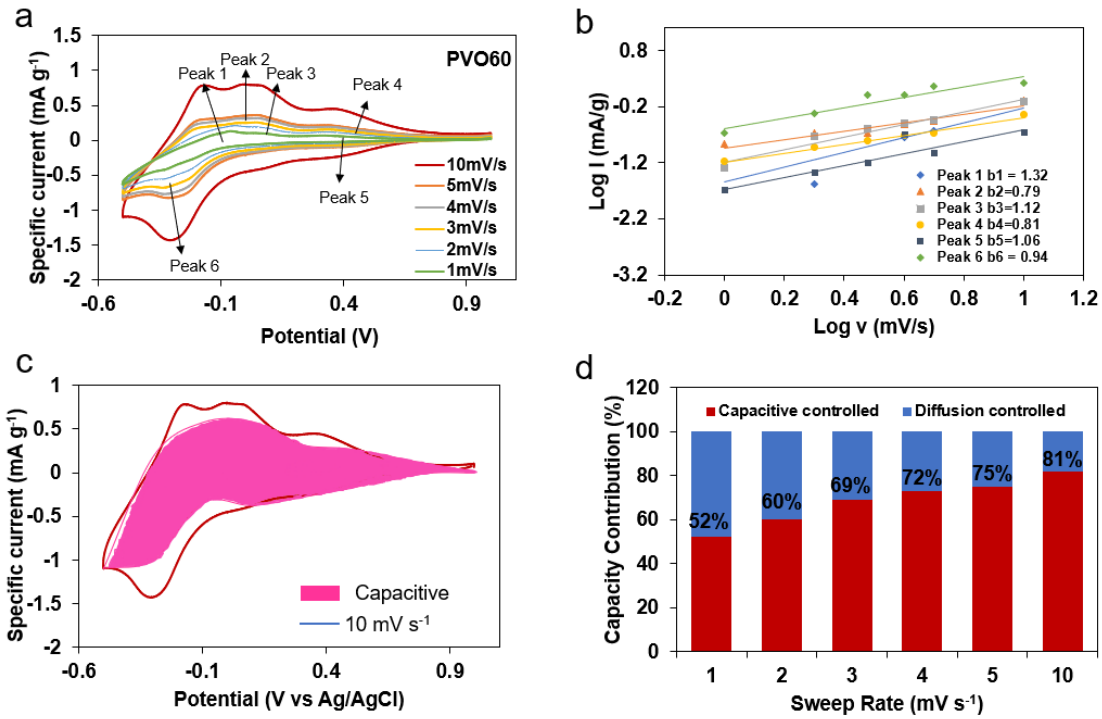

Figure 4.7. a) CV curves of PVO60 at various scanning rates from 1mV/s to 10mV/s; b) b values from the plots of logarithm of the scanning rate (mV/s) as a function of the peak current (mA) from figure 5a; c) CV curve of PVO60 with the shaded area as the calculated capacitive contribution; d) The contribution ratio of diffusion-controlled and capacitive processes to total capacities at various scanning rates.

To explore the kinetics of the AIB based on PVO60, its CV curves are obtained at various scanning rates as displayed in figure 4.7a. The shape of the CV curve is retained at a large scanning rate of 10 mV/s compared to those at low scanning rates, demonstrating a quick response of the NH_4^+ ion storage with a capacitive nature. It is also observed that the peaks shift slightly, due to the kinetics and stress relaxation in the crystal lattice of the cathode at different scanning rates. Overall, the CV profiles maintain similar shapes and the peaks become more pronounced while the scanning rate increases, showing good endurance of PVO60 for the NH_4^+ ingress/egress processes.

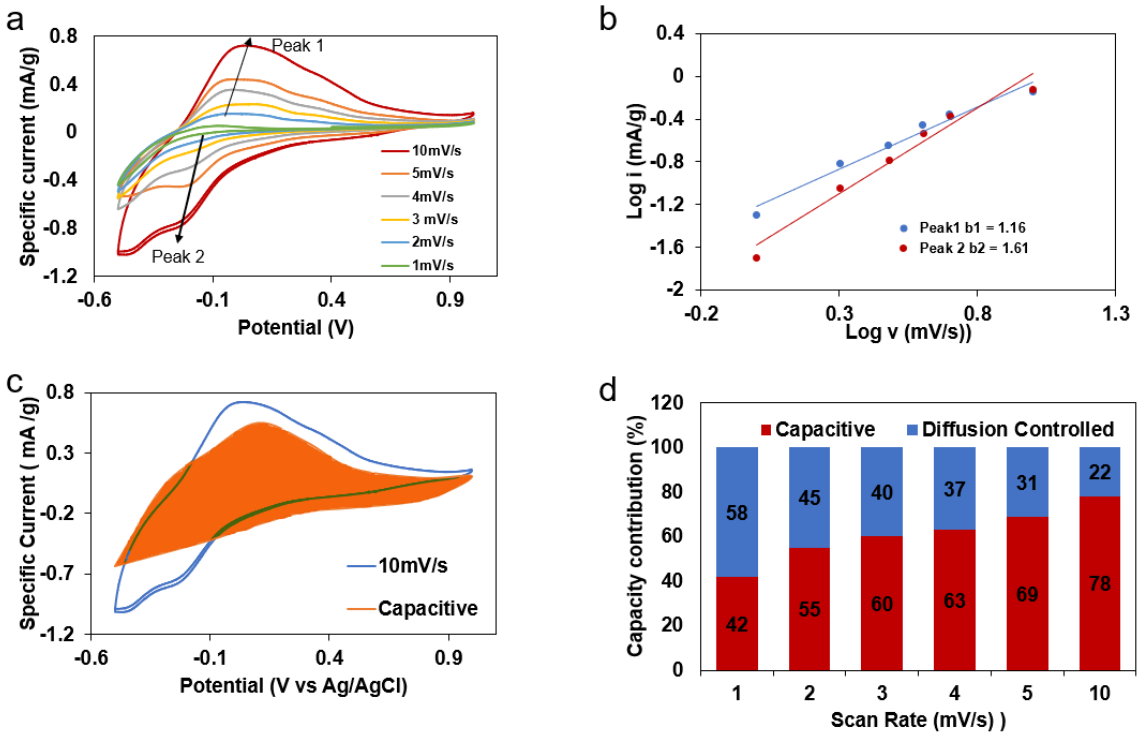

Figure 4.8. CV curves of HVO at different scan rates from 1mV/s to 10mV/s; b) b values from the plot of the logarithm of scanning rate as a function of the logarithm of peak current from a); c) CV curve of HVO with the shaded area as the calculated capacitive contribution; d) Contribution ratio between the diffusion-controlled capacity and capacitive capacity at various scanning rates.

The same characteristics are also observed in the parent material – HVO, as presented in figure 4.8a. The shapes of the CV profiles are preserved at different scanning rates showing two repetitive peaks. As the scanning rate increases, the charging current increases, so does the faradic current. According to the Randles-Sevcik equation, the current is proportional to the square root of the scanning rate which is also proportional to the flux of the concentration of NH_4^+ ions at the surface of the electrode.[121] According to the power law $i = av^b$, where i is the peak current and v is the scanning rate, the b value can be between 0.5–1.0, with b close to 0.5 showing a diffusion-controlled process and b close to 1.0 showing a capacitive process. The rearranged equation log i = b log v + log a can be plotted for a linear relationship between log i vs. log v, as displayed in figure 4.5b. The b values for peaks 1, 2, 3, 4, 5, 6 are determined to be 1.32, 0.79, 1.12, 0.81, 1.06 and 0.94, respectively, illustrating the redox reactions are controlled by capacitive processes. As for the battery based on HVO, the b values for peaks 1 and 2 are 1.16 and 1.61, demonstrating similar capacitive behavior as presented in figure 4.8b. Capacitive (k_1v) and a diffusion-controlled process ($k_2v^{1/2}$) can be separated quantitatively from the current response (i) at a specific potential (V), using the equation below:

$$i(V) = k_1v + k_2v^{1/2}$$

or

$$i/v^{1/2} = k_1v^{1/2} + k_2$$

where k_1 value and k_2 value represent the capacitive and diffusion contributions, respectively.

As illustrated in Figure 4.7c, 81% of the current contribution at 10 mV s^{-1} is due to the capacitive behavior in the case of the PVO cathode, which accounts for its impressive high-rate capability. Regarding the HVO cathode, 79% is due to the capacitive processes as shown in Figure 4.8c. The bar chart in figure 4.7d presents the contribution percentage of the capacitive process over the total processes (capacitive and diffusion-controlled) at 1, 2, 3, 4, 5 and 10 mV s^{-1} from the PVO60 cathode, revealing 52%, 60%, 69%, 72%, 79% and 81% at these scan rates. The capacitive contribution dominates the total capacity and its contribution percentage gradually increase with the increase of the scanning rate. The same phenomenon is observed for the HVO cathode, showing the contribution percentage of the capacitive behavior is 42%, 55%, 60%, 63%, 69% and 78% at 1, 2, 3, 4, 5 and 10 mV s^{-1}, as unveiled in Figure 4.8d.

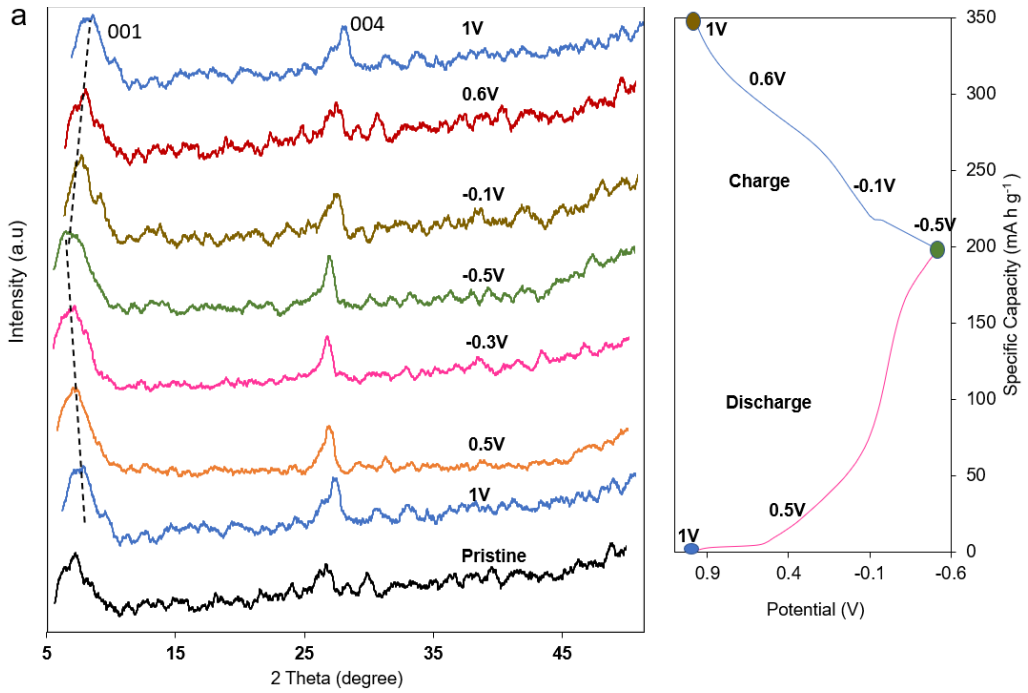

Figure 4.9. XRD patterns of PVO60 at various charge/discharge states.

To further explore the NH_4^+ storage mechanism of the PANI-intercalated V_2O_5, XRD is used to characterize the PVO60 cathode at various charge/discharge states as shown in figure 4.9, to trace its structural change during cycling.[125] The pristine PVO and the PVO charged 1 V display similar XRD patterns with (001) peak showing a slight shift from 6.33° in the initial state to 6.32° in the charged state. Such a slight shift is due to the activation and formation of diffusion channels in the PVO cathode during the early cycling stages. As the discharging starts from 1 V ((001) peak at 6.32°) to 0.5 V (6.30°) to -0.3V (6.29°) to eventually fully discharged state at -0.5 V, the diffraction angle of (001) peak from PVO decreases to 6.27° corresponding to an interlayer spacing of 14.07 Å, while the PVO charged to 1 V has the (001) peak at 6.32° representing an interlayer spacing of 13.98 Å. It can be observed that the interlayer spacing increases of PVO as

more NH_4^+ ions get intercalated into the PVO structure. Upon charging to 1 V, the (001) peak from PVO reverts to 6.32°, indicating its excellent structural reversibility.[4] As such, the crystal structure of PVO is well preserved when discharged, demonstrating that PANI remains inside PVO during the discharge process and the structure of PVO remains intact during cycling.

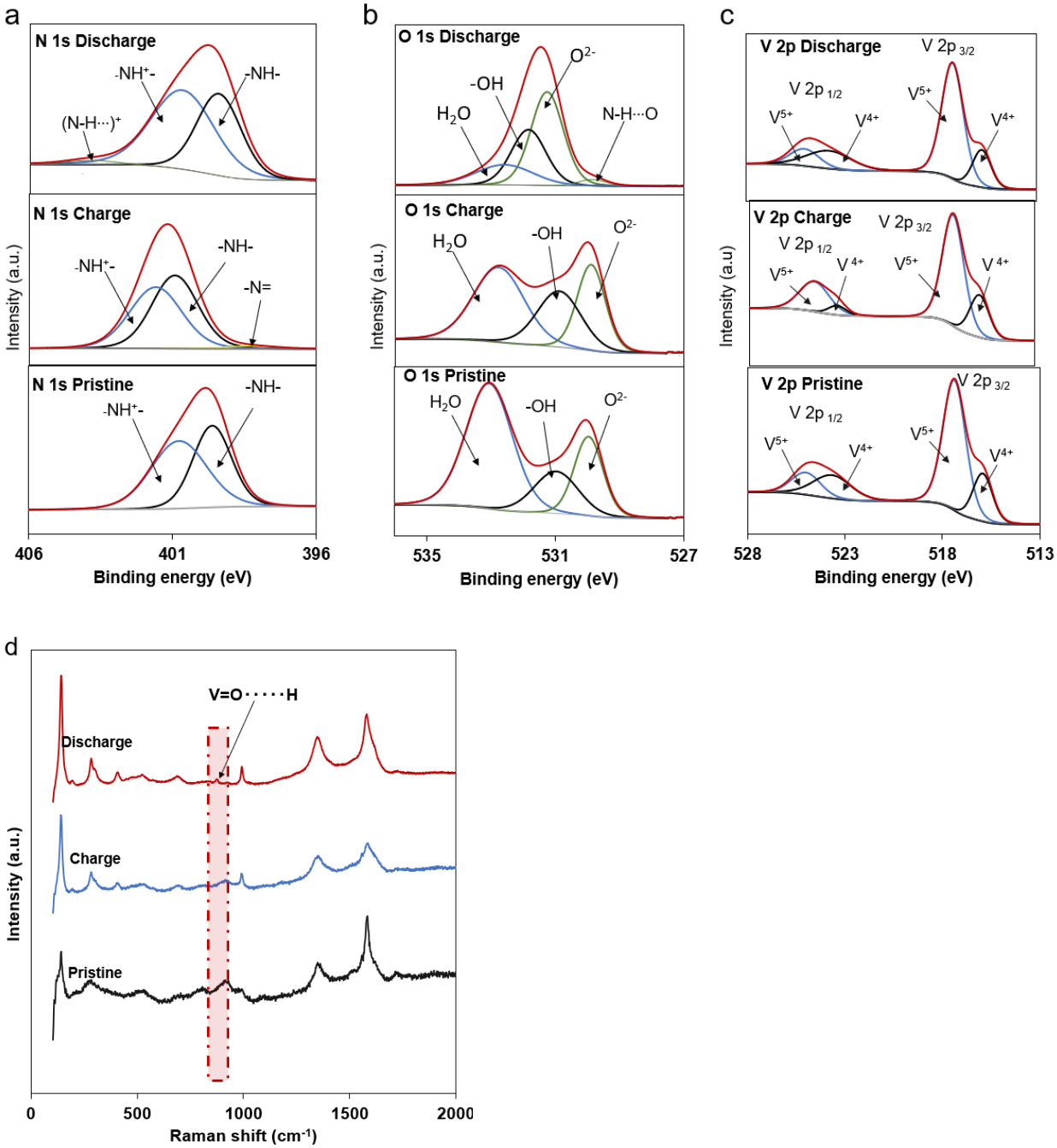

Figure 4.10. XPS a) N 1s, b) O 1s, c) V 2p spectra of PVO60 at pristine, charged, and discharged state; d) Raman Spectra of PVO60 at pristine, charged, and discharged state.

In addition to XRD, XPS is also conducted to examine the PVO60 electrode at the initial, charged, and discharged state, as presented in figure 4.10. Figure 4.10a exhibits the N 1s spectra owing to the PANI in the PVO60 and its electrochemical redox properties depend on the N 1s oxidation state, revealing two peaks at 400.68 and 399.40 eV ascribed to the protonated amine -NH^+- (56.04%) and non-protonated imine -NH- (41.61%) groups in PANI which confirm the emeraldine state of the polymer since the ratio of these two groups is close to 1.[126] In the PVO60 at the charged state, three N 1s groups - NH^+- (50.55%), -NH- (47.65%) and -N= (1.80%) are detected, while the -NH- group decreases to 41.61% and -NH^+- group increases to 56.04% in the discharged PVO60 because of the reduction due to the protonation resulted from the interaction with NH_4^+ ions, as shown in figure 4.10a. During the reduction process, the amount of -N= group decreases because of its protonation to generate -NH- due to the intercalation of NH_4^+ ions. A peak at higher binding energy is also detected at 403.48 eV, which is attributed to the positive center of the hydrogen bond (N-H$\cdots$) $^+$, illustrating the reaction of NH_4^+ with the highly π-conjugated structure of PANI through hydrogen bonding. The hydrogen bonding is confirmed by the O 1s spectra in figure 4.10b which shows (N-H$\cdots$O) in the fully discharged state of PVO60. Figure 4.10c displays the V 2p spectra from PVO60 at the pristine, charged, and discharged state. The V 2p spectrum of the charged PVO60 shows two peaks at 517.30 and 524.41 eV corresponding to V^{5+} and a peak at 515.93 eV corresponding to V^{4+}. When the PVO60 is fully discharged to -0.5 V (all potentials against Ag/AgCl), two sharp peaks at 515.80 and 523.69 eV are detected in the V 2p spectrum which correspond to V^{4+}. More V^{5+} is reduced to V^{4+} when more NH_4^+ ions are intercalated; hence, the amount of V^{5+} decreases and that of V^{4+} increases during the intercalation process.

The XPS results are complimented with Raman spectroscopic study of the PVO60 electrode. Figure 4.10d summarizes the Raman spectra of PVO60 at the pristine, charge and discharged state. In the spectrum of the discharged PVO60, there are a slight shift of the peak and a new peak located at 890 cm^{-1} compared to that of the pristine PVO60, confirming NH_4^+ forming hydrogen bonds (V=O$\cdots$H) with the PVO60 electrode.[127, 128] The XPS and Raman spectroscopy results demonstrate that hydrogen bonding plays a crucial role in the NH_4^+ redox chemistry. When NH_4^+ ions are intercalated by the layered PVO60, NH_4^+ ion as a tetrahedron-shaped multipole can rotate to move within the interlayer, breaking the hydrogen bonds with oxygen and nitrogen in PANI and forming new hydrogen bonds during moving. As hydrogen bonds are more flexible than rigid covalent or ionic bonds involved in the intercalation/extraction processes in metal-ion batteries, this process in ammonium-ion batteries allows more NH_4^+ ions to move and break/form bonds within the layered structure of PVO60 and thus accommodate more NH_4^+ ions, leading to high capacity and fast redox chemical reactions.

It is noted that the PVO60 in this work delivers a specific capacity of 192.50 and 120 mA h g^{-1} at 1 and 5 A g^{-1} respectively, which are higher than those reported in literature for pure PANI or pure V_2O_5. For instance, an earlier publication from our group reports PANI exhibits an ammonium-ion storage capacity of 160 and 110 mA h g^{-1} at 1 and 5 A g^{-1}, respectively. Dong et al. reports a capacity of 80 and 72 mA h g^{-1} at 1 and 5 A g^{-1} respectively for pure V_2O_5 annealed at 300°C.[100] These results show that the strategy of increasing the interlayer spacing with pure PANI in V_2O_5 framework can increase the capacity of pure PANI by 20% and notably by 59% increase with respect to pure V_2O_5 reported previously.

4.4 Conclusion

In this work, we employ an in-situ intercalation approach to prepare PANI-intercalated V_2O_5 to improve the NH_4^+ kinetics in ammonium ion batteries. The resulted electrode material, composed of a monolayer of PANI in the bi-layered V_2O_5 to expand its interlayer spacing and diffusion channels, shows a nanoflower morphology with larger surface area than the original parent structure, thereby accommodating more NH_4^+ ions and resulting in better electrochemical performance. The easy synthesis of the PVO electrode allows facile tuning of the composition of the PVO to maximize the transport kinetics and the battery performance. It is found that the PVO60 delivers the best electrochemical property, showing a capacity of 192.5 mA hg^{-1} and 39 mA hg^{-1} at specific currents of 1 and 20 A g^{-1} respectively as well as excellent cycling stability with a capacity retention of 98% over 100 cycles at either 10 or 20 A g^{-1}. Additionally, the ammonium-ion transport kinetics and intercalation mechanism in the AIB based on PVO60 are explored via XRD, XPS and Raman spectroscopy. It is found that the formation/breaking of hydrogen bonds occurs during the NH_4^+ (de)intercalation process within the layered structure of PVO60, and thus the hydrogen bonding dominates the NH_4^+ redox chemistry. As such, this work sheds light on the design and synthesis of high-capacity electrode materials to boost the electrochemical performance of emerging ammonium-ion batteries with intrinsic safety and low cost.

Chapter 5. A Metal-free All-Organic Ammonium-ion Battery with Low-Temperature Applications

5.1 Introduction

Batteries manufactured from metallic elements such as Ni, Co, Li, have been termed the new "petroleum" due to the imminent scarcity of these metallic elements. The dependence on metallic elements also causes environmental concerns due to toxicity of some metals and lack of sustainability.[129] On the other hand, non-metal charge carriers make it possible to fabricate safer and more sustainable metal-free batteries by combining with organic electrodes. Compared to traditional inorganic electrodes, organic electrodes have recently attracted much attention owing to their tunable molecular structure, metal-free feature, and lightness. They can be particularly useful for AIBs, because their flexible molecular structure could accommodate large ionic size of ammonium ions. Redox-active organic materials (ROMs), with organic groups from C, O, N and S have emerged as electroactive materials due to their abundance and light weight. They can be classified into three different categories depending on their charge storage mechanisms, i.e., p, n, and bipolar.[130, 131, 132, 133] P-type ROM has a charge storage mechanism in which oxidation occurs on the positively charged state (P^+), losing an electron, and the charge will then be balanced by an anion. N-type ROM (N) gets reduced by accepting an electron resulting in the negatively charged group and a counter positive cation balances this charge. In a bipolar type, a combination of both storage mechanisms of p and n types occurs.

Recently, a metal-free NH_4^+ dual-ion battery has been reported by using a graphite cathode and a 3,4,9,10-perylenetetracarboxylic anode, which exhibits an energy density of 200 Wh kg^{-1} when cycled in an organic electrolyte with NH_4PF_6 dissolved in the hybrid solvents of adiponitrile and ethyl methyl carbonate.[134] Though a potential high voltage of 2.75 V is shown in this proof-of-concept work, the battery is cycled in a much narrower potential range and presents moderate capacities. Additionally, both the electrode and the electrolyte materials used in this work are quite expensive. Among various organic electrodes, Polypyrrole (PPy) and polyaniline (PANI) have been used as electrodes in metal ion batteries,[135, 136, 137, 138] as they can be oxidized with anions through doping increasing their electrical conductivity. Polarons and bipolaron formed on the conjugated backbones upon p type doping process, increase their energy levels and conductivity. Both these polymers offer advantages of facile synthesis. Our group made the first effort to demonstrate PANI as a promising host material for NH_4^+ ion storage, recording a capacity of 160 mAh g^{-1} at 1 A g^{-1}.[139] We also prepared V_2O_5 intercalated with PANI for NH_4^+ ion

This chapter previously appeared as: Kuchena, Shelton Farai, and Ying Wang. "A metal-free all-organic ammonium-ion battery with low-temperature applications." *Journal of Materials Chemistry A* (2023). Copyright 2023 Royal Society of Chemistry. https: //pubs.rsc.org/en/content/articlehtml/2022/oq/d2ta08988b

storage, which delivers an increased capacity of 195.5 mAh g^{-1} at 1 A g^{-1}.[140, 141] Nevertheless, PPy has never been tested for ammonium-ion storage so far.

In this work, a metal-free ammonium-ion battery is developed using PPy and PANI electrodes coupled with WiSE. PPy is tested as a host material for NH_4^+ and K^+ ion, as they have similar physical properties, i.e., same coordination number (CN) of 6, ionic radius of 1.38 Å for K^+ vs. ionic radius of 1.48 Å. Additionally, water in salt electrolyte (WiSE) is employed to improve the performance of the batteries, as WiSE offers better properties than conventional electrolytes, including expanded electrochemical window, inhibited parasitic side reactions, and suppressed metal dissolution. Another advantage provided by WiSE is a lower freezing point due to fewer free water molecules in WiSE compared to conventional diluted electrolytes, which makes it possible to develop batteries that can operate at subzero temperatures. Herein, we investigate K^+/ NH_4^+ ion insertion in ROM PPy using 25 M and 1 M electrolytes of KAc or NH_4Ac. Additionally, this work is the first effort to fabricate a nonmetal full battery that can operate at a low temperature of 0°C, by using ROM PPy cathode, PANI anode, and 19 m NH_4Ac electrolyte.

Herein, we present an all-organic metal-free NH_4^+ ion full battery that can operate at a low temperature of 0°C, by using polypyrrole (PPy) as cathode, polyaniline (PANI) as anode, and 19 m ammonium acetate aqueous solution as electrolyte. For the first time, PPy is demonstrated as a high-capacity host material for both NH_4^+ and K^+ storage, when cycled in the water in salt electrolytes (WiSEs). When tested in a three-electrode cell containing 25 m NH_4CH_3COO electrolyte, PPy exhibits an impressive capacity of 125 mA h g^{-1} at a specific current of 1 Ag^{-1} and retains 43.61 mA h g^{-1} at 25 A g^{-1}. Additionally, a full battery is assembled using PPy cathode and PANI anode coupled with 19 m NH_4CH_3COO WiSE. This battery is found to deliver a capacity of 78.405 mA h g^{-1} at 25°C and 49.083 mA h g^{-1} at 0°C with a capacity retention of 71.83% after 200 cycles, demonstrating its potential for operations at low temperatures. Additionally, the physiochemical properties of NH_4^+-based WiSEs are examined by Raman and Nuclear magnetic resonance (NMR) spectroscopies, to explore their electrochemical behaviors and the fundamental effect of salt concentration on the electrolyte characteristics. This study presents the first non-metal battery with potential for low-temperature applications and opens the door to future metal-free electronics that would generate long-term benefits to the environment.

5.2 Experimental Section

5.2.1 Synthesis of Polypyrrole

0.86 g Sodium Dodecyl Sulphate (SDS) as a surfactant was added to 30 ml de-ionized water, followed by vigorous stirring for 30 mins to obtain a clear solution. 3 ml pyrrole monomer was then added dropwise. Afterwards, $FeCl_3$ solution of the required molarity was added dropwise and allowed to polymerize for 3 hours at room temperature. A black solution was formed,

indicating successful polymerization. It was washed and filtered several times with de-ionized water. The polymer powder was dried in a vacuum oven at 60°C for 24 hours.

5.2.2 Synthesis of Polyaniline

PANI was synthesized by a chemical oxidation method. Typically, 0.365 mL aniline and 15 mL 1 m HCl were added in a beaker under stirring in an ice bath to maintain a low temperature range of 0 – 5 °C. After 1 h of continuous stirring, 5 mL of 1 m HCl with dissolved 0.228 g $(NH_4)_2S_2O_8$ (APS) as an oxidant was added into the mixture dropwise whilst under continuous stirring in the ice bath. After a few minutes, the colorless solution turned dark green, showing polymerization had occurred. After the reaction continued for 1 h, the solution was taken out and washed with deionized water, and PANI precipitates were collected then put in an oven for drying at 60°C for 12 h.

5.2.3 Material Characterization

X-Ray diffraction measurements were collected at rate of 2° min^{-1} using Rigaku MiniFlex XRD with Cu Kα radiation with wavelength 1.54Å. Scanning electron imaging and EDS mapping was done using FEI Quanta 3D FEG field emission scanning electron microscope. Raman data was collected using the Reinshaw in Via Reflex Raman Microscope and X-ray photoelectron spectroscopy (XPS) measurements were done using AXIS165 spectrometer. Bruker Avance Neo 700 MHz spectrometer was used for NMR characterization for the electrolyte in deuterium solvent.

5.2.4 Electrochemical Measurement

For the three-electrode cell measurements, the electrode was prepared by mixing the as-prepared PPy, carbon black and polyvinylidene fluoride (PVDF) binder at a weight ratio of 7:2:1 in dimethylformamide. The slurry was then cast onto the carbon fiber paper and dried at 60°C in an oven. The mass loading of the electrode is about 3 mg/cm^2. The electrochemical performance was tested in an three-electrode cell, in which the PPy electrode, graphite rod, and saturated Ag/AgCl, serve as the working electrode, counter electrode, and reference electrode, respectively. The electrolyte is 200 ml of 1 m or 25 m aqueous solution of NH_4Ac or KAc. Cyclic voltammetry (CV) measurements and galvanostatic charge- discharge (GCD) tests were conducted on an electrochemical workstation CHI 6504C (CH Instruments, Inc. Austin, TX) over a potential range of 0.5 – -1 V. Electrochemical impedance spectroscopy (EIS) measurements were operated by applying an AC potential of 5 mV amplitude in a frequency range from 0.01 to 100 kHz.

For the full PANI/PPy full aqueous batteries, a 2032 coin-type cell was assembled using PANI anode and PPy cathode coupled with the electrolyte (NH_4Ac or KAc) and separator. The

working electrodes, i.e., PANI and PPy, were fabricated by rolling 60 wt% active material, 30 wt% conductive carbon (Super P), and 10 wt% polytetrafluoroethylene (PTFE) into thin film. Galvanostatic charge-discharge experiments were carried out on an eight-channel battery analyzer (MTI corporation) with a voltage range of 0 - 1 V. Cyclic voltammetry measurements and electrochemical impedance spectroscopy was conducted on an electrochemical workstation (CHI 6504C) with a frequency range of 100 kHz to 0.01 Hz

5.3 Results and Discussion

PPy was prepared via a chemical oxidation method using anhydrous $FeCl_3$ as a chemical oxidant, as described in the Experimental Procedure in the Supporting Information. The yield and the conductivity of PPy produced is affected by solvent, type of oxidant, monomer/oxidant ratio, and reaction time. The optimum ratio of Fe (III) to monomer of 2.4 will result in the yield of PPy approaching 100%.[142] The overall reaction is represented by the following stochiometric reaction equation:

$$n\,C_4H_5N + (2+y)n FeCl_3 = [(C_4H_3N)_n^{y+}\, ny Cl^-] + (2+y)n FeCl_2 + 2n HCl \qquad \textit{Equation}\ldots.\ 1$$

where y is the degree of PPY oxidation.

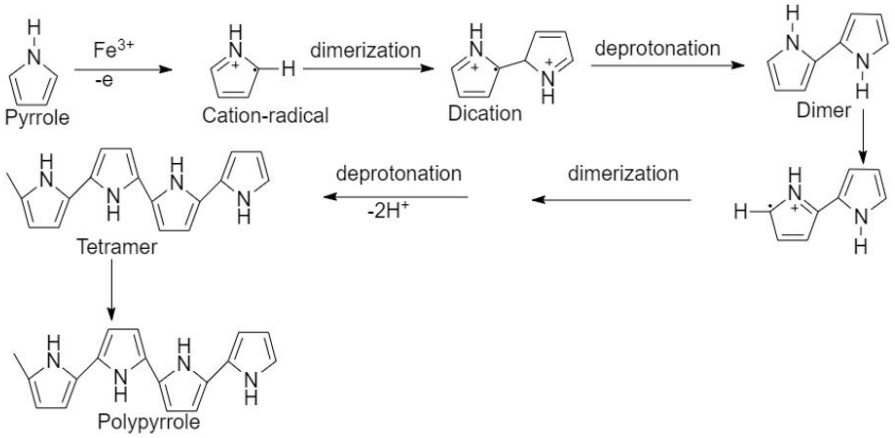

Scheme 1. Reactions for synthesizing PPy via chemical oxidation.

Scheme 1 presents the reaction formation of PPy polymer. $FeCl_3$ serves as the oxidant which produces active cation-radicals of the monomers while the reaction proceeds, resulting in a long-conjugated structure with C=C bonds and C-C bonds alternately arranged. An optimum ratio of the oxidant to the monomer is required. If the ratio is to high, more oxidant will be available, resulting in over polymerization. If the ratio is too low, the polymerization would not be completed, and more monomer units will be left in the solution.[143]

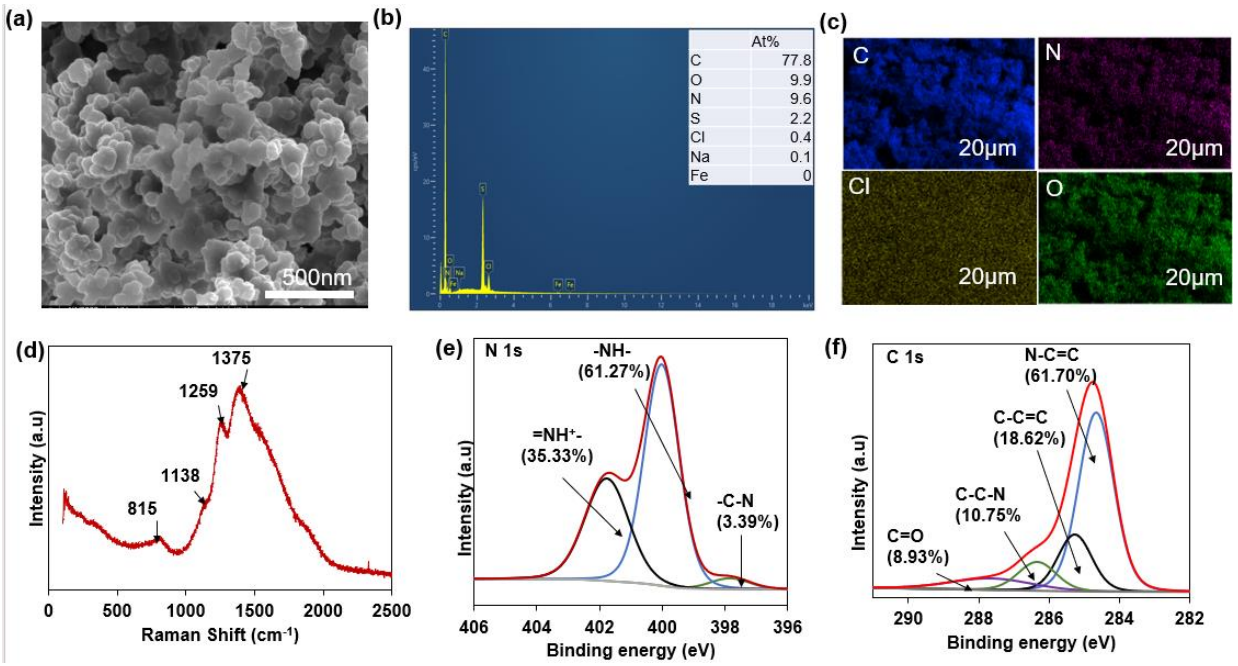

Figure 5.1.(a) SEM, (b) EDS spectrum, (c) EDS mapping, and (d) Raman spectrum, (e) XPS N 1s spectrum, and (f) XPS C 1s spectrum of PPY

The as-prepared PPy is then characterized for composition, structure, and morphology, as revealed in Figure 5.1. Figure 5.1a shows the SEM image of PPy, displaying a highly porous nano-thorn structure which is beneficial to electrochemical redox reactions as it provides high surface area and short diffusion paths. Figure 5.1b presents the EDS spectrum of PPy, showing its elemental composition with C- 77.8% O-9.9%, N-9.6%, confirming the successful synthesis of PPy. The EDS mapping in Figure 5.1c suggests homogenous distribution of C, N, O and Cl in the entire sample, indicating a uniform composition of PPy. Figure 5.1d displays the Raman spectrum of PPy, with the bands at 815 and 1138 cm^{-1} assigned to the ring formation associated with the di cation (di-polaron and radical cation (polaron), the peak at 1375 cm^{-1} attributed to the C-N stretching mode and that at 1259cm^{-1} is the C-H group, again demonstrating the successful synthesis of PPY.[144] Figure 5.1e unveils the N 1s XPS spectrum of PPy that shows nitrogen groups at 400.03, 401.77 and 397.75 eV corresponding to -NH- at an atomic weight percentage of 61.27% , $-NH^{+}-$ with 35.33%, and -C-N 3.39% respectively.[145] The presence of $FeCl_3$ during synthesis would result in polarons and bipolaron that have a delocalized spin which is responsible for the conductivity of PPY. Additionally, Figure 5.1f presents the C1s XPS spectrum revealing peaks at 284.5 eV, 285.1, 286.5, and 287.7 eV, representing N-C=C, C-C-C, N-C-C- and -C=O- groups in PPy. [146]

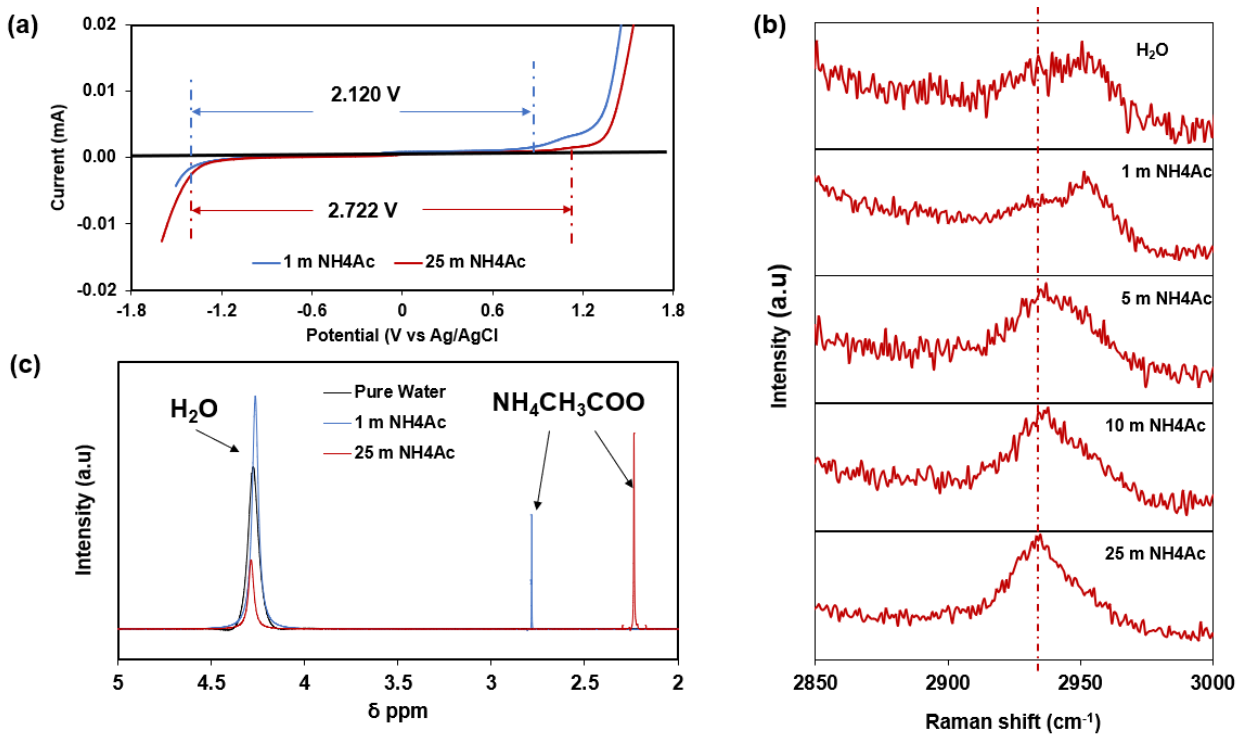

Figure 5.2. (a) Linear Sweep Voltammetry curves recorded in 1 m and 25 m NH_4Ac electrolytes at 10 mV s^{-1}. The onset potentials are selected at 0.001 mA. (b) The Raman bonds observed in the range of 2900 to 3000 cm^{-1} which correspond to the O-H stretching modes of water. (c) Normalized NMR spectra of 1 m and 25 m NH_4Ac electrolytes as well as pure water, showing the ^1H chemical shift of water molecules and protons in NH_4Ac.

To explore physiochemical properties of the electrolytes with various concentrations, we perform linear sweep voltammetry (LSV) as well as Raman and ^1H NMR spectra characterizations. First, LSV is carried out to determine the potential window of the aqueous ammonium-ion electrolytes, as presented in Figure 5.2a. It is found that the 25 m NH_4Ac electrolyte shows a potential window of 2.722 V, wider than 2.120 V from the 1 m NH_4Ac electrolyte. The expanded voltage window is attributed to the anodic stability property, though the electrolyte concentration has insignificant effect on the water cathodic stability.[147,148] In order to understand the interaction between the ammonium acetate salt and water, Raman spectroscopy is performed on the electrolytes with concentration varying from 1 to 25 m NH_4Ac as displayed in Figure 5.2b. The O-H stretching vibration peaks reveal that the spectrum of WiSE resembles that of crystalline salt with no water molecules, while a broad Raman band is observed for pure water, due to water molecules in different hydrogen bonding environments in water clusters.[149] This band remains pronounced in the electrolyte of 1 m NH_4Ac, indicating that water molecules remain clusters and do not participate that much in the hydration structure around NH_4^+ ions. As the salt concentration increases to 25 m, it is observed that a sharp peak progressively forms at 2934.988 cm^{-1} at the expense of the broad water cluster band, suggesting that number of free water clusters decreases significantly and the vast majority of water molecules are in a state of crystalline hydrates.[149] These results illustrate that less water content available for the formation of the solvation sheath the

sharper the peak becomes. The position of the peak also depends on the salt, e.g., 3552 cm^{-1} for 17 m $NaClO_4$,[150] 3429 cm^{-1} for 40 m HCOOK.[151]

To further explore the interactions between ions and water molecules as well as the hydrogen bonding in the electrolytes, proton NMR studies are performed on the 1 m and 25 m NH_4Ac electrolytes in addition to pure water as a reference, as revealed in Figure 5.2c. The downward chemical shift from 2.783 to 2.236 ppm for the ^1H spectra from NH_4CH_3COO is due to the increase in concentration as the interaction between NH_4Ac ions and water molecules increases.[152] NH_4^+ ion is multipolar and can form hydrogen bonds in aqueous solution, entailing a redox chemistry different from ionic bonding formed by metallic charge carriers. The formation of hydrogen bonds is more pronounced at higher concentrations of salt, due to the increase of interaction between the cations and water molecules, leading to the shift in the ^1H NMR spectra. It is noted that the interaction between NH_4^+ ion and oxygen in water is much stronger with a larger binding energy of 0.89 eV than that between two water molecules (0.27 eV). In this regard, more hydrogen bonds are formed between NH_4^+ ions and -OH (in water) in the high-concentration electrolyte containing fewer free water molecules. In high-concentration electrolyte, significant ion-pairing and aggregation occur while a limited number of solvent molecules will be largely bound to cations, leading to new electrolyte structures at both molecular and long-range scales that would affect properties such as transport, thermal, mechanical, electrochemical, interfacial, and interspatial. In a diluted solution, cations exist as hydrated ions bound by water molecules. However, there are more cations than water molecules in the WiSE, hence, the primary solvation sheath of a cation is not complete, resulting in fewer water molecules available for the formation of the primary solvation sheath of the ion. The reduced solvation number decreases the highest occupied molecular orbital (HOMO) level of water, making water splitting reactions more difficult, especially the oxygen evolution reaction (OER). Additionally, fewer free water molecules would cause suppressed freezing point of the aqueous electrolyte.[153]

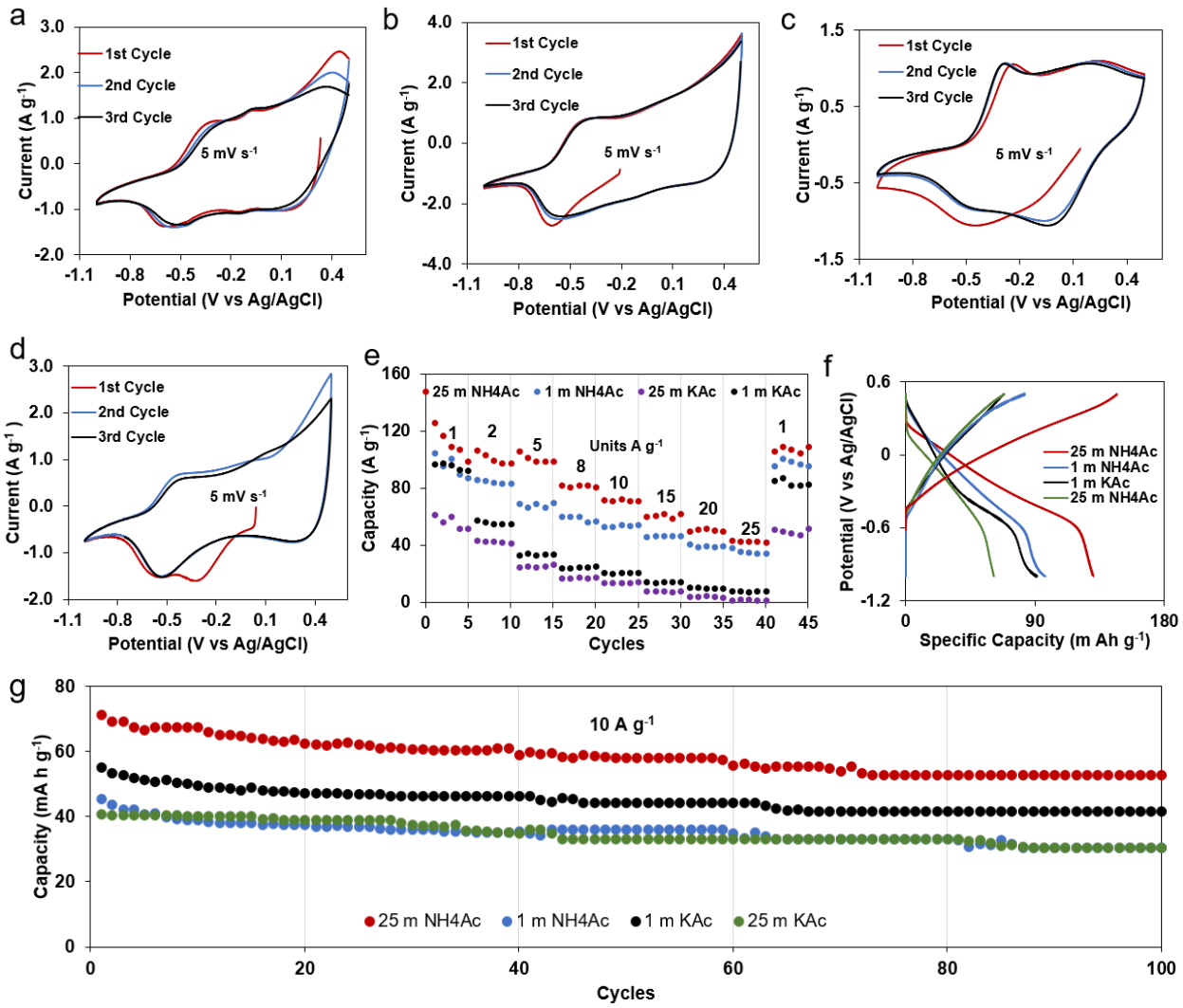

Figure 5.3. The first three CV curves at a scan rate of 5 mV s^{-1} of PPy cycled in (a) 25 m NH_4Ac, (b) 1 m NH_4Ac, (c) 25 m KAc, (d) 1 m KAc. (e) Rate performances, (f) charge/discharge curves of initial cycles at 1 A g^{-1}, and (g) cycling performances at 10 A g^{-1} of PPy in 1 M and 25 M of NH_4Ac and KAc electrolytes.

In this work, NH_4^+ and K^+ ions are compared as charge carriers for battery performance evaluation, since these two ions have similar physical properties, such as the same coordination number (CN) = 6 and ionic radius of 1.38 Å for K^+ vs. 1.48 Å for NH_4^+. To study the intercalation behaviors of these two ions in the PPy electrode, a three-electrode cell is set up, using PPy as the working electrode, graphite as the counter electrode, Ag/AgCl as the reference electrode in 1m or 25 m electrolyte. Figure 5.3 a-d present the cyclic voltammogram (CV) curves of the battery cells using 25 m and 1 m NH_4Ac and KAc electrolytes, respectively. The CV area from the cell using 25 m NH_4Ac electrolyte in Figure 5.3a appears larger than that from the 25-m-KAc-based cell in Figure 5.3c, suggesting PPy delivers higher NH_4^+-storage capacity than K^+ storage capacity. Figure 5.3a displays the first three CV curves for PPy in 25 m NH_4Ac in a voltage range of -1 V to 0.5 V. The cathodic peaks, located at -0.541, -0.136 and 0.168 V, are observed during the initial

reduction scan, which overlap well with the three peaks in the following cycles of the cathodic scan. The oxidation peaks located at -0.303, -0.06 and 0.456 V also overlap well in the first three CV curves. Multiple oxidation-reduction pairs of peaks are clearly observed, suggesting a multistep reaction process of NH_4^+ ions with the PPy electrode. Furthermore, the CV profiles of the three initial cycles show good repeatability, indicating good redox reversibility and structural stability of the PPy electrode. These curves are slightly different from those of the PPy for K^+ storage in the 25 m KAc electrolyte in Figure 5.3c which reveals cathodic peaks at -0.023 and -0.5 V as well as oxidation peaks at 0.227 and -0.272 V. The CV profiles of PPy for K^+ storage also show good repeatability, suggesting good reversibility. The CVs for K^+ and NH_4^+ storage in PPy display clear redox peak pairs, demonstrating the capability of PPy in stable and reversible electrochemical storage of both K^+ and NH_4^+ ions. In contrast, the CV for NH_4^+ intercalation shows an additional redox peak pair compared to that for K^+, attributed to a different multistep reaction process. NH_4^+ ion exhibits a structure composed of four flexible hydrogen atoms which make it multipolar and can form hydrogen bonds with host structure. Hence, NH_4^+ ion entails a different redox chemistry from metallic K^+ ion that forms rigid ionic bond with host. It is important to note that the desolvation process in aqueous electrolyte requires low energy for NH_4^+ ions than for K^+ ions, because NH_4^+ ion forms hydrogen bonding with water molecules which is weaker than ionic bonding formed by K^+ ions.[154] Figure 5.3 b and c shows the first three CV curves of the PPy electrode in 1 m aqueous electrolyte with NH_4Ac or KAc, respectively. In the 1 m NH_4Ac, the CV of PPy reveals an anodic peak at -0.60 V and a cathodic peak at -0.39 V which have different peak positions than those in the CV from the 1 m KAc electrolyte with anodic peaks at -0.526 and 0.295 V and cathodic peak at -0.429 V. For both NH_4^+ and K^+ storage, the peaks on the CV curves of PPy from the 1 m electrolyte are fewer and less sharp than those from the 25 m electrolyte, due to different intercalation mechanisms in the electrolytes of different concentrations. It is also observed that the CV curves from the 25 m electrolytes exhibit higher integrated area than those from the 1 m electrolyte, suggesting the battery cell based on WiSE may deliver higher specific capacity than that using diluted electrolyte.

It is important to evaluate the rate performance of aqueous ammonium-ion batteries as it reflects the transport kinetics during charge and discharge of the battery. Unfortunately, various cathodes reported to date have shown unsatisfactory rate performances, owing to irreversible structural change in the electrode materials and intensive polarization of NH_4^+ ions with slow charge transfer kinetics. However, the as-prepared PPy delivers excellent rate capability when subjected to harsh galvanostatic tests at the specific current ranging from 1 to 25 A g^{-1} in a voltage window -1 to 0.5 V, as presented in Figure 5.3e. The PPy electrode shows the best performance for NH_4^+ storage in the 25 m NH_4Ac electrolyte among all the electrolytes of different charge carriers or concentrations, demonstrating reversible capacities of 125.77, 106.50, 101.67, 80.88, 72.11, 60.13, 50.22, and 43.61 mA h g^{-1} at specific currents of 1, 2, 5, 8, 10, 15, 20, 25 A g^{-1}, respectively. It is noted that there is only ~ 19.16% capacity decay as the applied specific current is increased from 1 to 5 A g^{-1}. After cycled at a high specific current of 25 A g^{-1} and back to 1 A g^{-1}, a capacity of 106.0 mA h g^{-1} is delivered, demonstrating excellent structural integrity of the PPy electrode. Additionally, a moderate capacity of 43.61 mA h g^{-1} and a discharge-charge time of

6.28 seconds, are delivered even at the highest specific current of 25 A g^{-1}, suggesting the ultrafast transport kinetics and impressive rate capability of the PPy electrode when cycled in the WiSE of ammonium ions. In the 1 m NH_4Ac electrolyte, the PPy electrode exhibits discharge capacities of 104.44, 85.60, 66.94, 60.2, 53.19, 45.96, 38.89 and 35.97 mA h g^{-1} at specific currents of 1, 2, 5, 8, 10, 15, 20, 25 A g^{-1}, which are lower than those from the 25 m NH_4Ac electrolyte, due to the increased redox potential of PPy when tested in WiSE where more capacity could be realized at the same lower cutoff potential. The same phenomenon was observed for titanic acid electrode in 25 m NH_4Ac.[153] On the other hand, PPy delivers a higher K^+-storage capacity in the 1 m electrolyte than that in the 25 m KAc electrolyte. The former shows capacities 97.22, 53.39, 33.33, 24.22, 20.22, 14.5, 10.61, and 7.88 mA h g^{-1} at specific currents of 1, 2, 5, 8, 10, 15, 20, 25 A g^{-1} respectively, while the latter exhibits capacities of 61.5, 42.83, 25.28, 17.10, 14.08, 7.85, 4.37, and 1.361 mA h g^{-1}, as unveiled in Figure 3f. It is found that the K^+-storage performance of the PPy electrode is comparable with other host materials reported for K^+ storage.[155, 156, 157]

Figure 5.3f exhibits the GCD curves of the PPy electrode in the different electrolytes, with the one for NH_4^+ storage showing a smooth sloping profile and that for K^+ storage containing a pronounced step or plateau. The coulombic efficiencies (CEs) calculated from Figure 5.3f are 89.18 and 84.60% for PPy cycled in 25 and 1 m NH_4Ac, respectively, while CEs of PPy in 25 and 1 m KAc are 71% and 106%, respectively. The cycling performance of PPy in 25 and 1 m electrolytes of NH_4Ac and KAc are then examined at a high specific current of 10 A g^{-1}, as displayed in Fig. 3g. The PPy cycled in 25 m NH_4Ac shows the highest initial capacity of 71.55 mA h g^{-1} and a capacity retention of 73.77% after 100 cycles, whereas PPy in 1 m NH_4Ac delivers an initial capacity of 55.33 mA h g^{-1} and a capacity retention of 69.80% after 100 cycles. On the other hand, PPy cycled in 1 m KAc exhibits an initial capacity of 43.78 mA h g^{-1} and a capacity retention of 69.80% after 100 cycles, while PPy in 25 m KAc gives an initial capacity of 40.78 mA h g^{-1} and a capacity retention of 74.94% after 100 cycles. PPy demonstrates decent cycling stability for both NH_4^+ and K^+ storage in different electrolyte concentrations.

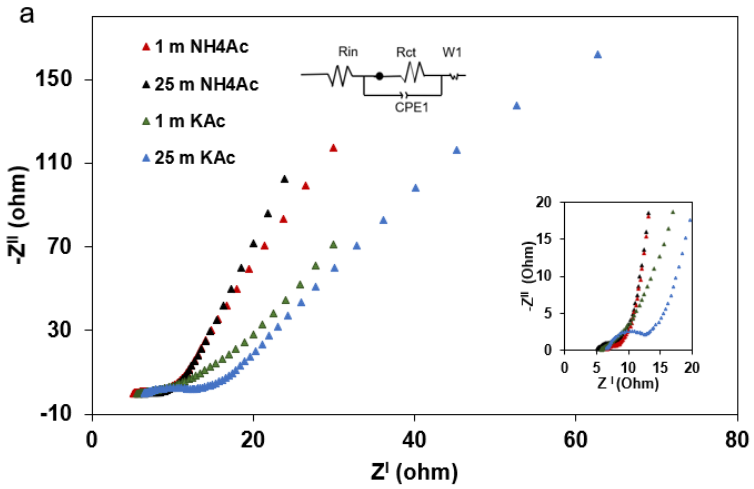

Figure 5.4. Electronic Impedance Spectroscopy spectra of the PPy electrode in 1 m NH_4Ac, 25 m NH_4Ac, 1 m KAc, and 25 m KAc electrolytes.

To elucidate the charge transfer process, electrochemical impedance spectroscopy (EIS) tests are then carried out in PPy when cycled in NH_4Ac and KAc electrolytes, as presented in Figure 5.4. The charge transfer resistances of PPy in the 1 and 25 m NH_4Ac electrolytes are 8.31 and 9.28 Ω respectively, while those in 1 and 25 m KAc electrolytes are 10.23 and 14.43 Ω, respectively. The charge transfer resistances of PPy in the 25 m electrolytes are higher than those in the 1 m electrolytes, possibly due to enhanced ion-ion interactions in WiSE. On another note, PPy in KAc electrolytes exhibits higher charge transfer resistances than in NH_4Ac at both concentrations, because K^+ ions form rigid ionic bonds with water whereas NH_4^+ ions form weaker flexible hydrogen bonds with water which can break and form more easily during charge transport.[158] This effect of strong coordination ability causing slower kinetics in KAc electrolyte is enhanced at higher concentrations, as more K^+ ions form ionic bonds with water leading to higher interfacial resistance at the electrode/electrolyte interface. Hence, in addition to electrolyte structure, the electrode/electrolyte interfacial property affects the charge transfer kinetics too.

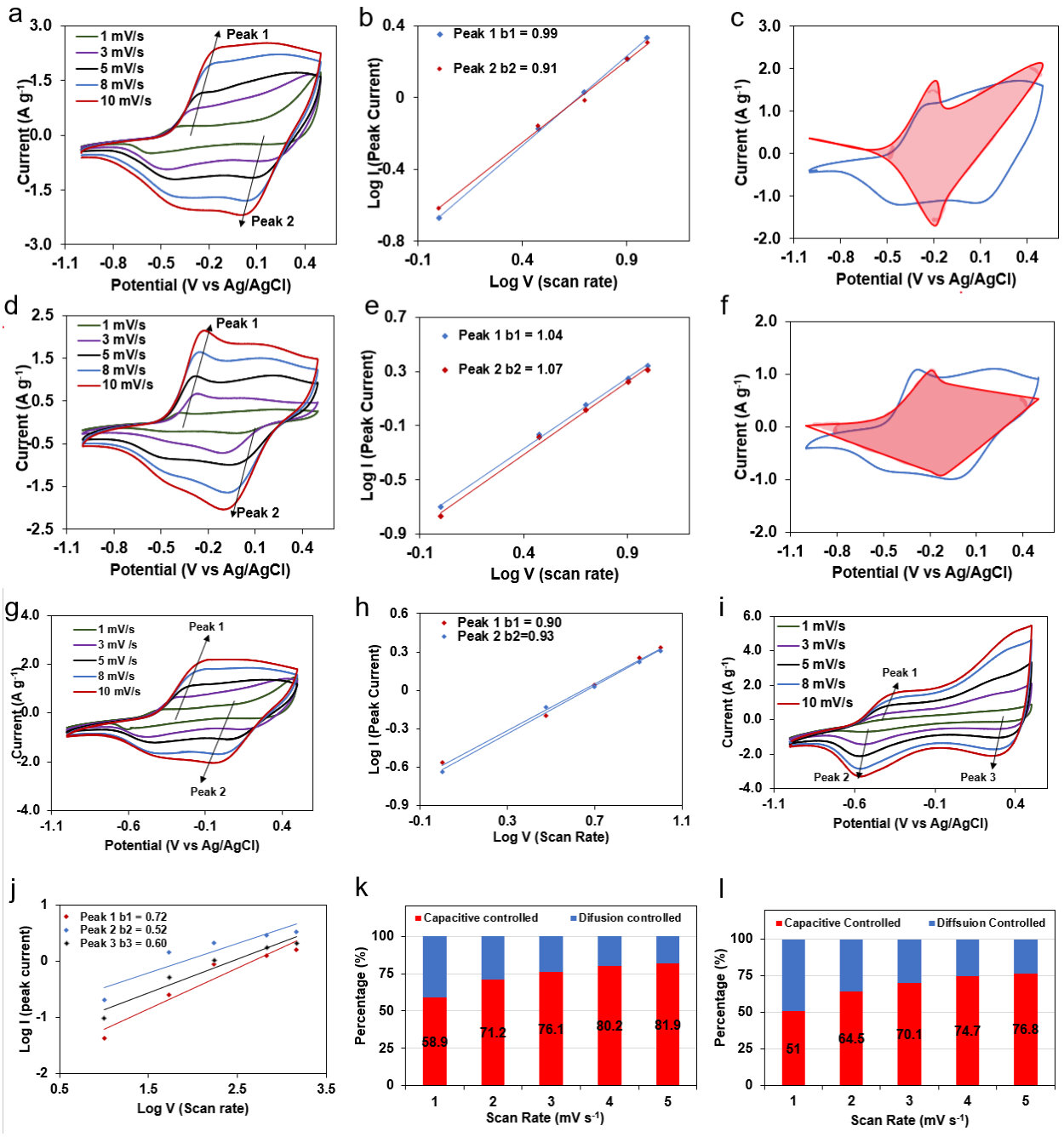

Figure 5.5. Electrochemical tests of PPy in 25 m NH_4Ac electrolyte: (a) CV profiles at various scan rates, (b) Log i (peak current) vs. Log v (scan rate) based on the CV data in a, (c) CV showing the capacitive contribution at 5 mV s^{-1}. Electrochemical tests of PPY in 25 m KAc: (d) CV profiles at various scan rates, (e) Log i (current) versus Log v (scan rate) based on the CV data in d, (f) CV showing the capacitive contribution at 5 mV s^{-1} (g) The CV profiles of PPy in 1 m NH_4Ac at various scan rates; (h) Log i (current) versus Log v (scan rate) at specific reduction/oxidation states based on the CV data in (g); (i) CV profiles of PPy in 1 m KAc at various scan rates; (j) Log i (current) versus Log v (scan rate) at specific reduction/oxidation states based on the CV data in (i) The contribution ratio of the diffusion-controlled capacities and capacitive capacities for PPy in (k) 25 m NH_4Ac electrolyte, (l) 25 m KAc electrolyte.

To further study kinetics in PPy for storage of K^+ and NH_4^+ ions, more CV tests are performed in 25 m electrolytes, as shown in Figure 5.5. Figure 5.5a and d present the CV profiles of the PPy electrode in the 25 m NH_4Ac and KAc respectively at sweep rates in a range of 1-10 mV s^{-1}. It is found that the CV profiles maintain similar shapes with the area getting larger with the increasing scan rate, indicating excellent electrochemical properties of PPy during the redox reactions with NH_4^+ and K^+ ions even in the 1 m electrolytes as presented in Figure 5.5 g and i. The cathodic and anodic peaks appear to shift to low and high potentials at the increased scan rate, respectively, which can be attributed to the diffusion resistance is increased when the scan rate increases. The power law can be used to analyze the electrochemical kinetics, as described below: $i = av^b$ where a and b are constants, v is the scan rates (in V/s), i is the current (in A). b values represent the type of electrochemical charge storage reaction and range between 0.5 – 1.0. If b value is close to 0.5, the reaction is a diffusion-controlled process, while b value being close to 1 indicates a capacitive process. Figure 5.5b shows the b values to be 0.99 and 0.91, suggesting that the reaction is controlled by a capacitive process for NH_4^+. The same can be said about K^+ as revealed in Figure 5.5e with the b values being 1.04 and 1.07. When cycled in the 1 m electrolytes, the b values for NH_4^+ are 0.90 and 0.93, showing that the reaction is capacitive controlled at even lower electrolyte concentrations (Figure 5.5h). It is different for PPY cycled in 1 M KAc electrolyte, because the b values are 0.72, 0.52 and 0.60 as revealed in Figure 5.5j, indicating the reaction is mainly diffusion controlled.

Furthermore, the equation $i = av^b$ can be separated into capacitive (k_1v) and diffusion ($k_2v^{1/2}$) factors to quantify their contributions:

$i = k_1v + k_2v^{1/2}$ with k_1 representing capacitive and k_2 diffusion contributions.

Figure 5.5c unveils the capacitive contribution when PPy is cycled in 25 m NH_4Ac at 5 mV/s. From Figure 5.5k 76.1% at 5 mV/s is from capacitive contribution. Additionally, it can also the observed from Figure 5.4k that as the scan rate increases i.e., 1, 3, 5, 8 and 10 mV s^{-1} the capacitive process dominates the contribution towards total capacity with contributions 58.9, 71.2, 76.1, 80.2, and 81.9% respectively. The same can also be said for K^+ from Figure 5.5l the distribution for capacitive controlled at 5 mV s^{-1}. Additionally, it can also the observed from Figure 4h that as the scan rate increases i.e., 1, 3, 5, 8 and 10 mV s^{-1} the capacitive process dominates the contribution towards total capacity with contributions 51, 64.5, 70.1, 74.7, and 76.8% respectively.

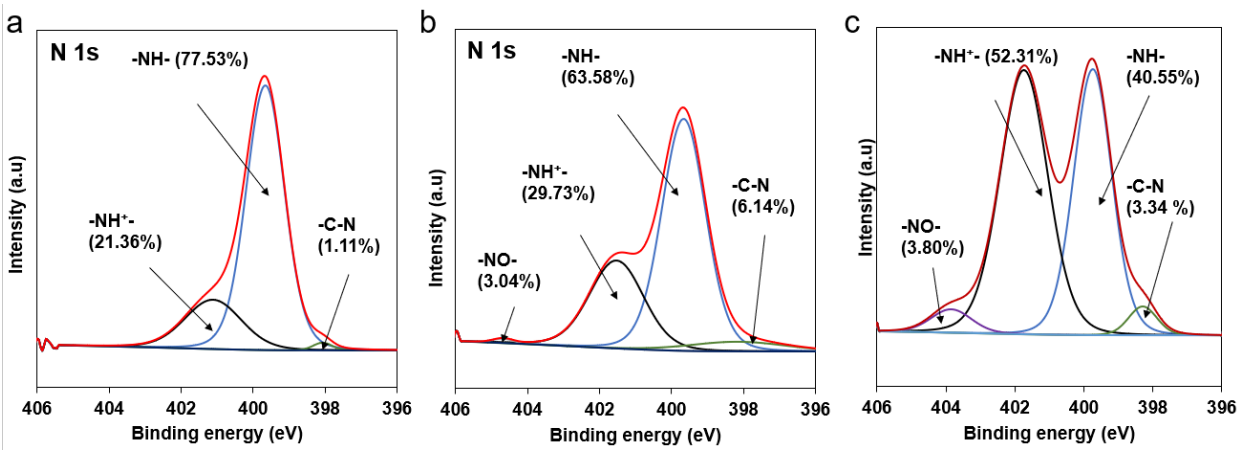

Figure 5.6. Ex-situ XPS N 1s spectrum of PPy at (a) pristine, (b) charge, (c) discharge state, when cycled in 25 m NH_4Ac.

To gain more insights in the storage mechanism of NH_4^+ ions in PPy, we conducted ex-situ XPS spectroscopy on N 1s from the PPy electrode, since the electrochemical properties of PPy are dependent on the oxidation state of N. The study is focused on the PPy electrode cycled in 25 m NH_4Ac electrolyte, since it delivers the highest capacities among the battery cells using various electrolytes. Figure 5.6 displays the N 1s XPS spectra of PPy at pristine, charge, and discharge states. As shown in Figure 5.6a, the spectrum of pristine PPy reveals N 1s groups at 399.76, 398.07 and 401.11 eV, corresponding to N from -NH- (77.53%), -CN- (1.11%), and -NH^+- (21.36%) (The value in the bracket is atomic percentage.). In the XPS spectrum of the charged PPy after five cycles in Figure 5.6b, the positions of N 1s peaks do not change, locating at 399.66, 398.17, 401.53 and 404.68 eV, which represent non-protonated amine -NH- (63.58%), -NC- (6.14%), protonated amine -NH^+- (29.73%) and -NO- (3.04%) nitrogen groups that are similar to the pristine state. Compared to the spectrum of the discharged PPy in Figure 5.6c, the atomic weight percentage of -NH^+- increases from 29.73% in the charged state of PPy to 52.31% in its discharged state. As for -NH- group, it decreases from 63.58% in the charged PPy to 40.55% in the discharged PPY, resulted from the oxidation of PPy by NH_4^+ ions. As discharge continues and the potential on the electrode would increase in the negative charges, more NH_4^+ ions would be further attracted to the electrode and facilitate protonation of the -NH- group. The reverse process occurs during charging over a single potential range.

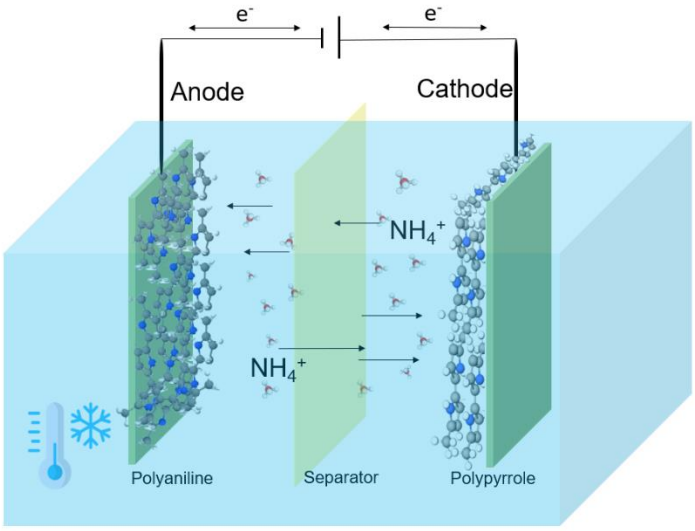

Figure 5.7. Schematic of the metal-free ammonium-ion full battery based on PPY/PANI electrodes.

Due to the promising electrochemical performance of PPy in high-concentration NH_4Ac electrolyte, we then fabricate the first all-organic metal-free battery and test it at 25°C and 0°C.

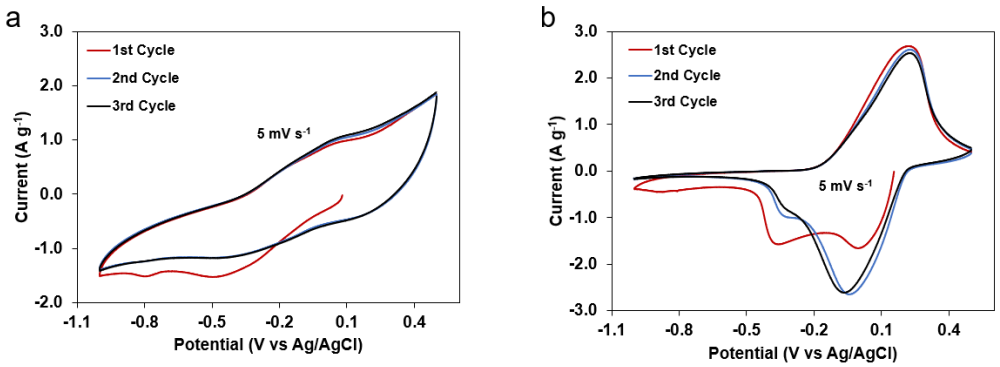

Figure 5.8. Cyclic voltammetry curves of (a) PPy and (b) PANI in the three-electrode set-up with 25 m NH4Ac electrolyte at a scan rate of 5 mV s -1 at 0 °C

Figure 5.8 exhibits CV curves of PPy and PANI in the three-electrode cell using 25 m NH_4Ac electrolyte in the voltage range 0.5 V to -1.0 V at 0°C, to determine if any redox reaction occurs in these electrodes at such a low temperature. Figure 5.8a displays the first three CV curves of PPy electrode, exhibiting cathodic peaks at 0.1 V and -0.2 V during initial reduction scan. The oxidation peak at 0.05 V is observed too, which shows that PPy maintains its electrochemical activity even at 0 °C. On other hand, PANI electrode exhibits one major oxidation peak at 0.257 V and one reduction peak at -0.031 V. Both initial CV profiles of PPy and PANI display good repeatability, indicating good redox reversibility and structural stability at 0°C. Encouraged by these results we assembled a full battery using PANI as anode and PPy as cathode in the mass ratio

of 1:1, as shown in Figure 5.7. Aqueous NH_4Ac electrolytes of various concentrations have been studied and it was found that the 19 m NH_4Ac electrolyte has a lowest freezing point of -38°C.[159] Therefore, we prepare and compare full batteries using 19 m and 25 m NH_4Ac electrolytes.

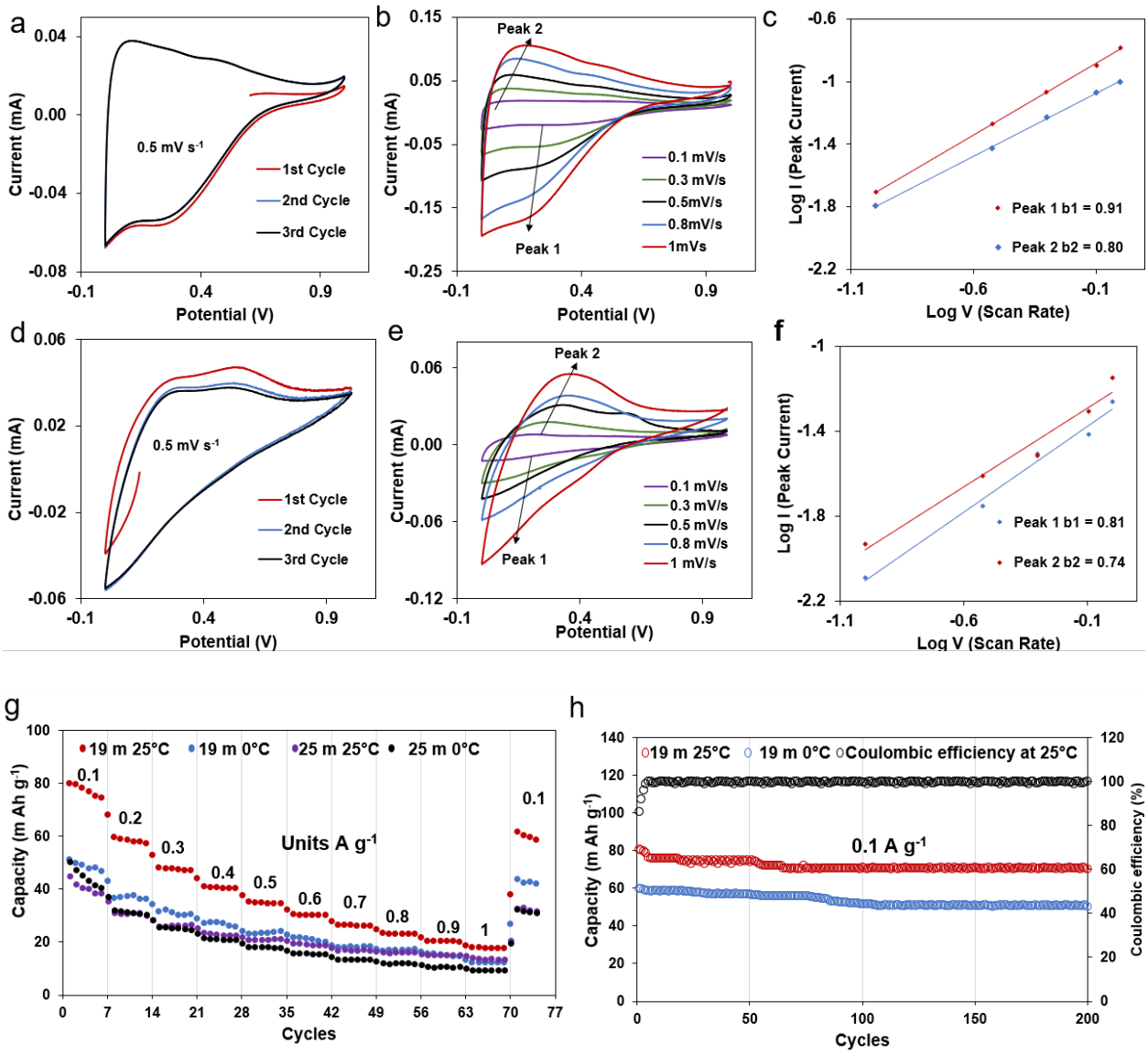

Figure 5.9. Electrochemical performances of the full PANI/PPy AIB with 19 m NH_4Ac in the potential range of 0 – 1 V: (a) the first three CV curves at 0.5 mV s^{-1} at 25°C, (b) CV curves are various scan rates, (c) Log i (current) versus Log v (scan rate) at specific reduction/oxidation states based on the CV data in b, (d) the first three CV curves at 0.5 mV s^{-1} at 0°C, (e) CV curves at various scan rates at 0°C, (f) Log i (current) versus Log v (scan rate) at specific reduction/oxidation states based on the CV data in e. (g) Rate capability of PANI/PPy cells with 19 m and 25 m NH_4Ac electrolyte at 25°C and 0°C. (h) Cycling performances of PANI/PPy cell with 19 m NH_4Ac electrolyte at 25°C and 0°C.

Figure 5.9a displays the first three CV curves of the PANI/PPy full cell with 19 m NH_4Ac electrolyte at 25°C, revealing one pair of pronounced redox peaks at 0.085 V and 0.275 V, in the potential range of 0 – 1 V. No peak shift is observed when comparing these three CV profiles, demonstrating a reversible and stable redox reaction during charging, and discharging of this full battery. To understand the kinetics of this full cell, we obtained its CV profiles are various scan rates ranging from 0.1 to 1 mV s^{-1}, as shown in Figure 5.9b. These CV curves at different scan rates show similar shapes, indicating excellent structural integrity of the PANI and PPy electrodes. The power law based on the CV profiles in Figure 5.9b is then applied to distinguish capacitive and diffusion currents. The b values for peaks 1 and 2 are found to be 0.91 and 0.80, respectively, as shown in Figure 5.9c, suggesting that the electrochemical reactions in the full cell are controlled by both capacitive and diffusion-controlled processes. It is expected low temperature would affect the transport kinetics of charge carriers in electrolytes, thereby affecting conductivity and inevitably the performance of the full cell. Figure 5.9d presents the first three CV curves of the full cell at 0°C, presenting a pair of redox peaks at 0.563/0.0088V. The capacitive area of the CV curve at 25°C is greater than that at 0°C because the conductivity and transport kinetics of the electrolyte are reduced at lower temperature. The CV curves at various scan rates show great repeatability demonstrating that temperature is not affecting the redox peaks of either PPy or PANI as shown in Figure 5.9e. The power law shows that the b values for peak 1 and 2 are 0.81 and 0.74, showing the process is dominated by the combination of capacitive and diffusion contributions, as seen in Figure 5.9f.

To further explore the electrochemical performances of the full cells, the PANI/PPy full cell with 19 m or 25 m NH_4Ac electrolyte is subjected to harsh galvanostatic evaluation from 0.1 to 1 A g^{-1} in a potential window of 0 -1 V at 25°C and 0°C, as presented in Figure 5.9g. The PANI/PPy full cell containing 19 m NH_4Ac exhibits reversible capacities of 78.405 and 49.083 mA h g^{-1} at 25°C and 0°C, respectively. Additionally, the cell based on the 25 m electrolyte delivers capacities of 45.184 and 40.633 mA h g^{-1} at 25°C and 0°C, respectively. The cell with 19 m electrolyte shows a capacity of 18.958 mA h g^{-1} at 1 A g^{-1} at 0°C. Figure 5.9h unveils cycling performance of the cell with 19 m electrolytes cells, presenting a retention capacity of 86.72% and 71.83% at a specific current of 0.1 A g^{-1} at 25°C and 0°C.

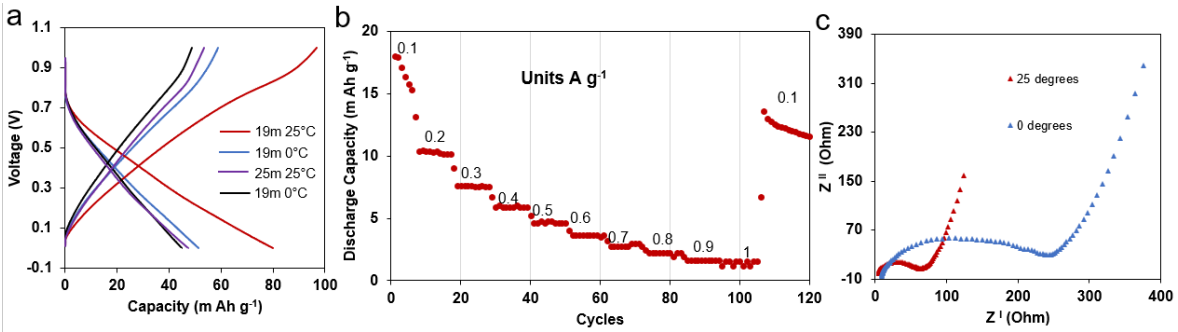

Figure 5.10. (a) Initial charge/discharge curves of PANI/PPy battery cells with 19 m and 25 m NH_4Ac electrolytes at 0 and 25°C, respectively, when cycled at 0.1 A g^{-1} (b) Rate performance of the full PANI/PPy cell with the 19 m KAc electrolyte (c) Electronic impedance spectroscopy spectra of the full PPy/PANI cell with the 19 m NH4Ac electrolyte at 25°C and 0°C

Figure 5.10a exhibits the GCD curves of the full PANI/PPy cell at 25°C and 0°C using 25 m and 19 m NH_4Ac electrolytes. The Coulombic efficiencies (CEs) calculated from Figure 5.10 are 120% and 115% for 19 m NH_4Ac electrolyte, as well as 113% and 108% for 25 m NH_4Ac electrolyte at 25°C and 0°C, respectively. The CEs are greater than 100%, which can be attributed to different storage capacities of PPy and PANI for NH_4^+ ions. NH_4^+ ion is a more promising charge carrier for the PANI/PPy full battery and is the focus of this work For comparison purposes, a PANI/PPy full cell is assembled using 19 m KAc electrolyte, which delivers a very inferior capacity of 17.951 mA h g^{-1} at 0.1 A g^{-1} at 25°C, as displayed in Figure 5.10b. Figure 5.10c exhibits EIS spectra of the PANI/PPy full cell with 19 m NH_4Ac electrolyte at 0°C and 25°C, showing the charge transfer resistance at 0°C is 280 Ω and that at 25°C is 88 Ω, confirming that the kinetics is slower at lower temperature, thereby smaller capacity when temperature decreases. During the discharge process, NH_4^+ ions will be stored in PPy through the mechanism described above; then NH_4^+ ions move back into the electrolyte during the charge process and will be stored in PANI via the mechanism reported by our group previously.[139,140] It can be seen that the capacity of our non-metal full battery is comparable to that delivered by the other all-organic ammonium dual-ion battery composed of graphite cathode and poly(1,5-naphthalenediamine) anode coupled with the electrolyte containing NH_4PF_6 dissolved in hybrid organic solvents reported recently,[160] however, the electrode and electrolyte materials in our work are more cost effective. Yan et al. have recently presented an ammonium-ion battery using Prussian blue cathode and WiSE with preliminary results showing the electrolyte can work over an extended temperature range of −40 to 80°C, but the battery is not tested for cycling performance at low temperatures.[161] Therefore, the PPy/PANI-based full battery in this work is the first one demonstrating low temperature applications among AIBs and metal-free batteries

5.4 Conclusion

In this work, we have developed the first all-organic metal-free battery that can operate at low temperature, by using PPY cathode and PANI anode as well as NH_4Ac WiSE. First, PPY is systematically studied as a host material for both NH_4^+ and K^+ storage in electrolytes with 25 M and 1 M concentrations. It is found that PPY delivers an impressive capacity of 125 mA h g^{-1} at a specific current of 1 Ag^{-1} and maintains 43.61 mA h g^{-1} at 25 A g^{-1}, when cycled in 25 M NH_4Ac electrolyte, much higher than 40.78 mA h g^{-1} at 1 A g^{-1} for K^+ storage when it is cycled in 25 M KAc electrolyte. The PPy cathode is then coupled with PANI anode together with 19 M NH_4CH_2COO electrolyte, to form a metal-free full cell that demonstrates a high capacity 78.405 mA h g^{-1} at 0.1 A g^{-1} at 25°C and a capacity of 49.083 mA h g^{-1} at 0°C. Additionally, the physiochemical properties of NH_4^+-based WiSEs are examined by Raman and Nuclear magnetic resonance (NMR) spectroscopies, to explore their electrochemical behaviors and the fundamental effect of salt concentration on the electrolyte characteristics. This work presents new opportunities for the fabrication of all-organic batteries with lower cost, better safety and sustainability. Such a battery also opens the door to future realization of metal-free electronics that would generate long-term benefits to the environment.

Chapter 6. Conclusions

In this research work the development of high-performance ammonium ion batteries (AIBs) was achieved by improving their electrochemical performance. This was done from two aspect i.e., developing high-capacity storage nanomaterials which can be applied as electrodes in ammonium ion full cells and electrolytes which are facially tuned and optimized to enable the ammonium battery to be used in different applications i.e. in flexible electronics and use in low temperatures.

For a battery to deliver high power and energy electrodes play a crucial role so a high-capacity cathode material is necessary. We proposed a high-surface-area emeraldine salt polyaniline (ES-PANI) and emeraldine base polyaniline (EB-PANI) with a nano thorn structure is obtained on conducting carbon felts via facile in situ polymerization through chemical oxidation, for application as a storage material for NH_4^+ ion storage. The surface areas of these two nanomaterials are 38.9311 and 34.8328 m^2g^{-1} respectively which is an advantage because it give them a high surface area for electrochemical reactions to occur thus fast redox kinetics and thereby improving the electrochemical performance. At a specific current of 1 A g^{-1}, the ES-PANI delivers an initial discharge capacity of 160 mAh g^{-1} and initial charge capacity of 171 mAh g^{-1}, resulting in a coulombic efficiency of 93.4% and EB-PANI delivers 116 mAh g^{-1}. Of particular importance is the excellent cycling stability of the ES-PANI with capacity retention of 82% after 100 cycles at specific capacity of 5 A g^{-1}. These results together with the remarkable rate capability of the ES-PANI demonstrate that ES-PANI can be applied as a high-potential electrode material for NH_4^+ ion storage in a new aqueous rechargeable battery. The ES-PANI in our work has the optimum degree of oxidation and protonation, resulting in the formation of emeraldine salt with much increased conductivity. When PANI is doped, local charge carriers are generated. These charges can move because of the conjugated π-electron system on the polymer chains of PANI. Through the interaction with the PANI environment, the charge carriers undergo relaxation, causing the distortions of bipolarons, polarons and solitons, which can migrate intra and intermolecularly within PANI, thus giving ES-PANI high conductivity whereas EB-PANI is not deoped. These factors in addition to the large surface area and short diffusion paths of the nanothorn-structured ES-PANI on CFs lead to its high capacity for NH_4^+ storage. Moreover, the intercalation and deintercalation of NH_4^+ ion are shown to be highly reversible in the PANI doped with Cl^- ions, demonstrating that NH_4^+ ion is a promising charge carrier for new electrochemical energy technology and PANI as a very promising electrode material for NH_4^+ storage.

Flexible electronics require flexible batteries that can be bent without changing their electrochemical performance. The critical part in flexible batteries is the electrolyte which cannot be an aqueous electrolytes as it can leak causing short circuit. Non-metallic NH_4^+ ion redox chemistry is utilized to demonstrate a full flexible AIBs, composed of the $NH_4V_3O_8{\cdot}2.9H_2O$ as cathode and the PANI anode as well as the concentrated hydrogel electrolyte containing ammonium sulfate and xanthan gum. As proof of concept first, the cathode and the anode are assembled with aqueous 1 M $(NH_4)_2SO_4$ electrolyte for electrochemical performance evaluation. The resulting battery delivers an impressive capacity of 121 mA h g^{-1}, stable cycling performance and a capacity retention of 95% after 400 cycles. To enable the flexible battery, we facially

synthesized a hydrogel electrolyte composed of the electrolyte salt, water, and xanthan gum. The salt concentration in the gel electrolyte is tuned and optimized to maximize the battery performance, and it is found that the battery based on the quasi solid state electrolyte prepared from 3 M salt solution shows the highest capacity of 55 mAh g^{-1} and the best performance can be ascribed to the increased ionic conductivity, reduced side reactions, and suppressed active material dissolution resulted from the high salt concentration. This battery also delivers excellent cycling perfomance with a high capacity retention of 98% after 250 cycles as well as maintaining the capacity whilst bent at different angles 90 and 180 degrees and undergoing electrochemical cycling silmultaneously, demonstrating remarkable mechanical strength and flexibility. As such, the full flexible AIB in this work shows high potential as a safe and low-cost power source to meet the demands of the fast expanding market of wearable electronics.

To enhance the capacity of PANI one strategy is to prepare a composite material with another electroactive material. By using this strategy, we employ an in-situ intercalation approach to prepare PANI-intercalated V_2O_5 (PVO) to improve the NH_4^+ kinetics in AIBs. The structure obtained, composed of a monolayer of PANI in the bi-layered V_2O_5 to expand its interlayer spacing and diffusion channels, shows a nanoflower morphology with larger surface area than the original parent structure, thereby accommodating more NH_4^+ ions and resulting in better electrochemical performance. The easy synthesis of the PVO electrode allows facile tuning of the composition of the PVO to maximize the transport kinetics and the battery performance. It is found that the PVO60 delivers the best electrochemical property, showing a capacity of 192.5 mA hg^{-1} and 39 mA hg^{-1} at specific currents of 1 and 20 A g^{-1} respectively as well as excellent cycling stability with a capacity retention of 98% over 100 cycles at either 10 or 20 A g^{-1}. Additionally, the ammonium-ion transport kinetics and intercalation mechanism in the AIB based on PVO60 are explored via XRD, XPS and Raman spectroscopy. It is found that the formation/breaking of hydrogen bonds occurs during the NH_4^+ (de)intercalation process within the layered structure of PVO60, and thus the hydrogen bonding dominates the NH_4^+ redox chemistry. As such, this work sheds light on the design and synthesis of high-capacity electrode materials to boost the electrochemical performance of emerging ammonium-ion batteries with intrinsic safety and low cost.

Most commercial batteries use metal ions either in their cathode, anode or in their electrolytes. This influences the end life of these batteries as these metals are heavy nonrenewable metals. In our research we also explored a metal free battery that can also operate at a low temperature of 0°C. Firstly we exhibited Polypyrrole (PPy) as a high-capacity material for NH_4^+ ion storage, exhibiting a capacity of 125 mA h g^{-1} at 1 A g^{-1} in a water in salt electrolyte (WISE). A comparative study was carried out on PPy for K^+ storage as this ion has similar physical properties to NH_4^+ ion such as same coordination number (CN) of 6, ionic radius of 1.38 Å for K^+ vs. ionic radius of 1.48 Å. PPy showed a high reversible capacity of 97.22 mA hg^{-1} at 1 A g^{-1} in 1m potassium acetate electrolyte. Additionally, water in salt electrolyte (WiSE) is employed to improve the performance of the batteries, as WiSE offers better properties than conventional electrolytes, including expanded electrochemical window, inhibited parasitic side reactions, and suppressed metal dissolution. Their physical properties were explored by using NMR, Raman spectroscopies. Another advantage provided by WiSE is a lower freezing point due to fewer free

water molecules in WiSE compared to conventional diluted electrolytes, which makes it possible to develop batteries that can operate at subzero temperatures. A metal free battery consisting of PANI as anode, PPy as cathode with 19 m WISE electrolyte was explored for use at 0°C and exhibited a reversible capacity of 78.405 mA h g^{-1} at a specific current of 1 A g^{-1}.

In conclusion this dissertation work provides insights into the development of high-performance future ammonium ion batteries from the anode, cathode, and electrolyte aspect. For electrolytes quasi solid-state electrolytes can be used in flexible batteries and WiSE electrolytes for use in low temperature batteries.

Appendix. Copyright Information.

1. Permission to use published materials of ACS publications for figure 1.0 in Chapter 1.

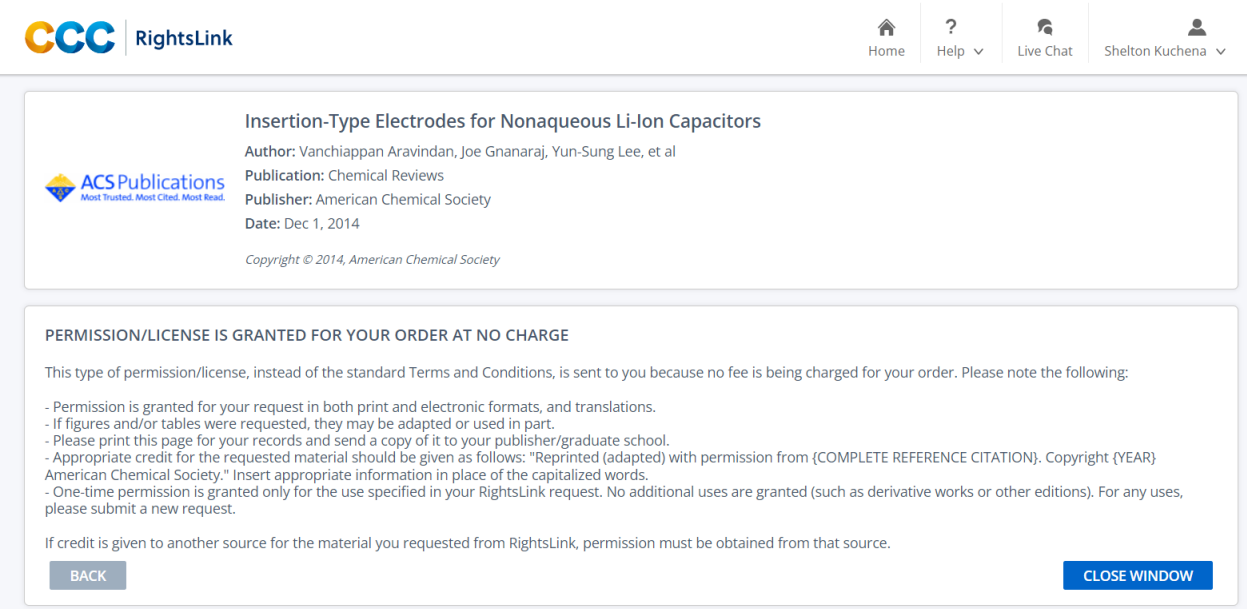

02-02-2023 04:59:25 PM EST - Drew Jenkins Additional comments

Hello Dr. Shelton Farai Kuchena,

I hope this message reaches you well, and thank you for contacting ACS Publications Support.

Your permission requested is granted and there is no fee for this reuse.

In your planned reuse, you must cite the ACS article as the source, add this direct link: https://pubs.acs.org/doi/10.1021/acsaem.0c01791 and include a notice to readers that further permission related to the material excerpted should be directed to the ACS.

Please do not hesitate to contact me if you need any further assistance.

Drew Jenkins
ACS Publications Support
Customer Services & Information
Website: https://acs.service-now.com/acs
Email: support@services.acs.org
Phone: 800-227-9919 | 202-872-(HELP) 4357

2. Permission to use published materials from ACS publications for figure 1.3 in Chapter 1.

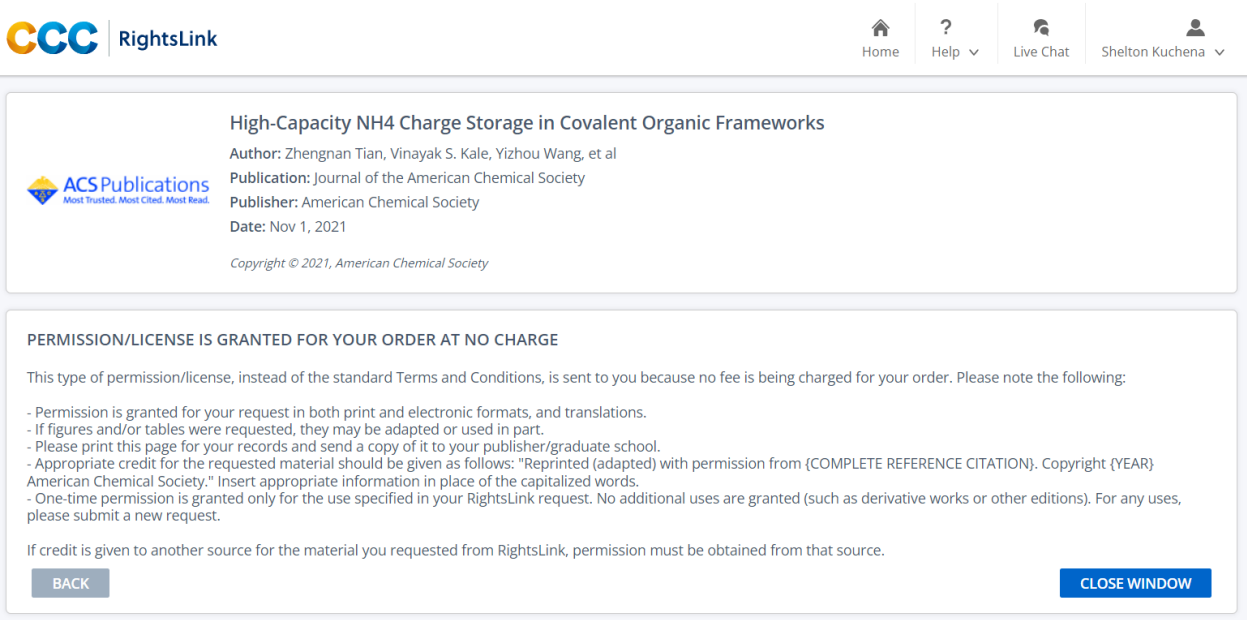

3. Permission to use published materials of Elsevier publications for figure 1.4 in Chapter 1.

ELSEVIER LICENSE
TERMS AND CONDITIONS

Feb 02, 2023

This Agreement between Mr. Shelton Kuchena ("You") and Elsevier ("Elsevier") consists of your license details and the terms and conditions provided by Elsevier and Copyright Clearance Center.

License Number	5480960172387
License date	Feb 02, 2023
Licensed Content Publisher	Elsevier
Licensed Content Publication	Chem
Licensed Content Title	Ultra-fast NH4 + Storage: Strong H Bonding between NH4 + and Bi-layered V2O5
Licensed Content Author	Shengyang Dong,Woochul Shin,Heng Jiang,Xianyong Wu,Zhifei Li,John Holoubek,William F. Stickle,Baris Key,Cong Liu,Jun Lu,P.Alex. Greaney,Xiaogang Zhang,Xiulei Ji
Licensed Content Date	Jun 13, 2019
Licensed Content Volume	5
Licensed Content Issue	6
Licensed Content Pages	15
Start Page	1537

End Page	1551
Type of Use	reuse in a thesis/dissertation
Portion	figures/tables/illustrations
Number of figures/tables/illustrations	1
Format	both print and electronic
Are you the author of this Elsevier article?	No
Will you be translating?	No
Title	DEVELOPMENT OF NOVEL ELECTRODES AND ELECTROLYTES FOR SAFER AQUEOUS AMMONIUM-ION BATTERIES WITH ENHANCED PERFORMANCE
Institution name	Louisiana State University
Expected presentation date	Mar 2023
Portions	Figure 4
Requestor Location	Mr. Shelton Kuchena 3235 Barton Rouge, LA 70803 Highland Road BATON ROUGE, LA 70803 United States Attn: Louisiana State University
Publisher Tax ID	98-0397604
Total	0.00 USD

1.

Terms and Conditions

INTRODUCTION

1. The publisher for this copyrighted material is Elsevier. By clicking "accept" in connection with completing this licensing transaction, you agree that the following terms and conditions apply to this transaction (along with the Billing and Payment terms and conditions established by Copyright Clearance Center, Inc. ("CCC"), at the time that you opened your Rightslink account and that are available at any time at http://myaccount.copyright.com).

GENERAL TERMS

2. Elsevier hereby grants you permission to reproduce the aforementioned material subject to the terms and conditions indicated.

3. Acknowledgement: If any part of the material to be used (for example, figures) has appeared in our publication with credit or acknowledgement to another source, permission must also be sought from that source. If such permission is not obtained then that material may not be included in your publication/copies. Suitable acknowledgement to the source must be made, either as a footnote or in a reference list at the end of your publication, as follows:

"Reprinted from Publication title, Vol /edition number, Author(s), Title of article / title of chapter, Pages No., Copyright (Year), with permission from Elsevier [OR APPLICABLE SOCIETY COPYRIGHT OWNER]." Also Lancet special credit - "Reprinted from The Lancet, Vol. number, Author(s), Title of article, Pages No., Copyright (Year), with permission from Elsevier."

4. Reproduction of this material is confined to the purpose and/or media for which permission is hereby given.

5. Altering/Modifying Material: Not Permitted. However figures and illustrations may be altered/adapted minimally to serve your work. Any other abbreviations, additions, deletions and/or any other alterations shall be made only with prior written authorization of Elsevier Ltd. (Please contact Elsevier's permissions helpdesk here). No modifications can be made to any Lancet figures/tables and they must be reproduced in full.

6. If the permission fee for the requested use of our material is waived in this instance, please be advised that your future requests for Elsevier materials may attract a fee.

7. Reservation of Rights: Publisher reserves all rights not specifically granted in the combination of (i) the license details provided by you and accepted in the course of this licensing transaction, (ii) these terms and conditions and (iii) CCC's Billing and Payment terms and conditions.

8. License Contingent Upon Payment: While you may exercise the rights licensed immediately upon issuance of the license at the end of the licensing process for the transaction, provided that you have disclosed complete and accurate details of your proposed use, no license is finally effective unless and until full payment is received from you (either by publisher or by CCC) as provided in CCC's Billing and Payment terms and conditions. If full payment is not received on a timely basis, then any license preliminarily granted shall be deemed automatically revoked and shall be void as if never granted. Further, in the event that you breach any of these terms and conditions or any of CCC's Billing and Payment

terms and conditions, the license is automatically revoked and shall be void as if never granted. Use of materials as described in a revoked license, as well as any use of the materials beyond the scope of an unrevoked license, may constitute copyright infringement and publisher reserves the right to take any and all action to protect its copyright in the materials.

9. Warranties: Publisher makes no representations or warranties with respect to the licensed material.

10. Indemnity: You hereby indemnify and agree to hold harmless publisher and CCC, and their respective officers, directors, employees and agents, from and against any and all claims arising out of your use of the licensed material other than as specifically authorized pursuant to this license.

11. No Transfer of License: This license is personal to you and may not be sublicensed, assigned, or transferred by you to any other person without publisher's written permission.

12. No Amendment Except in Writing: This license may not be amended except in a writing signed by both parties (or, in the case of publisher, by CCC on publisher's behalf).

13. Objection to Contrary Terms: Publisher hereby objects to any terms contained in any purchase order, acknowledgment, check endorsement or other writing prepared by you, which terms are inconsistent with these terms and conditions or CCC's Billing and Payment terms and conditions. These terms and conditions, together with CCC's Billing and Payment terms and conditions (which are incorporated herein), comprise the entire agreement between you and publisher (and CCC) concerning this licensing transaction. In the event of any conflict between your obligations established by these terms and conditions and those established by CCC's Billing and Payment terms and conditions, these terms and conditions shall control.

14. Revocation: Elsevier or Copyright Clearance Center may deny the permissions described in this License at their sole discretion, for any reason or no reason, with a full refund payable to you. Notice of such denial will be made using the contact information provided by you. Failure to receive such notice will not alter or invalidate the denial. In no event will Elsevier or Copyright Clearance Center be responsible or liable for any costs, expenses or damage incurred by you as a result of a denial of your permission request, other than a refund of the amount(s) paid by you to Elsevier and/or Copyright Clearance Center for denied permissions.

LIMITED LICENSE

The following terms and conditions apply only to specific license types:

15. **Translation**: This permission is granted for non-exclusive world **English** rights only unless your license was granted for translation rights. If you licensed translation rights you may only translate this content into the languages you requested. A professional translator must perform all translations and reproduce the content word for word preserving the integrity of the article.

16. **Posting licensed content on any Website**: The following terms and conditions apply as follows: Licensing material from an Elsevier journal: All content posted to the web site must maintain the copyright information line on the bottom of each image; A hyper-text must be included to the Homepage of the journal from which you are licensing at http://www.sciencedirect.com/science/journal/xxxxx or the Elsevier homepage for books at http://www.elsevier.com; Central Storage: This license does not include permission for a

scanned version of the material to be stored in a central repository such as that provided by Heron/XanEdu.

Licensing material from an Elsevier book: A hyper-text link must be included to the Elsevier homepage at http://www.elsevier.com . All content posted to the web site must maintain the copyright information line on the bottom of each image.

Posting licensed content on Electronic reserve: In addition to the above the following clauses are applicable: The web site must be password-protected and made available only to bona fide students registered on a relevant course. This permission is granted for 1 year only. You may obtain a new license for future website posting.

17. **For journal authors:** the following clauses are applicable in addition to the above:

Preprints:

A preprint is an author's own write-up of research results and analysis, it has not been peer-reviewed, nor has it had any other value added to it by a publisher (such as formatting, copyright, technical enhancement etc.).

Authors can share their preprints anywhere at any time. Preprints should not be added to or enhanced in any way in order to appear more like, or to substitute for, the final versions of articles however authors can update their preprints on arXiv or RePEc with their Accepted Author Manuscript (see below).

If accepted for publication, we encourage authors to link from the preprint to their formal publication via its DOI. Millions of researchers have access to the formal publications on ScienceDirect, and so links will help users to find, access, cite and use the best available version. Please note that Cell Press, The Lancet and some society-owned have different preprint policies. Information on these policies is available on the journal homepage.

Accepted Author Manuscripts: An accepted author manuscript is the manuscript of an article that has been accepted for publication and which typically includes author-incorporated changes suggested during submission, peer review and editor-author communications.

Authors can share their accepted author manuscript:

- immediately
  - via their non-commercial person homepage or blog
  - by updating a preprint in arXiv or RePEc with the accepted manuscript
  - via their research institute or institutional repository for internal institutional uses or as part of an invitation-only research collaboration work-group
  - directly by providing copies to their students or to research collaborators for their personal use
  - for private scholarly sharing as part of an invitation-only work group on commercial sites with which Elsevier has an agreement
- After the embargo period
  - via non-commercial hosting platforms such as their institutional repository
  - via commercial sites with which Elsevier has an agreement

In all cases accepted manuscripts should:

- link to the formal publication via its DOI

- bear a CC-BY-NC-ND license - this is easy to do
- if aggregated with other manuscripts, for example in a repository or other site, be shared in alignment with our hosting policy not be added to or enhanced in any way to appear more like, or to substitute for, the published journal article.

Published journal article (JPA): A published journal article (PJA) is the definitive final record of published research that appears or will appear in the journal and embodies all value-adding publishing activities including peer review co-ordination, copy-editing, formatting, (if relevant) pagination and online enrichment.

Policies for sharing publishing journal articles differ for subscription and gold open access articles:

Subscription Articles: If you are an author, please share a link to your article rather than the full-text. Millions of researchers have access to the formal publications on ScienceDirect, and so links will help your users to find, access, cite, and use the best available version.

Theses and dissertations which contain embedded PJAs as part of the formal submission can be posted publicly by the awarding institution with DOI links back to the formal publications on ScienceDirect.

If you are affiliated with a library that subscribes to ScienceDirect you have additional private sharing rights for others' research accessed under that agreement. This includes use for classroom teaching and internal training at the institution (including use in course packs and courseware programs), and inclusion of the article for grant funding purposes.

Gold Open Access Articles: May be shared according to the author-selected end-user license and should contain a CrossMark logo, the end user license, and a DOI link to the formal publication on ScienceDirect.

Please refer to Elsevier's posting policy for further information.

18. **For book authors** the following clauses are applicable in addition to the above: Authors are permitted to place a brief summary of their work online only. You are not allowed to download and post the published electronic version of your chapter, nor may you scan the printed edition to create an electronic version. **Posting to a repository:** Authors are permitted to post a summary of their chapter only in their institution's repository.

19. **Thesis/Dissertation**: If your license is for use in a thesis/dissertation your thesis may be submitted to your institution in either print or electronic form. Should your thesis be published commercially, please reapply for permission. These requirements include permission for the Library and Archives of Canada to supply single copies, on demand, of the complete thesis and include permission for Proquest/UMI to supply single copies, on demand, of the complete thesis. Should your thesis be published commercially, please reapply for permission. Theses and dissertations which contain embedded PJAs as part of the formal submission can be posted publicly by the awarding institution with DOI links back to the formal publications on ScienceDirect.

Elsevier Open Access Terms and Conditions

You can publish open access with Elsevier in hundreds of open access journals or in nearly 2000 established subscription journals that support open access publishing. Permitted third

party re-use of these open access articles is defined by the author's choice of Creative Commons user license. See our open access license policy for more information.

Terms & Conditions applicable to all Open Access articles published with Elsevier:

Any reuse of the article must not represent the author as endorsing the adaptation of the article nor should the article be modified in such a way as to damage the author's honour or reputation. If any changes have been made, such changes must be clearly indicated.

The author(s) must be appropriately credited and we ask that you include the end user license and a DOI link to the formal publication on ScienceDirect.

If any part of the material to be used (for example, figures) has appeared in our publication with credit or acknowledgement to another source it is the responsibility of the user to ensure their reuse complies with the terms and conditions determined by the rights holder.

Additional Terms & Conditions applicable to each Creative Commons user license:

CC BY: The CC-BY license allows users to copy, to create extracts, abstracts and new works from the Article, to alter and revise the Article and to make commercial use of the Article (including reuse and/or resale of the Article by commercial entities), provided the user gives appropriate credit (with a link to the formal publication through the relevant DOI), provides a link to the license, indicates if changes were made and the licensor is not represented as endorsing the use made of the work. The full details of the license are available at http://creativecommons.org/licenses/by/4.0.

CC BY NC SA: The CC BY-NC-SA license allows users to copy, to create extracts, abstracts and new works from the Article, to alter and revise the Article, provided this is not done for commercial purposes, and that the user gives appropriate credit (with a link to the formal publication through the relevant DOI), provides a link to the license, indicates if changes were made and the licensor is not represented as endorsing the use made of the work. Further, any new works must be made available on the same conditions. The full details of the license are available at http://creativecommons.org/licenses/by-nc-sa/4.0.

CC BY NC ND: The CC BY-NC-ND license allows users to copy and distribute the Article, provided this is not done for commercial purposes and further does not permit distribution of the Article if it is changed or edited in any way, and provided the user gives appropriate credit (with a link to the formal publication through the relevant DOI), provides a link to the license, and that the licensor is not represented as endorsing the use made of the work. The full details of the license are available at http://creativecommons.org/licenses/by-nc-nd/4.0. Any commercial reuse of Open Access articles published with a CC BY NC SA or CC BY NC ND license requires permission from Elsevier and will be subject to a fee.

Commercial reuse includes:

- Associating advertising with the full text of the Article
- Charging fees for document delivery or access
- Article aggregation
- Systematic distribution via e-mail lists or share buttons

Posting or linking by commercial companies for use by customers of those companies.

20. **Other Conditions**:

v1.10

Questions? customercare@copyright.com or +1-855-239-3415 (toll free in the US) or +1-978-646-2777.

4. Permission to use published material from ACS Publications for Chapter 2.

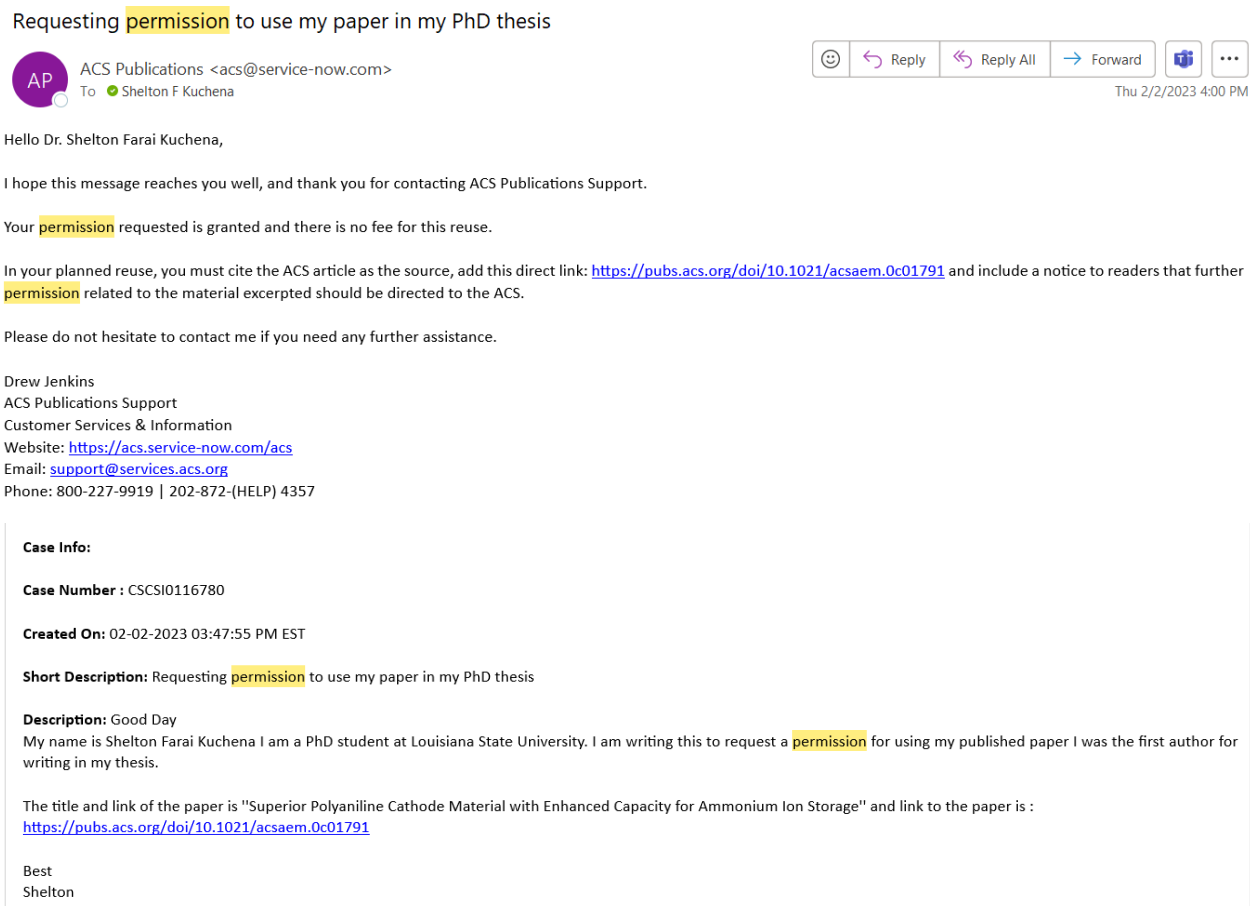

Requesting permission to use my paper in my PhD thesis

AP ACS Publications <acs@service-now.com>
To Shelton F Kuchena

Reply | Reply All | Forward

Thu 2/2/2023 4:00 PM

Hello Dr. Shelton Farai Kuchena,

I hope this message reaches you well, and thank you for contacting ACS Publications Support.

Your permission requested is granted and there is no fee for this reuse.

In your planned reuse, you must cite the ACS article as the source, add this direct link: https://pubs.acs.org/doi/10.1021/acsaem.0c01791 and include a notice to readers that further permission related to the material excerpted should be directed to the ACS.

Please do not hesitate to contact me if you need any further assistance.

Drew Jenkins
ACS Publications Support
Customer Services & Information
Website: https://acs.service-now.com/acs
Email: support@services.acs.org
Phone: 800-227-9919 | 202-872-(HELP) 4357

Case Info:

Case Number : CSCSI0116780

Created On: 02-02-2023 03:47:55 PM EST

Short Description: Requesting permission to use my paper in my PhD thesis

Description: Good Day
My name is Shelton Farai Kuchena I am a PhD student at Louisiana State University. I am writing this to request a permission for using my published paper I was the first author for writing in my thesis.

The title and link of the paper is ''Superior Polyaniline Cathode Material with Enhanced Capacity for Ammonium Ion Storage'' and link to the paper is :
https://pubs.acs.org/doi/10.1021/acsaem.0c01791

Best
Shelton

5. Permission for use of published material from Wiley library for Chapter 3.

JOHN WILEY AND SONS LICENSE
TERMS AND CONDITIONS

Feb 02, 2023

This Agreement between Mr. Shelton Kuchena ("You") and John Wiley and Sons ("John Wiley and Sons") consists of your license details and the terms and conditions provided by John Wiley and Sons and Copyright Clearance Center.

License Number	5480941434645
License date	Feb 02, 2023
Licensed Content Publisher	John Wiley and Sons
Licensed Content Publication	Chemistry - A European Journal
Licensed Content Title	A Full Flexible NH4 Ion Battery Based on the Concentrated Hydrogel Electrolyte for Enhanced Performance
Licensed Content Author	Shelton Farai Kuchena, Ying Wang
Licensed Content Date	Oct 5, 2021
Licensed Content Volume	27
Licensed Content Issue	62
Licensed Content Pages	10

Type of use	Dissertation/Thesis
Requestor type	Author of this Wiley article
Format	Print and electronic
Portion	Full article
Will you be translating?	No
Title	DEVELOPMENT OF NOVEL ELECTRODES AND ELECTROLYTES FOR SAFER AQUEOUS AMMONIUM-ION BATTERIES WITH ENHANCED PERFORMANCE
Institution name	Louisiana State University
Expected presentation date	Mar 2023
Requestor Location	Mr. Shelton Kuchena 3235 Barton Rouge, LA 70803 Highland Road BATON ROUGE, LA 70803 United States Attn: Louisiana State University
Publisher Tax ID	EU826007151
Total	0.00 USD

Terms and Conditions

TERMS AND CONDITIONS

This copyrighted material is owned by or exclusively licensed to John Wiley & Sons, Inc. or one of its group companies (each a"Wiley Company") or handled on behalf of a society with which a Wiley Company has exclusive publishing rights in relation to a particular work (collectively "WILEY"). By clicking "accept" in connection with completing this licensing transaction, you agree that the following terms and conditions apply to this transaction

(along with the billing and payment terms and conditions established by the Copyright Clearance Center Inc., ("CCC's Billing and Payment terms and conditions"), at the time that you opened your RightsLink account (these are available at any time at http://myaccount.copyright.com).

Terms and Conditions

- The materials you have requested permission to reproduce or reuse (the "Wiley Materials") are protected by copyright.
- You are hereby granted a personal, non-exclusive, non-sub licensable (on a stand-alone basis), non-transferable, worldwide, limited license to reproduce the Wiley Materials for the purpose specified in the licensing process. This license, **and any CONTENT (PDF or image file) purchased as part of your order,** is for a one-time use only and limited to any maximum distribution number specified in the license. The first instance of republication or reuse granted by this license must be completed within two years of the date of the grant of this license (although copies prepared before the end date may be distributed thereafter). The Wiley Materials shall not be used in any other manner or for any other purpose, beyond what is granted in the license. Permission is granted subject to an appropriate acknowledgement given to the author, title of the material/book/journal and the publisher. You shall also duplicate the copyright notice that appears in the Wiley publication in your use of the Wiley Material. Permission is also granted on the understanding that nowhere in the text is a previously published source acknowledged for all or part of this Wiley Material. Any third party content is expressly excluded from this permission.
- With respect to the Wiley Materials, all rights are reserved. Except as expressly granted by the terms of the license, no part of the Wiley Materials may be copied, modified, adapted (except for minor reformatting required by the new Publication), translated, reproduced, transferred or distributed, in any form or by any means, and no derivative works may be made based on the Wiley Materials without the prior permission of the respective copyright owner.**For STM Signatory Publishers clearing permission under the terms of the STM Permissions Guidelines only, the terms of the license are extended to include subsequent editions and for editions in other languages, provided such editions are for the work as a whole in situ and does not involve the separate exploitation of the permitted figures or extracts,** You may not alter, remove or suppress in any manner any copyright, trademark or other notices displayed by the Wiley Materials. You may not license, rent, sell, loan, lease, pledge, offer as security, transfer or assign the Wiley Materials on a stand-alone basis, or any of the rights granted to you hereunder to any other person.
- The Wiley Materials and all of the intellectual property rights therein shall at all times remain the exclusive property of John Wiley & Sons Inc, the Wiley Companies, or their respective licensors, and your interest therein is only that of having possession of and the right to reproduce the Wiley Materials pursuant to Section 2 herein during the continuance of this Agreement. You agree that you own no right, title or interest in or to the Wiley Materials or any of the intellectual property rights therein. You shall have no rights hereunder other than the license as provided for above in Section 2. No right, license or interest to any trademark, trade name, service mark or other branding ("Marks") of WILEY or its licensors is granted hereunder, and you agree that you shall not assert any such right, license or interest with respect thereto

- These terms and conditions together with CCC's Billing and Payment terms and conditions (which are incorporated herein) form the entire agreement between you and WILEY concerning this licensing transaction and (in the absence of fraud) supersedes all prior agreements and representations of the parties, oral or written. This Agreement may not be amended except in writing signed by both parties. This Agreement shall be binding upon and inure to the benefit of the parties' successors, legal representatives, and authorized assigns.

- In the event of any conflict between your obligations established by these terms and conditions and those established by CCC's Billing and Payment terms and conditions, these terms and conditions shall prevail.

- WILEY expressly reserves all rights not specifically granted in the combination of (i) the license details provided by you and accepted in the course of this licensing transaction, (ii) these terms and conditions and (iii) CCC's Billing and Payment terms and conditions.

- This Agreement will be void if the Type of Use, Format, Circulation, or Requestor Type was misrepresented during the licensing process.

- This Agreement shall be governed by and construed in accordance with the laws of the State of New York, USA, without regards to such state's conflict of law rules. Any legal action, suit or proceeding arising out of or relating to these Terms and Conditions or the breach thereof shall be instituted in a court of competent jurisdiction in New York County in the State of New York in the United States of America and each party hereby consents and submits to the personal jurisdiction of such court, waives any objection to venue in such court and consents to service of process by registered or certified mail, return receipt requested, at the last known address of such party.

WILEY OPEN ACCESS TERMS AND CONDITIONS

Wiley Publishes Open Access Articles in fully Open Access Journals and in Subscription journals offering Online Open. Although most of the fully Open Access journals publish open access articles under the terms of the Creative Commons Attribution (CC BY) License only, the subscription journals and a few of the Open Access Journals offer a choice of Creative Commons Licenses. The license type is clearly identified on the article.

The Creative Commons Attribution License

The Creative Commons Attribution License (CC-BY) allows users to copy, distribute and transmit an article, adapt the article and make commercial use of the article. The CC-BY license permits commercial and non-

Creative Commons Attribution Non-Commercial License

The Creative Commons Attribution Non-Commercial (CC-BY-NC)License permits use, distribution and reproduction in any medium, provided the original work is properly cited and is not used for commercial purposes.(see below)

Creative Commons Attribution-Non-Commercial-NoDerivs License

The Creative Commons Attribution Non-Commercial-NoDerivs License (CC-BY-NC-ND) permits use, distribution and reproduction in any medium, provided the original work is

6. Permission to use published materials of Elsevier publications for Chapter 4.

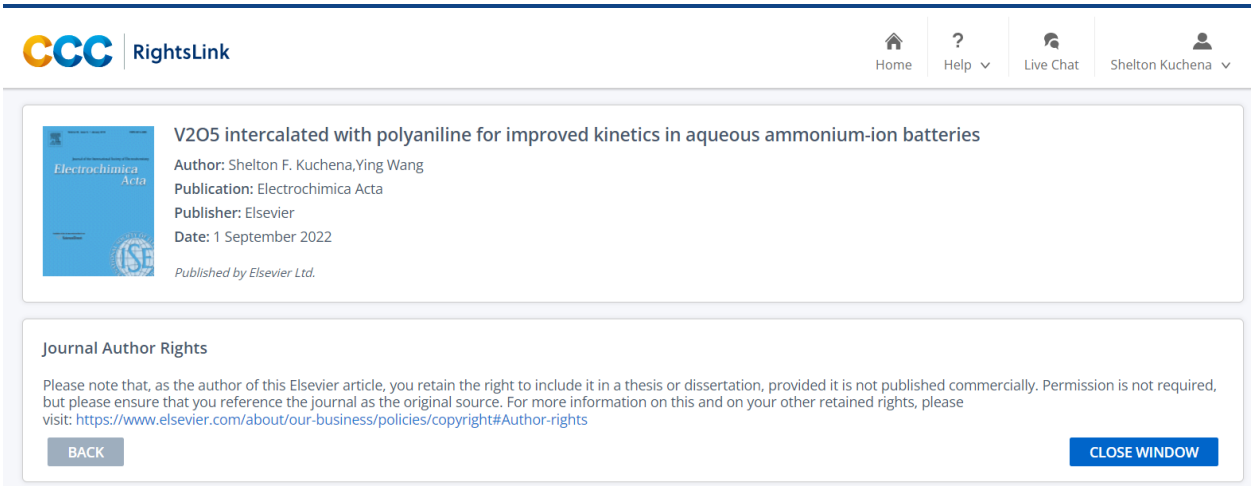

7. Permission to use published materials of ACS publications for Chapter 5.

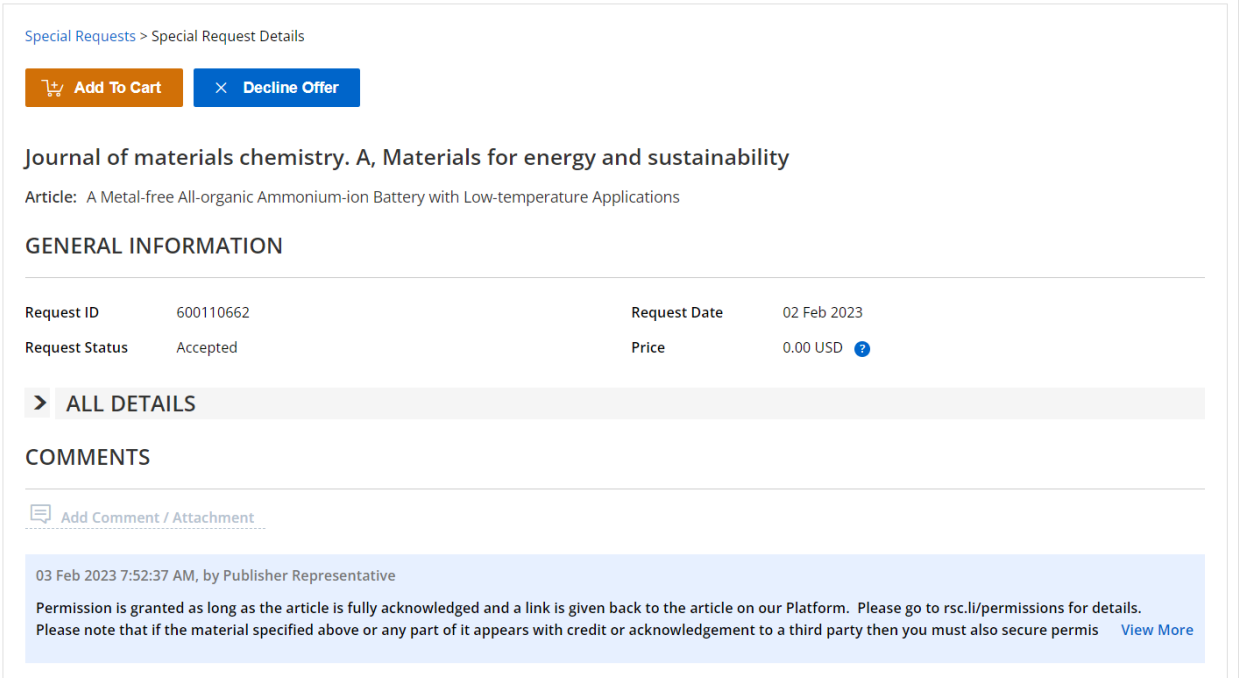

References

1. Farhidi, Faraz, and Zaeng Mawi. "Is It Costly to Transition from Fossil Fuel Energy: A Trade-Off Analysis." *Energies* 15, no. 21 (2022): 7873.

2. Depren, Serpil Kılıç, Mustafa Tevfik Kartal, Neşe Çoban Çelikdemir, and Özer Depren. *Ecological Informatics* 70 (2022): 101747.

3. Aravindan, Vanchiappan, Joe Gnanaraj, Yun-Sung Lee, and Srinivasan Madhavi. *Chemical reviews* 114, no. 23 (2014): 11619-11635.

4. Li, Xiuwan, Zhibo Yang, Yujun Fu, Li Qiao, Dan Li, Hongwei Yue, and Deyan He. ACS nano 9, no. 2 (2015): 1858-1867.

5. R.T. Zheng, S.S. Qian, X. Cheng, H.X. Yu, N. Peng, T.T. Liu, J.D. Zhang, M.T. Xia, H. J. Zhu, J. Shu, FeNb11O29 nanotubes: Nano Energy 58 (2019) 399–409.

6. B. Guo, X. Yu, X.-G. Sun, M. Chi, Z.-A. Qiao, J. Liu, Y.-S. Hu, X.-Q. Yang, J. B. Goodenough, S. Dai, Energy Environ. Sci. 7 (7)

7. K.-S. Park, D. Im, A. Benayad, A. Dylla, K.J. Stevenson, J.B. Goodenough, , Chem. Mater. 24 (14) (2012) 2673–2683. (2014) 2220–2226.

8. Zhu, Gao-Long, Chen-Zi Zhao, Jia-Qi Huang, Chuanxin He, Jian Zhang, Shaohai Chen, Lei Xu, Hong Yuan, and Qiang Zhang. Small 15, no. 15 (2019): 1805389.

9. Sun, Yang, Zhenzhong Yang, Lin Gu, Yong Chen, and Haoshen Zhou. Joule 2, no. 7 (2018): 1265-1277.

10. Wen, Jianwu, Yan Yu, and Chunhua Chen. *Materials express* 2, no. 3 (2012): 197-212.

11. Macioszek, Elżbieta. *Research Methods in Modern Urban Transportation Systems and Networks* (2021): 41-58.

12. Yoo, Hyun Deog, Ivgeni Shterenberg, Yosef Gofer, G. Gershinsky, Nir Pour, and Doron Aurbach. "Energy Environ." *Sci* 6 (2013): 2265-2279.

13. Levi, E., M. D. Levi, O. Chasid, and D. Aurbach. *Journal of Electroceramics* 22, no. 1-3 (2009): 13-19.

14. Das, Shyamal K., Sadhan Mahapatra, and Homen Lahan. *Journal of Materials Chemistry A* 5, no. 14 (2017): 6347-6367.

15. Jayaprakash, N., S. K. Das, and L. A. Archer. " *Chemical Communications* 47, no. 47 (2011): 12610-12612.

16. D. Chao, H.J. Fan, , Chem 5 (6) (2019) 1359–1361.

17. X.Y. Wu, Y.T. Qi, J.J. Hong, Z.F. Li, A.S. Hernandez, X.L. Ji, Angew. Chem. Int. Ed. 56 (2017) 13026–13030.

18. Saito, Morihiro, Satoru Kawaharasaki, Kensuke Ito, Shinya Yamada, Kikuko Hayamizu, and Shiro Seki. *RSC advances* 7, no. 24 (2017): 14528-14535.

19. Xu, Kang. *Chemical reviews* 104, no. 10 (2004): 4303-4418.

20. Tian, Zhengnan, Vinayak S. Kale, Yizhou Wang, Sharath Kandambeth, Justyna Czaban-Jozwiak, Osama Shekhah, Mohamed Eddaoudi, and Husam N. Alshareef. *Journal of the American Chemical Society* 143, no. 45 (2021): 19178-19186.

21. Ming, J.; Cao, Z.; Li, Q.; Wahyudi, W.; Wang, W.; Cavallo, L.; Park, K.-J.; Sun, Y.-K.; Alshareef, H. N. ACS Energy Lett. 2019, 4 (7), 1584−1593.

22. Sogawa, M.; Sawayama, S.; Han, J.; Satou, C.; Ohara, K.; Matsugami, M.; Mimura, H.; Morita, M.; Fujii, K. J. Phys. Chem. C 2019, 123 (14), 8699− 8708.

23. Wessells, Colin D., Matthew T. McDowell, Sandeep V. Peddada, Mauro Pasta, Robert A. Huggins, and Yi Cui. *ACS nano* 6, no. 2 (2012): 1688-1694.

24. Wu, Xianyong, Yitong Qi, Jessica J. Hong, Zhifei Li, Alexandre S. Hernandez, and Xiulei Ji. *Angewandte Chemie International Edition* 56, no. 42 (2017): 13026-13030.

25. Zhang, Xikun, Maoting Xia, Tingting Liu, Na Peng, Haoxiang Yu, Runtian Zheng, Liyuan Zhang, Miao Shui, and Jie Shu. *Chemical Engineering Journal* 421 (2021): 127767.

26. Zhang, Haode, Yu Tian, Wenxuan Wang, Zelang Jian, and Wen Chen *Angewandte Chemie* (2022).

27. Wu, Xianyong, Yunkai Xu, Heng Jiang, Zhixuan Wei, Jessica J. Hong, Alexandre S. Hernandez, Fei Du, and Xiulei Ji. *ACS Applied Energy Materials* 1, no. 7 (2018): 3077-3083.

28. Xia, Maoting, Xikun Zhang, Haoxiang Yu, Zhengwei Yang, Shi Chen, Liyuan Zhang, Miao Shui, Ying Xie, and Jie Shu. *Chemical Engineering Journal* 421 (2021): 127759.

29. Li, Chunyang, Wenqi Yan, Shishuo Liang, Peng Wang, Jing Wang, Lijun Fu, Yusong Zhu, Yuhui Chen, Yuping Wu, and Wei Huang. *Nanoscale Horizons* 4, no. 4 (2019): 991-998.

30. Li, Chunyang, Dexin Zhang, Fuxiang Ma, Tianyi Ma, Jing Wang, Yuhui Chen, Yusong Zhu, Lijun Fu, Yuping Wu, and Wei Huang. *ChemSusChem* 12, no. 16 (2019): 3732-3736.

31. Wessells, Colin D., Sandeep V. Peddada, Matthew T. McDowell, Robert A. Huggins, and Yi Cui. *Journal of The Electrochemical Society* 159, no. 2 (2011): A98.

32. Song, Yu, Qing Pan, Huizhen Lv, Duo Yang, Zengming Qin, Ming-Yue Zhang, Xiaoqi Sun, and Xiao-Xia Liu. *Angewandte Chemie* 133, no. 11 (2021): 5782-5786.

33. Xu, Wangwang, Lei Zhang, Kangning Zhao, Xiuxuan Sun, and Qinglin Wu. *Electrochimica Acta* 360 (2020): 137008.

34. Farai Kuchena, Shelton, and Ying Wang. " *Chemistry–A European Journal* 27, no. 62 (2021): 15450-15459.

35. Dong, Shengyang, Woochul Shin, Heng Jiang, Xianyong Wu, Zhifei Li, John Holoubek, William F. Stickle et al. Chem 5, no. 6 (2019): 1537-1551.

36. Zhigang Zhao, Tingting Yu, Yingchun Miao, Xiangyu Zhao, , Electrochimica Acta, Volume 270, 2018, Pages 30-36, ISSN 0013-4686

37. Wan, F.; Zhang, L.; Wang, X.; Bi, S.; Niu, Z.; Chen, J., **2018,** *28* (45), 1804975.

38. Deng, J.; Wang, X.; Guo, J.; Liu, P.,. *Industrial & Engineering Chemistry Research* **2014,** *53* (35), 13680-13689.

39. Benykhlef, S.; Bekhoukh, A.; Berenguer, R.; Benyoucef, A.; Morallon, E. J. C.; Science, P.,. **2016,** *294* (12), 1877-1885

40. Luo, Y.; Guo, R.; Li, T.; Li, F.; Liu, Z.; Zheng, M.; Wang, B.; Yang, Z.; Luo, H.; Wan, Y.,. **2019,** *12* (8), 1591-1611.

41. Ref: Nureddin Çolak & Bahar Sökmen (2000) 3:2, 181-189, DOI: 10.1163/156855500300142870.

42. Banerjee, D.; Kar, A. K.,. *Physical Chemistry Chemical Physics* **2018,** *20* (35), 23055-23071

43. Jeon, J.-W.; Ma, Y.; Mike, J. F.; Shao, L.; Balbuena, P. B.; Lutkenhaus, J. L., *Physical Chemistry Chemical Physics* **2013,** *15* (24), 9654-9662.

44. Mostafa, N. Y.; Mohamed, M. B.; Imam, N. G.; Alhamyani, M.; Heiba, Z. K., *Colloid and Polymer Science* **2016,** *294* (1), 215-224.

45. Cuiping Han, Jing Tong, Xiao Tang, Dong Zhou, Huan Duan, Baohua Li, and Guoxiu Wang

ACS Applied Materials & Interfaces **2020** *12* (9), 10479-10489

46. H. Gao, L. Xue, S. Xin, J. B. Goodenough, *Angew. Chem. Int. Ed.* **2018**, *57*, 5449.

47. Quinton K. Wyatt and Matthias J. Young 2020 *J. Electrochem. Soc.* **167** 110548

48. T. Yu, R. Yang, X. Zhao, X. Shen,

ChemElectroChem **2019**, *6*, 1761.

49. Zhigang Zhao, Tingting Yu, Yingchun Miao, Xiangyu Zhao, , Electrochimica Acta, Volume 270, 2018, Pages 30-36, ISSN 0013-4686

50. Hai, T. A. P.; Sugimoto, R., *Journal of Molecular Structure* **2017,** *1146*, 660-668

51. Číková, E.; Mičušík, M.; Šišková, A.; Procházka, M.; Fedorko, P.; Omastová, M.,. *Synthetic Metals* **2018,** *235*, 80-88.

52. Leguizamon, S.; Díaz-Orellana, K. P.; Velez, J.; Thies, M. C.; Roberts, M. E., *Journal of Materials Chemistry A* **2015,** *3* (21), 11330-11339.

53. Takamori, D. Y.; Bizeto, M. A.; Fantini, M. C. d. A.; Rubinger, C. P. L.; Faez, R.; Martins, T. S.,. *Microporous and Mesoporous Materials* **2019,** *274*, 212-219.

54. Sakai, Kazuki et al. *ACS omega* vol. 3,1 691-697.

55. Xu, J.; Wang, K.; Zu, S.-Z.; Han, B.-H.; Wei, Z.,. *ACS nano* **2010,** *4* (9), 5019-5026.

56. Chen, Y.; Lüder, J.; Ng, M.-F.; Sullivan, M.; Manzhos, S., *Physical Chemistry Chemical Physics* **2018,** *20* (1), 232-237.

22. Shi, Hua-Yu, Ye, Yin-Jian, Liu, Kuan, Sun, Xiaoqi., Angewandte Chemie International Edition **2018,** 5750 1433-7851

58. Özdemir, C.; Kaplan Can, H.; Çolak, N.; Güner, A.,**2006,** *99* (5), 2182-2192.

59. Agarwal, U. P.; Ralph, S. A.; Baez, C.; Reiner, R. S.; Verrill, S. P. J. C.,. **2017,** *24* (5), 1971-1984.

60. Reddy, K. R.; Karthik, K. V.; Prasad, S. B. B.; Soni, S. K.; Jeong, H. M.; Raghu, A. V.,. *Polyhedron* **2016,** *120*, 169-174.

61. Wu, X.; Qi, Y.; Hong, J. J.; Li, Z.; Hernandez, A. S.; Ji, X., Rocking-Chair Ammonium-Ion Battery: A Highly Reversible Aqueous Energy Storage Syst. **2017,** *56* (42), 13026-13030.

62. Dong, S.; Shin, W.; Jiang, H.; Wu, X.; Li, Z.; Holoubek, J.; Stickle, W. F.; Key, B.; Liu, C.; Lu, J.; Greaney, P. A.; Zhang, X.; Ji, X., *Chem* **2019,** *5* (6), 1537-1551.

63. Shimano, J. Y.; MacDiarmid, A. G., *Synthetic Metals* **2001,** *123* (2), 251-262.

64. Ryu, K. S.; Kim, K. M.; Kang, S.-G.; Lee, G. J.; Joo, J.; Chang, S. H., *Synthetic Metals* **2000,** *110* (3), 213-217.

65. Shi, Hua-Yu, Ye, Yin-Jian, Liu, Kuan, Sun, Xiaoqi., Angewandte Chemie International Edition **2018,** 5750 1433-7851

66. Shuai Wang, Shuo Huang, Minjie Yao, Yang Zhang, Zhiqiang Niu Angewandte Chemie International Edition **2020, 11898**-11905

67. Oleg Borodin, Julian Self, Kristin A. Persson, Chunsheng Wang, Kang Xu, , Joule, Volume 4, Issue 1, 2020, Pages 69-100, ISSN 2542-4351, https://doi.org/10.1016/j.joule.2019.12.007.

68. **Energy Environ. Sci.**, 2020,**13**, 4625-4665

69. Kundu, D., Adams, B., Duffort, V. *et al. . Nat Energy* **1,** 16119 (2016). https://doi.org/10.1038/nenergy.2016.119

70. Yangsheng Cai, Fei Liu, Zhigao Luo, Guozhao Fang, Jiang Zhou, Anqiang Pan, Shuquan Liang, Energy Storage Materials, Volume 13, 2018, Pages 168-174, ISSN 2405-8297, https://doi.org/10.1016/j.ensm.2018.01.009.

71. Zhiqiang Xie, Jianwei Lai, Xiuping Zhu, and Ying Wang *ACS Applied Energy Materials* **2018** *1* (11), 6401-6408 DOI: 10.1021/acsaem.8b01378

72. Y. Yang, Y. Tang, G. Fang, L. Shan, J. Guo, W. Zhang, C. Wang, L. Wang, J. Zhou and S. Liang, Energy Environ.Sci., 2018, 11, 3157–3162.

73. B. Tang, J. Zhou, G. Fang, F. Liu, C. Zhu, C. Wang, A. Pan and S. Liang, J. Mater. Chem. A, 2019, 7, 940–945.

74. F. Wan, L. Zhang, X. Dai, X. Wang, Z. Niu and J. Chen, Nat. Commun., 2018, 9, 1656.

75. B. Tang, G. Fang, J. Zhou, L. Wang, Y. Lei, C. Wang, T. Lin, Y. Tang and S. Liang, Nano Energy, 2018, 51, 579–587.

76. F. Ming, H. Liang, Y. Lei, S. Kandambeth, M. Eddaoudi and H. N. Alshareef, ACS Energy Lett., 2018, 3, 2602–2609.

77. H. Wang, Y. Ren, W. Wang, X. Huang, K. Huang, Y. Wang and S. Liu, J. Power Sources, 2012, 199, 315–321.

78. S. Sarkar, P. S. Veluri and S. Mitra, Electrochim. Acta, 2014, 132, 448–456.

79. H. Fei, X. Liu, Y. Lin and M. Wei, J. Colloid Interface Sci., 2014, 428, 73–77.

80. A. Sarkar, S. Sarkar, T. Sarkar, P. Kumar, M. D. Bharadwaj and S. Mitra, ACS Appl. Mater. Interfaces, 2015, 7, 17044– 17053.

81. E. A. Esparcia Jr, M. S. Chae, J. D. Ocon and S. T. Hong, Chem. Mater., 2018, 30, 3690–3696.

82. Hui Li, Jie Yang, Jianli Cheng, Tao He, Bin Wang, Nano Energy, Volume 68, 2020, 104369, ISSN 2211-2855, https://doi.org/10.1016/j.nanoen.2019.104369.

83. J. Mater. Chem. A, 2021,9, 2043-2069

84. A. Becker, F. Katzen, A. Pühler, L. Ielpi, *Appl. Microbiol. Biotechnol.* **1998**, *50*, 145.

85. B. Katzbauer, *Polym. Degrad. Stab.* **1998**, *59*, 81

86. D. Vernardou, M. Apostolopoulou, D. Louloudakis, N. Katsarakis and E. Koudoumas, New J. Chem., 2014, 38,2098–2104.

87. G. S. Zakharova, C. Taschner, T. Kolb, C. Jahne, A. Leonhardt, B. Buchner, and R. Klingler, Dalton Trans.,2013, 42, 4897–4902.

88. V. Soundharrajan, B. Sambandam, S. Kim, M. H. Alfaruqi, D. Y. Putro, J. Jo, S. Kim, V. Mathew, Y.-K. Sun, and J. Kim, Nano Lett., 2018, 18, 2402–2410.

89. C. Xia, J. Guo, P. Li, X. Zhang, and H. N. Alshareef, Angew. Chem., Int. Ed., 2018, 57, 3943–3948.

90. C. Xia, J. Guo, Y. Lei, H. Liang, C. Zhao, and H. N. Alshareef, Adv. Mater., 2018, 30, 1705580.

91. Michael McEldrew, Zachary A. H. Goodwin, Sheng Bi, Martin Z. Bazant, and Alexei A. Kornyshev, The Journal of Chemical Physics 152, 234506 (2020) https://doi.org/10.1063/5.0006197

92. Shen Qiu, Yunkai Xu, Xin Li, Sean K. Sandstrom, Xianyong Wu, Xiulei Ji, Electrochemistry Communications,Volume 122, 2021, 106880, ISSN 1388-2481, https://doi.org/10.1016/j.elecom.2020.106880.

93. X. Wang, B. Xi, Z. Feng, W. Chen, H. Li, Y. Jia, J. Feng, Y. Qian and S. Xiong, J. Mater. Chem. A, 2019, 7, 19130.

94. Kundu, D., Adams, B., Duffort, V. *et al.* . *Nat Energy* **1,** 16119 (2016). https://doi.org/10.1038/nenergy.2016.119

95. Z. Xie, J. Lai, X. Zhu and Y. Wang, ACS Appl. Energy Mater., 2018, 1, 6401–6408.

96. X. Wang, B. Xi, Z. Feng, W. Chen, H. Li, Y. Jia, J. Feng, Y. Qian and S. Xiong, J. Mater. Chem. A, 2019, 7, 19130.

97. Fangwang Ming, Hanfeng Liang, Yongjiu Lei, Sharath Kandambeth, Mohamed Eddaoudi, and Husam N. Alshareef *ACS Energy Letters* **2018** *3* (10), 2602-2609 DOI: 10.1021/acsenergylett.8b01423

98. ***J. Mater. Chem. A***, 2020,**8**, 15130-1513

99. Liu, Sucheng, He Zhu, Binghao Zhang, Gen Li, Hekang Zhu, Yang Ren, Hongbo Geng, Yang Yang, Qi Liu, and Cheng Chao Li. *Advanced Materials* 32, no. 26 (2020): 2001113.

100. Chen, Dong, Xianhong Rui, Qi Zhang, Hongbo Geng, Liyong Gan, Wei Zhang, Chengchao Li, Shaoming Huang, and Yan Yu *Nano Energy* 60 (2019): 171-178.

101. Clites, Mallory, and Ekaterina Pomerantseva. *Energy Storage Materials* 11 (2018): 30-37.

102. Lai, Jianwei, Hui Tang, Xiuping Zhu, and Ying Wang. Journal of Materials Chemistry A 7, no. 40 (2019): 23140-23148.

103. Tang, Boya, Jiang Zhou, Guozhao Fang, Fei Liu, Chuyu Zhu, Chao Wang, Anqiang Pan, and Shuquan Liang. *Journal of Materials Chemistry A* 7, no. 3 (2019): 940-945.

104. Yang, Yongqiang, Yan Tang, Guozhao Fang, Lutong Shan, Jiasheng Guo, Wenyu Zhang, Chao Wang, Liangbing Wang, Jiang Zhou, and Shuquan Liang. Energy & Environmental Science 11, no. 11 (2018): 3157-3162.

105. Zhang, Yao, Edison Huixiang Ang, Khang Ngoc Dinh, Kun Rui, Huijuan Lin, Jixin Zhu, and Qingyu Yan. Materials Chemistry Frontiers 5, no. 2 (2021): 744-762.

106. Fang, Guozhao, Jiang Zhou, Anqiang Pan, and Shuquan Liang. ACS Energy Letters 3, no. 10 (2018): 2480-2501.

107. Wan, Fang, and Zhiqiang Niu Angewandte Chemie 131, no. 46 (2019): 16508-16517.

108. Kuchena, Shelton Farai, and Ying Wang. *ACS Applied Energy Materials* 3, no. 12 (2020): 11690-11698.

109 .Somani, Prakash R., R. Marimuthu, and A. B. Mandale. *Polymer* 42, no. 7 (2001): 2991-3001.

110. Yanyan Liu, Zhenghui Pan, Dan Tian, Tao Hu, Hanmei Jiang, Jie Yang, Jingjing Sun, Jiqi Zheng, Changgong Meng, Yifu Zhang, Chemical Engineering Journal, Volume 399, 2020, 125842, ISSN 1385-8947, doi.org/10.1016/j.cej.2020.125842.

111. C. G. Wu, D. C. DeGroot, H. O. Marcy, J. L. Schindler, C. R. Kannewurf, Y.-J. Liu, W. Hirop, M. G. Kanatzidis, Chem. Mater. 1996, 8, 1992.

112. C.-G. Wu, D. C. DeGroot, H. O. Marcy, J. L. Schindler, C. R. Kannewurf, Y.-J. Liu, W. Hirpo, and M. G. Kanatzidis *Chemistry of Materials* **1996** *8* (8), 1992-2004 DOI: 10.1021/cm9600236

113. Rui Li, Fei Xing, Tianyu Li, Huamin Zhang, Jingwang Yan, Qiong Zheng, Xianfeng Li, , Energy Storage Materials, 38, 2021, 590-598.

114. Shi, Hua-Yu,Ye, Yin-Jian , Liu, Kuan un, Xiaoqi Angewandte Chemie International Edition, Angew. Chem. Int. Ed. 57 50, 1433-7851

115. P. Gomez-Romero , Hybrid Organic-Inorganic Materials —In Search of Synergic Ac- tivity, Adv. Mater. 13 (2001) 163 .

116. R. Pelster , G. Nimtz , B. Weßling , Mesoscale charge transport in polyaniline, J. Phys. II 4 (1994) 549 .

117. Surface Science Spectra24, 024001 (2017); doi: 10.1116/1.4998018

118. N. Zhang , M. Jia , Y. Dong , Y. Wang , J. Xu , Y. Liu , L. Jiao , F. Cheng, Adv. Funct. Mater. 29 (2019) 1807331 .

119. Farai Kuchena, Shelton, and Ying Wang. *Chemistry–A European Journal* 27, no. 62 (2021): 15450-15459.

120. Laviron, E. Journal of Electroanalytical Chemistry and Interfacial Electrochemistry 52, no. 3 (1974): 395-402.

121. Bard, Allen J., and Larry R. Faulkner. Student Solutions Manual to accompany Electrochemical Methods: Fundamentals and Applicaitons, 2e. John Wiley & Sons, 2002.

122. Dong, Shengyang, Woochul Shin, Heng Jiang, Xianyong Wu, Zhifei Li, John Holoubek, William F. Stickle et al. Chem 5, no. 6 (2019): 1537-1551.

123. Wang, Peng, Yifu Zhang, Hanmei Jiang, Xueying Dong, and Changgong Meng. *Chemical Engineering Journal* 427 (2022): 131548.

124. Li, Rui, Fei Xing, Tianyu Li, Huamin Zhang, Jingwang Yan, Qiong Zheng, and Xianfeng Li. *Energy Storage Materials* 38 (2021): 590-598.

125. Zhu, He, Yalan Huang, Hekang Zhu, Liguang Wang, Si Lan, Xinhui Xia, and Qi Liu. *Small Methods* 4, no. 6 (2020): 1900223.

126. W.-S. Huang, B. D. Humphrey, A. G. MacDiarmid, J. Chem. Soc. Faraday Trans. 1 1986, 82, 2385–2400; b) F. Genoud, M. Guglielmi, M. Nechtschein, E. Genies, M. Salmon, Phys. Rev. Lett. 1985, 55, 118–121; c) C. K. Chiang, C. R. Fincher, Y. W. Park, A. J. Heeger, H. Shirakawa, E. J. Louis, S. C. Gau, A. G. MacDiarmid, Phys. Rev. Lett. 1977, 39, 1098–1101.

127 Perera, Sanjaya D., Randall B. Archer, Craig A. Damin, Rubén Mendoza-Cruz, and Christopher P. Rhodes *Journal of Power Sources* 343 (2017): 580-591.

128 Cazzanelli, E., G. Mariotto, S. Passerini, and W. H. Smyrl. *Journal of non-crystalline solids* 208, no. 1-2 (1996): 8

129. Grey, C. P., and J. M. Tarascon. Nature materials 16, no. 1 (2017): 45-56.

130. Poizot, Philippe, Joël Gaubicher, Stéven Renault, Lionel Dubois, Yanliang Liang, and Yan Yao., *Chemical reviews* 120, no. 14 (2020): 6490-6557.

131. Deuchert, Klaus, and Siegfried Hünig, *Angewandte Chemie International Edition in English* 17, no. 12 (1978): 875-886.

132. Esser, Birgit, Franck Dolhem, Matthieu Becuwe, Philippe Poizot, Alexandru Vlad, and Daniel Brandell, *Journal of Power Sources* 482 (2021): 228814.

133. Kye, Hyojin, Yeongkwon Kang, Deogjin Jang, Ji Eon Kwon, and Bong-Gi Kim, *Advanced Energy and Sustainability Research* (2022): 2200030.

134. Zhao, Zhiming, Yongjiu Lei, Lin Shi, Zhengnan Tian, Mohamed Hedhili, Yusuf Khan, and Husam N. Alshareef. *Angewandte Chemie International Edition* (2022).

135. Han, Jiajun, Zhaowen Chen, and Jiawei Xu. *Materials Letters* 304 (2021): 130629.

136 Huang, Jianhang, Zhuo Wang, Mengyan Hou, Xiaoli Dong, Yao Liu, Yonggang Wang, and Yongyao Xia. *Nature communications* 9, no. 1 (2018): 1-8.

137. Li, Rui, Fei Xing, Tianyu Li, Huamin Zhang, Jingwang Yan, Qiong Zheng, and Xianfeng Li. *Energy Storage Materials* 38 (2021): 590-598.

138. Xu, Jun-Wei, Qing-Li Gao, Yong-Mei Xia, Xian-Sen Lin, Wei-Liang Liu, Man-Man Ren, Fan-Gong Kong, Shou-Juan Wang, and Chen Lin. *Journal of Colloid and Interface Science* 598 (2021): 419-429.

139. Kuchena, Shelton Farai, and Ying Wang. *ACS Applied Energy Materials* 3, no. 12 (2020): 11690-11698.

140. Kuchena, Shelton F., and Ying Wang. *Electrochimica Acta* 425 (2022): 140751.

141. Dong, Shengyang, Woochul Shin, Heng Jiang, Xianyong Wu, Zhifei Li, John Holoubek, William F. Stickle et al. *Chem* 5, no. 6 (2019): 1537-1551.

142. Kausaite-Minkstimiene, Asta, Viktor Mazeiko, Almira Ramanaviciene, and Arunas Ramanavicius Colloids and Surfaces A: Physicochemical and Engineering Aspects 483 (2015): 224-231.

143. Ansari, Reza. *E-Journal of Chemistry* 3, no. 4 (2006): 186-201.

144. Zhang, Bin, Yiting Xu, Yifang Zheng, Lizong Dai, Mingqiu Zhang, Jin Yang, Yujie Chen, Xudong Chen, and Juying Zhou. *Nanoscale research letters* 6, no. 1 (2011): 1-9.

145. Wang, Ying, and Shelton F. Kuchena. " *ACS omega* (2022).

146. MA, Chougule, Pawar SG, Godse PR, Sen Shashwati, and Patil VB. *Soft nanoscience letters* 2011 (2011).

147. Yamada, Yuki, Kenji Usui, Keitaro Sodeyama, Seongjae Ko, Yoshitaka Tateyama, and Atsuo Yamada. *Nature Energy* 1, no. 10 (2016): 1-9.

148. Coustan, Laura, Galyna Shul, and Daniel Belanger. *Electrochemistry Communications* 77 (2017): 89-92.

149. Amiri, Mona, and Daniel Bélanger. *ChemSusChem* 14, no. 12 (2021): 2487-2500.

150. Lee, Myeong Hwan, Sung Joo Kim, Donghee Chang, Jinsoo Kim, Sehwan Moon, Kyungbae Oh, Kyu-Young Park et al. Materials Today 29 (2019): 26-36.

151. Liu, Ting, Lujie Tang, Haowei Luo, Shuang Cheng, and Meilin Liu. *Chemical Communications* 55, no. 85 (2019): 12817-12820.

152. Dubouis, Nicolas, Pierre Lemaire, Boris Mirvaux, Elodie Salager, Michaël Deschamps, and Alexis Grimaud. Energy & Environmental Science 11, no. 12 (2018): 3491-3499.

153. Holoubek, John J., Heng Jiang, Daniel Leonard, Yitong Qi, Galo C. Bustamante, and Xiulei Ji. , *Chemical Communications* 54, no. 70 (2018): 9805-9808.

154. Tian, Zhengnan, Vinayak S. Kale, Yizhou Wang, Sharath Kandambeth, Justyna Czaban-Jozwiak, Osama Shekhah, Mohamed Eddaoudi, and Husam N. Alshareef, Journal of the American Chemical Society 143, no. 45 (2021): 19178-19186.

155. Zhang, Qing, Zhijie Wang, Shilin Zhang, Tengfei Zhou, Jianfeng Mao, and Zaiping Guo. *Electrochemical Energy Reviews* 1, no. 4 (2018): 625-658.

156. Sha, Mo, Long Liu, Huaping Zhao, and Yong Lei. "Review on recent advances of cathode materials for potassium-ion batteries." *Energy & Environmental Materials* 3, no. 1 (2020): 56-66.

157. Wu, Zhenrui, Jian Zou, Shulin Chen, Xiaobin Niu, Jian Liu, and Liping Wang, *Journal of Power Sources* 484 (2021): 229307.

158. Tian, Zhengnan, Vinayak S. Kale, Yizhou Wang, Sharath Kandambeth, Justyna Czaban-Jozwiak, Osama Shekhah, Mohamed Eddaoudi, and Husam N. Alshareef, *Journal of the American Chemical Society* 143, no. 45 (2021): 19178-19186.

159. Yan, Lei, Ya-E. Qi, Xiaoli Dong, Yonggang Wang, and Yongyao Xia. *eScience* 1, no. 2 (2021): 212-218.

160. Zhao, Zhiming, Yongjiu Lei, Lin Shi, Zhengnan Tian, Mohamed Hedhili, Yusuf Khan, and Husam N. Alshareef. *Angewandte Chemie International Edition* (2022).

161. Yan, Lei, Ya-E. Qi, Xiaoli Dong, Yonggang Wang, and Yongyao Xia. eScience 1, no. 2 (2021): 212-218.

Vita

Shelton Kuchena obtained his bachelor's degree in 2016 from the National University of Science Technology, Zimbabwe. He is currently a Ph.D. student in the Department of Mechanical and Industrial Engineering, Engineering Science program Concentration: Material Science and Engineering, at Louisiana State University under the supervision of Dr. Ying Wang. His research interests are in the development of advanced electrodes and electrolytes for ammonium ion batteries. Shelton Kuchena professional publications up to date in the PhD program at LSU are as follows:

1. **Kuchena, Shelton Farai**, and Ying Wang. "Superior polyaniline cathode material with enhanced capacity for ammonium ion storage." *ACS Applied Energy Materials* 3, no. 12 (2020): 11690-11698.

2. **Farai Kuchena, Shelton**, and Ying Wang. "A full flexible Ammonium ion battery based on the concentrated hydrogel electrolyte for enhanced performance." *Chemistry–A European Journal* 27, no. 62 (2021): 15450-15459.

3. **Kuchena, Shelton F**., and Ying Wang. "V_2O_5 intercalated with polyaniline for improved kinetics in aqueous ammonium-ion batteries." *Electrochimica Acta* 425 (2022): 140751.

4. Wang, Ying, and **Shelton F. Kuchena**. "Recent Progress in Aqueous Ammonium-Ion Batteries." *ACS omega* 7, no. 38 (2022): 33732-33748.

5. **Kuchena, Shelton Farai**, and Ying Wang. "A metal-free all-organic ammonium-ion battery with low-temperature applications." *Journal of Materials Chemistry A* 11, no. 6 (2023): 2814-2825.